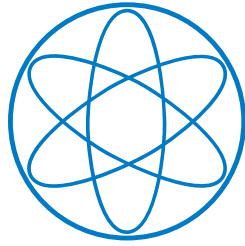Lehrstuhl E15
Physik - Department

Realization and Characterization of the Muon Veto Scintillator and the Buffer Liquid of the Double Chooz Experiment

Diplomarbeit

Judith Meyer

1. Dezember 2010

Technische Universität München

Abstract

Neutrino physics is one of the most exciting and important fields of modern particle and astroparticle physics. The enhanced understanding of neutrinos and their properties today provides the opportunity to use them as a new and unique probe into a huge variety of fields, for example, in astrophysics, geophysics, and cosmology. Many experimentally observed phenomena, such as the lack of solar electron neutrinos, are known to be caused by neutrino oscillations, which describe the periodical change in the probability to detect a particular flavor during the propagation of neutrinos in space. The underlying oscillation theory has six independent parameters. While four of them, namely the mixing angles ϑ_{12} and ϑ_{23} as well as the two mass‑squared differences Δm_{21}^2 and Δm_{32}^2 have been determined with high accuracy by several experiments, the small mixing angle ϑ_{13} and the CP‑violating phase δ are still unknown. In order to further expand this theory, the focus of many current neutrino experiments, such as the Double Chooz experiment, is on quantifying ϑ_{13}. The result will also have a significant impact on the determination of the phase δ.

The Double Chooz project is a reactor neutrino experiment located in the French Ardennes using the two cores of the Chooz reactor plant as efficient neutrino sources. For neutrino detection Double Chooz will use two large volume liquid scintillator based detectors in order to make a competitive measurement. Built identically, their purpose is to cancel or decrease significantly the systematic uncertainties. Both detectors feature a dedicated muon identification system, called *muon veto* or *inner veto*, which is an active detector based on a liquid scintillator in order to reject background events induced by cosmic muons. Another fluid of the detector is the non‑scintillating buffer liquid with the objective of shielding the target from natural radioactivity. The detection quality and therefore, the physical capability of the Double Chooz experiment strongly depends upon the optical characteristics of these liquids. This thesis focuses on testing both the muon veto scintillator and the buffer liquid on their optical properties, which play a crucial role in the decision regarding their composition and in their realization.

Different products were available for the selection of the components of both buffer and muon veto liquid. Selection criteria included the results of the attenuation length and light yield measurements. Having decided for the final compositions of the scintillator, it has been prepared on grand scale at *Wacker Chemie* in Munich. Finally, all liquids have been prepared on site in Chooz.

The attenuation length is a parameter quantifying the optical transparency of a liquid scintillator. A high attenuation length implies high transparency, which is of essential concern for a scintillator given the fact that light from each event in the liquid should be able to reach the photomultipliers located at the surfaces of the detector vessels. The attenuation length at $430\,\mathrm{nm}$ for the final muon veto

scintillator from Chooz was found to be more than 8 m and for the final buffer liquid more than 12 m. These results exceed the requirements for both the muon veto scintillator and the buffer liquid.

The light yield, as it characterizes the efficiency in the conversion of energy deposited in the scintillator into detectable photons, is another key parameter of a liquid scintillator. Light yield measurements using γ-radiation have been carried out within the framework of this thesis. Based on them, the concentration of PPO as a wavelength shifter for the muon veto scintillator has been chosen to be 2 g/l. With an absolute light yield of 9 photons/keV for the ready scintillator the expected light yield has been achieved.

In order to analyze the light yield of the muon veto scintillator with respect to neutrons, it was the aim to determine the proton-quenching factor, which is a variable relevant for a precise understanding of the Double Chooz detector response. By time-of-flight measurements performed at the Maier-Leibnitz-Laboratorium in Munich the proton-quenching factor at an energy of 10.6 MeV has been determined to be 2.6. A Monte Carlo simulation based on C++ was used to investigate its energy dependence.

Furthermore, the muon veto scintillator has been tested on its capability of distinguishing between incident neutrons and gammas via pulse-shape discrimination. The neutron-γ discrimination was found to be possible on a 1σ-level above an energy threshold of 2180 keV. As regards Double Chooz, this will allow a greater control of background.

4

Contents

1. Introduction to Neutrinos

Astroparticle physics is a young multidisciplinary field of research, in which particle physics, astronomy, astrophysics and cosmology converge. While particle physics deals with the study of the structure of matter and the fundamental laws that govern their interaction and astronomy as well as astrophysics study the evolution and structure of the Universe from the Hot Big Bang up to now, it is cosmology that yields the theory to link those fields of physics. During the last years astroparticle physics has taken remarkable strides towards understanding the evolution of our Universe. The field of *neutrinos* thereby plays an important role. In the Standard Model of particle physics neutrinos are the least massive fermions [1, 2]. They belong to the family of neutral leptons and exist in three types, also called *flavors*: electron neutrinos ν_e, muon neutrinos ν_μ and tau neutrinos ν_τ. Each type has a corresponding antiparticle, named antineutrino ($\overline{\nu}_e, \overline{\nu}_\mu, \overline{\nu}_\tau$).

Neutrinos are of great scientific interest. They are created as a result of certain types of radioactive decays, nuclear reactions such as those that take place in the Sun, in nuclear reactors, or through the interaction of cosmic rays with the atmosphere. As they are known to be particles that are not significantly attenuated by their travel through the interstellar medium, they can make an exceptional probe for environments that are typically concealed from other observation techniques. Therefore, they do not only provide a new method to study astrophysical processes like the energy production in the Sun or the mechanism of core-collapse supernova explosions, but due to the discovery of so-called *neutrino oscillations* and, connected to that, neutrino masses, even give a strong motivation to extend the Standard Model of particle physics and to search for new physics beyond it.

The neutrino was first postulated in 1930 by Wolfgang Pauli in order to preserve the conservation of energy, momentum and angular momentum in beta decays [3]. The fact that an electron created and emitted by beta decay showed a continuous energy spectrum and not a discrete one as expected for a two body decay, had presented former physics with a challenge. Pauli theorized that a third undetected particle was carrying away the observed difference between the energy, momentum, and angular momentum of the initial and final particles. He proposed that this particle had to be electrically neutral and only very weakly interacting, which also was an explanation for the missing experimentally measured data concerning this particle up to that time. To the detection of the neutrino, however, almost 20 more years should elapse. It was not before the discovery of nuclear fission and the construction of the first nuclear power plants that neutrino sources with a very high efficiency were available, which enabled Cowan and Reines to succeed in the

detection of the neutrino in 1956 [4].

The possibility of neutrinos changing their flavor was considered the first time at the discovery of the solar neutrino number discrepancy [3]. The Sun generates its energy by nuclear fusion of hydrogen nuclei into helium. 98.4% of the helium produced in the Sun comes from a series of steps called the *p* - *p* (*proton* - *proton*) chain with the following netto reaction: $4H + 2e^- \rightarrow {}^4He + 2\nu_e + 26.73\,\text{MeV}$. The remaining 1.6% of the helium is generated in the so-called *CNO cycle*, in which small amounts of carbon, nitrogen and oxygen isotopes are used as a catalyst to produce one alpha particle, two positrons and two electron neutrinos. Those neutrinos just like the ones produced in the $\text{p} - \text{p}$ chain, escape carrying away about 3% of the released energy. Despite the huge circumfluent covering mass of the Sun, the neutrinos reach the Earth as they do not significantly interact with matter. Depending on their reaction of production in the $\text{p} - \text{p}$ chain, which determines the neutrino energy, one can classify solar neutrinos. Headed by the astrophysicist Raymond Davis, the first experiment for the investigation of the solar neutrino flux started operating in 1968 [5]. The *Homestake* experiment or often referred to as the *Davis* experiment used the inverse beta decay of chlorine as a proof of evidence and was the first experiment to successfully detect and count solar neutrinos. Surprisingly, the measured neutrino rate turned out to be only one third of the neutrino rate predicted by the Standard Solar Model. This great discrepancy between the neutrino rates became generally known as the *Solar Neutrino Problem* and could be confirmed by further experiments such as *GALLEX* [6] and *SuperKamiokande* [7]. The *SNO* experiment [8] succeeded in unraveling this mystery. In contrast to its predecessors, SNO used a Cherenkov detector containing heavy water, which made it possible to distinguish between electron neutrinos and neutrinos of different flavors. This way the missing electron neutrinos could be identified as muon - or tau neutrinos, which was the first experimental confirmation of neutrino oscillations.

At the present day only the third mixing angle, namely ϑ_{13}, is still missing for a complete theoretical description of neutrino oscillations between the three neutrino flavors. The *Double Chooz* project [9] is a neutrino experiment with the objective of the search for this final unknown parameter. Double Chooz (DC), like its predecessor *Chooz* [10], is a reactor neutrino experiment using the two cores of the Chooz reactor plant as efficient neutrino sources. The Chooz experiment has already been able to determine the best upper limit known today for the angle ϑ_{13} ($\sin^2(2\vartheta_{13}) < 0.16$ at a 90% C. L. [11]) and, therefore, also for the maximum conversion probability of the antielectron neutrino. Now, it is the aim of Double Chooz to finally determine ϑ_{13} or at least to improve this limit.

2. Neutrino Oscillations

By definition neutrino oscillations are oscillating transitions of a neutrino of a certain flavor into a neutrino of another flavor during its propagation through space [3]. This means that the probability to measure a certain flavor of a neutrino changes periodically with its preceding movement. The fact that neutrino oscillations exist implicates important consequences. Contrary to what had been previously assumed, a precedent condition for neutrino oscillations is that not all neutrinos can be massless. Moreover, neutrino oscillations violate the lepton flavor number conservation, merely the lepton number is preserved. Both scenarios are not contained in the Standard Model of particle physics. As they do not violate the Standard Model neither, the theory of neutrino oscillations could establish as an enhancement of the Standard Model.

2.1. Derivation of the Oscillation Formula

Solar and atmospheric neutrino experiments have indicated that the reason for neutrino oscillations is a discrepancy between the flavor and the mass eigenstates of the neutrinos [3]. The three flavor eigenstates $|\nu_e\rangle, |\nu_\mu\rangle, |\nu_\tau\rangle$ of the neutrinos are the eigenstates of the weak interaction, in which neutrinos are generated. They are also the ones one can detect. The mass eigenstates $|\nu_1\rangle, |\nu_2\rangle, |\nu_3\rangle$ in contrast, which are not identical to the eigenstates of the weak interaction, are responsible for the propagation of the neutrinos. Each group of eigenstates forms an independent orthonormal basis of the Hilbert space, so both basis systems can be transformed into each other. The corresponding matrix is a 3×3 mixing matrix, also referred to as PMNS-matrix [1] [3, 12, 13]:

$$
\begin{pmatrix} \nu_e \\ \nu_\mu \\ \nu_\tau \end{pmatrix} = \begin{pmatrix} U_{e1} & U_{e2} & U_{e3} \\ U_{\mu 1} & U_{\mu 2} & U_{\mu 3} \\ U_{\tau 1} & U_{\tau 2} & U_{\tau 3} \end{pmatrix} \begin{pmatrix} \nu_1 \\ \nu_2 \\ \nu_3 \end{pmatrix}
\tag{2.1}
$$

By means of the PMNS-matrix the oscillation probability of a neutrino of a certain flavor can be derived. First of all, a flavor eigenstate can be expressed in terms of mass eigenstates as follows:

---

[1] *The matrix is named after the physicists Bruno Pontecorvo, Ziro Maki, Masami Nakagawa and Shoichi Sakata.*

$$|\nu_\alpha\rangle = \sum_{i=1}^{3} U_{\alpha i}|\nu_i\rangle \tag{2.2}$$

Here, the flavor eigenstates are denoted by $|\nu_\alpha\rangle$ with $\alpha = e, \mu, \tau$, and the mass eigenstates are denoted by $|\nu_i\rangle$ with $i = 1, 2, 3$. $U_{\alpha i}$ describes the elements of the mixing matrix. With respect to the evolution in time of the mass eigenstates, that one obtains by solving the Dirac equation, the flavor eigenstates are [2]:

$$|\nu_\alpha(t)\rangle = \sum_{i=1}^{3} U_{\alpha i} e^{-iE_i t}|\nu_i\,(t=0)\rangle \tag{2.3}$$

To get the transition probability $P_{\nu_\alpha \to \nu_\beta}$ of a neutrino of the flavor α to the flavor β, the transition amplitude $|\langle \nu_\beta | \nu_\alpha(t)\rangle|$ has to be determined and its absolute value has to be squared:

$$P_{\nu_\alpha \to \nu_\beta}(t) = |\langle \nu_\beta | \nu_\alpha(t)\rangle|^2 = \left| \sum_{k=1}^{3} U_{\alpha k}^\star e^{-iE_k t} U_{\beta k} \right|^2$$

$$= \sum_{k,j=1}^{3} U_{\alpha k}^\star U_{\beta k} U_{\alpha j} U_{\beta j}^\star e^{-i(E_k - E_j)t} \tag{2.4}$$

where $U_{\alpha k}^\star$ and $U_{\beta j}^\star$ are the complex conjugated matrix elements. The transition probability from the flavor state $|\nu_\alpha\rangle$ to the flavor state $|\nu_\beta\rangle$ hence varies periodically with time as a function of the energy difference $E_k - E_j$ of the two states. Under the assumptions made in the Standard Model of neutrino oscillations, namely that massive neutrinos have the same momentum $\vec{p}$ and that neutrinos detectable by oscillation experiments are ultrarelativistic, i.e. they almost travel with the speed of light, the exponent of the transition probability can be simplified. The approximation

$$E_k = \sqrt{\vec{p}^2 + m_k^2} \simeq E + \frac{m_k^2}{2E} \tag{2.5}$$

yields

$$E_k - E_j = \frac{\Delta m_{kj}^2}{2E}. \tag{2.6}$$

Here $E \equiv |\vec{p}|$ is the energy of the approximately massless neutrino and $\Delta m_{kj}^2 = m_k^2 - m_j^2$ are the mass squared differences. Next $c \simeq 1$ results in $t \simeq L$. L is the distance between neutrino source and detector that has been passed by the ultrarelativistic neutrino. In contrast to the time t of the propagation, it is a measurable parameter. This leads to the standard formula of the oscillation probability in vacuum. It gives the probability P, that a ν_α is measured as a ν_β after a distance L of flight and clarifies the dependence of the oscillation probability on the neutrino masses [14]:

$$
\begin{aligned}
P_{\nu_\alpha \to \nu_\beta}(L) &= \sum_{k,j=1}^{3} U_{\alpha k}^\star U_{\beta k} U_{\alpha j} U_{\beta j}^\star e^{-i\frac{\Delta m_{kj}^2}{2E}L} \\
&= \delta_{\alpha\beta} - 4\sum_{j>k} \Re\left(U_{\alpha k}^\star U_{\beta k} U_{\alpha j} U_{\beta j}^\star\right) \sin^2\left(\frac{\Delta m_{kj}^2}{4E}L\right) \\
&+ 2\sum_{j>k} \Im\left(U_{\alpha k}^\star U_{\beta k} U_{\alpha j} U_{\beta j}^\star\right) \sin\left(\frac{\Delta m_{kj}^2}{4E}L\right) \qquad (2.7)
\end{aligned}
$$

In obtaining (2.7) the unitarity of U has been used. $\delta_{\alpha\beta}$ is the Kronecker‑symbol:

$$
\delta_{\alpha\beta} = \begin{cases} 1 & \text{if } \alpha = \beta, \\ 0 & \text{if } \alpha \neq \beta, \end{cases}
$$

The phase differences $\propto \Delta m_{ij}^2 \cdot \frac{L}{2E}$ in the complex exponential function result in sine‑ and cosine‑like oscillating terms of the probability. If not all Δm_{kj}^2 disappear, which corresponds to the case of at least one massive neutrino, oscillations between the different flavor eigenstates of the neutrinos exist. As a consequence of this mechanism, it follows immediately that neutrino oscillations are only sensitive on the mass squared differences, but not on the absolute neutrino mass scale. The mass squared differences hence determine the frequency of the oscillations, while the oscillation amplitudes are given by the mixing angles ϑ_{ij} (see 2.2). Thus the mixing angles ϑ_{ij} that are contained in the matrix elements of the mixing matrix, can, up to a certain extend, be seen as a quantity for the intensity of the mixing. Strictly speaking, the considerations above are only valid for vacuum oscillations. When neutrinos are propagating through matter, neutrino oscillations have to be modified. This is known as the Mikheyev‑Smirnov‑Wolfenstein (MSW) effect [1, 3]. The presence of electrons in matter changes the energy levels of the propagation eigenstates due to additional charged current forward scattering of the electron neutrinos. As a consequence neutrinos in matter do have a different effective mass from neutrinos in vacuum, which in turn has an effect on the neutrino oscillations that are dependent on the mass square differences. This effect, however, is only

noticeable for very high densities of matter, as for example in stars, and very long distances of flight as it is the case for crossing the Earth. None of them plays any role for the Double Chooz experiment, which uses reactor neutrinos. The distances they travel are rather short ($\sim 1\,$km) and no high densities of matter do appear [9], which is why matter effects can be neglected.

2.2. Oscillation Parameters and their Determination

The mixing matrix of equation (2.1) can be written as a product of four 3×3 matrices [3]:

$$
\begin{aligned}
U &= \begin{pmatrix} U_{e1} & U_{e2} & U_{e3} \\ U_{\mu 1} & U_{\mu 2} & U_{\mu 3} \\ U_{\tau 1} & U_{\tau 2} & U_{\tau 3} \end{pmatrix} \\
&= \begin{pmatrix} 1 & 0 & 0 \\ 0 & \cos\vartheta_{23} & \sin\vartheta_{23} \\ 0 & -\sin\vartheta_{23} & \cos\vartheta_{23} \end{pmatrix} \cdot \begin{pmatrix} \cos\vartheta_{13} & 0 & \sin\vartheta_{13}e^{-i\delta} \\ 0 & 1 & 0 \\ -\sin\vartheta_{13}e^{-i\delta} & 0 & \cos\vartheta_{13} \end{pmatrix} \\
&\cdot \begin{pmatrix} \cos\vartheta_{12} & \sin\vartheta_{12} & 0 \\ -\sin\vartheta_{12} & \cos\vartheta_{12} & 0 \\ 0 & 0 & 1 \end{pmatrix} \cdot \begin{pmatrix} 1 & 0 & 0 \\ 0 & e^{i\alpha} & 0 \\ 0 & 0 & e^{i\beta} \end{pmatrix}
\end{aligned}
\tag{2.8}
$$

ϑ_{ij} stands for the mixing angles, which will later on often be referred to in the form of $\sin^2\vartheta_{ij}$. δ is the CP violating phase, which does not vanish if neutrino oscillations violate CP-symmetry [2]. The violation of CP symmetry is being expected, however, up to now it has not been possible to experimentally show it [15]. α and β in the last matrix only differ from zero, if neutrinos are Majorana particles, which up to now has neither been shown nor been disproved. The question whether neutrinos are Majorana particles or not, that is to say whether neutrinos are their own antiparticles or not, does not have any effect on neutrino oscillations [3, 16]. Inserting the matrix U (eq. (2.8)) in the standard formula of the oscillation probability (eq. (2.7)) reveals the oscillation probabilities for the three neutrino generations [3]. The neutrino oscillation probabilities depend on six independent parameters, two mass squared difference, the three mixing angles and the CP violating phase δ. In fact, the probabilities to detect a certain flavor depend on the fraction of the distance L passed between source and detector and the energy E of the neutrinos (see eq. (2.7)). Thus this ratio is the crucial experimental variable for a neutrino-oscillation experiment. Any experiment that allows the measurement and variation of L/E, in general, is sensitive on neutrino oscillations and makes it possible to

---

[2]*In particle physics, CP symmetry states that the laws of physics are the same, if a particle was interchanged with its antiparticle (charge conjugation or C symmetry), and all spatial coordinates were swapped (parity or P symmetry).*

access and determine the several parameters of the oscillation formula almost independently from each other. For all oscillation experiments, the types of neutrinos at the source have to be known and types of neutrinos in the detector have to be determined (e.g. by a CC-reaction on the nucleon). Basically, there are two possible types of oscillation experiments.

- So-called *appearance experiments* measure the probability $P_{\nu_\alpha \to \nu_\beta}$ that a neutrino type, different from the one generated in the source, is being detected. Therefore, it is of great importance for such experiments to exactly know about possible ν_β-impurities in the ν_α-beam.

- In *disappearance experiments* the type of neutrino produced in the source is being detected later on. This means, the survival probability $P_{\nu_\alpha \to \nu_\alpha}$ that an initial ν_α reaches the detector respectively the probability $P_{\nu_\alpha \to \nu_x} = 1 - P_{\nu_\alpha \to \nu_\alpha}$ that the initial ν_α has disappeared, is being measured. For such experiments it is important to either know the initial neutrino flux at the source or the neutrino flux at two different distances from the source in order to compare the related spectra.

Neutrinos can be produced in several processes revealing a broad range of neutrino energies. The most important neutrino sources used for the search of oscillations, the according energies as well as the relevant parameters L and $min\,(\Delta m^2)$ characterizing qualitatively the limit on the sensitivity of the different experiments are summarized in table (2.1). These values correspond to the reactor experiments *CHOOZ* [10] ($L \sim 1\,\mathrm{km}$) and *KamLAND* [17] ($L \sim 100\,\mathrm{km}$), to past ($L \sim 1\,\mathrm{km}$) and future ($L \sim 300 - 1000\,\mathrm{km}$) accelerator experiments (*K2K [18], MINOS [19], OPERA [20], T2K [21], NOνA [22]*), the atmospheric neutrino experiment *Super-Kamiokande* [7] and solar experiments such as *Borexino* [23] or *SNO* [8].

neutrino source	type of neutrino	E [MeV]	L [km]	$min\,(\Delta m^2)$ [eV^2]
reactor	$\overline{\nu}_e$	$1 - 10$	1	$\sim 10^{-3}$
reactor	$\overline{\nu}_e$	$1 - 10$	100	$\sim 10^{-5}$
accelerator	$\nu_\mu, \overline{\nu}_\mu,$	$10^3 - 10^5$	1	~ 1
accelerator	$\nu_\mu, \overline{\nu}_\mu$	$10^3 - 10^5$	1000	$\sim 10^{-3}$
atmosphere	$\nu_{\mu,e}, \overline{\nu}_{\mu,e}$	$10^2 - 10^4$	10^4	$\sim 10^{-4}$
sun	ν_e	$10^{-1} - 10$	$1.5 \cdot 10^8$	$\sim 10^{11}$

Table 2.1.: *The table lists neutrino sources with the corresponding neutrino type, energy, baseline L and sensitivity.* [3, 11].

Due to the successful oscillation experiments of the last decades, the PMNS-matrix could almost be completely determined. The combination of the results of all relevant neutrino experiments yields the oscillation parameters we know today. Ta-

ble (2.2) gives an overview of the current data as well as the current best constraint on ϑ_{13}. For $\sin^2(2\vartheta_{13})$ the low value of Δm_{32}^2 has been used.

Parameter	Value	Experiment
Δm_{21}^2 $[10^{-5}\ \mathrm{eV}^2]$	$7.59^{+0.19}_{-0.21}$ (90% C.L.)	KamLAND + global solar
Δm_{32}^2 $[10^{-3}\ \mathrm{eV}^2]$	2.43 ± 0.13 (68% C.L.)	MINOS
$\sin^2(2\vartheta_{12})$	0.87 ± 0.03 (90% C.L.)	KamLAND + global solar
$\sin^2(2\vartheta_{23})$	> 0.92 (90% C.L.)	SuperKamiokande
$\sin^2(2\vartheta_{13})$	< 0.16 (90% C.L.)	CHOOZ

Table 2.2.: *The current values of the neutrino oscillation parameters and the corresponding experiments are listed.* [11].

2.3. Measurement of ϑ_{13}

While two of the three mixing angles have already been sufficiently measured [7, 17], this is not the case for ϑ_{13}. This remaining mixing angle, however, is of great relevance for neutrino physics. A nonzero value of ϑ_{13} is crucial in order to access a possible CP-violating phase δ, to probe the neutrino mass hierarchy via neutrino interactions in the Earth or Supernovae and to discriminate different theoretical models for the neutrino mass mixing matrix [24]. For a vanishing angle on the other hand, the question would arise whether this is related to a new, up to now unknown symmetry [25]. The measurement of ϑ_{13}, though, is quite challenging as it is known to be very small compared to the other two neutrino mixing angles. Two ways of determining this last missing angle have emerged.

2.3.1. Accelerator based Superbeam Experiments

The superbeam is a natural extension of the conventional neutrino beam and current and approved experiments are mostly of this type. In superbeam experiments a very intensive neutrino or antineutrino beam from a particle accelerator is used to realize the appearance of electron (anti)neutrinos [22, 26, 27]. Therefore, a detector is located at a distance in the order of $\sim 100\,\mathrm{km}$. For generating the neutrino beam, accelerated protons are smashed onto a fixed target producing charged pions or kaons. Having been magnetically focused into a long tunnel, these unstable particles decay during flight. Because of the relativistic boost of the decaying particles, high-energetic muon (anti)neutrinos are produced as a beam rather than isotropically. The high energies also imply a longer baseline for the first oscillation maximum (compare with sec. (2.3.2)), which leads to a sensitivity to matter effects. Considering those matter effects in eq. (2.7), the corresponding appearance probability becomes [28]:

$$P\left(\nu_{\mu} \to \nu_{e}\right) \approx \sin^{2}\left(2\vartheta_{13}\right) \cdot \sin^{2}\left(2\vartheta_{23}\right) \cdot \sin^{2}\left(\beta\right)$$
$$\pm \alpha \cdot \sin\left(2\vartheta_{13}\right) \cdot \sin\left(\delta\right) \cdot \sin\left(2\vartheta_{12}\right) \cdot \sin\left(2\vartheta_{23}\right) \cdot \beta \cdot \sin^{2}\left(\beta\right)$$
$$-\alpha \cdot \sin\left(2\vartheta_{13}\right) \cdot \cos\left(\delta\right) \cdot \sin\left(2\vartheta_{12}\right) \cdot \sin\left(2\vartheta_{23}\right) \cdot \beta \cdot \cos\left(\beta\right) \cdot \sin\left(\beta\right) \tag{2.9}$$
$$+\alpha^{2} \cdot \cos^{2}\left(\vartheta_{23}\right) \cdot \sin^{2}\left(2\vartheta_{12}\right) \cdot \beta^{2}$$

with the abbreviations $\alpha = \Delta m_{21}^{2}/\Delta m_{32}^{2}$ and $\beta = \Delta m_{32}^{2}L/4E$, where L is the distance between generation and detection. Furthermore, $\cos(\vartheta_{13}) \approx 1$ and $\sin(\alpha \cdot \beta) \approx \alpha \cdot \beta$ have been used. The plus sign in the formula relates to antineutrinos, whereas the minus sign relates to neutrinos.

The formula implies that superbeam experiments offer the opportunity to measure Δm_{23}^{2}, the CP-violating phase δ, ϑ_{23}, the mass hierarchy indicated by the sign of Δm_{23}^{2}, but also ϑ_{13}. On the other hand, eq. (2.9) also implicates that at a certain level of precision all oscillation formulas depend on all oscillation parameters leading to a complicated parameter dependence with degeneracies and correlations. This is a great disadvantage of superbeam experiments [28].

2.3.2. Reactor Neutrino Experiments

In the core of a reactor, radioactive elements decay and emit electron antineutrinos, typically about 10^{22} per core and second. Due to their very intensive flux and low energies (typically below 8 MeV), these antineutrinos provide a possibility to measure ϑ_{13} [29]. The small energies as well as short baselines guarantee the absence of matter oscillation effects. However, the low energies of antineutrinos from nuclear power plants also have the disadvantage that only disappearance experiments are possible. The reason for this is that the energy of reactor neutrinos is not sufficient for the production of muon or tau leptons. With the help of eq. (2.7), the survival probability of an antielectron neutrino can be calculated to [30]:

$$P\left(\overline{\nu}_{e} \to \overline{\nu}_{e}\right) = 1 - 2\sin^{2}\left(\vartheta_{13}\right)\cos^{2}\left(\vartheta_{13}\right)\sin^{2}\left(\frac{\Delta m_{31}^{2}L}{4E}\right)$$
$$- \cos^{4}\left(\vartheta_{13}\right)\sin^{2}\left(\frac{\Delta m_{21}^{2}L}{4E}\right) \tag{2.10}$$
$$+ 2\sin^{2}\left(\vartheta_{13}\right)\cos^{2}\left(\vartheta_{13}\right)\sin^{2}\left(\vartheta_{12}\right)$$
$$\cdot \left(\cos\left(\frac{\left(\Delta m_{31}^{2} - \Delta m_{21}^{2}\right)L}{2E}\right) - \cos\left(\frac{\Delta m_{31}^{2}L}{2E}\right)\right).$$

The second term describes the contribution of the atmospheric and the third term of the solar driven oscillations. The last term is the result of an interference between both. Assuming low energies and short baselines L ($\sim 1\,\text{km}$), as it is the case for reactor experiments, eq. (2.10) in a first approximation simplifies to:

$$P\left(\overline{\nu}_e \to \overline{\nu}_e\right) = 1 - 2\sin^2\left(\vartheta_{13}\right)\cos^2\left(\vartheta_{13}\right)\sin^2\left(\frac{\Delta m_{31}^2 L}{4E}\right) \qquad (2.11)$$

Therefore, the survival probability approximately is free from parameter correlations and degeneracies, which allows a *clean* measurement of ϑ_{13}. This is the great advantage of reactor neutrino experiments. At the same time, however, reactor neutrino experiments have up to now been dominated by higher systematic uncertainties originating, for example, from the missing knowledge of the precise antineutrino spectrum from the fission products of the reactor. Furthermore, the total neutrino flux had to be calculated from the thermal power of the reactor cores.

Since both superbeam and reactor neutrino experiments have advantages and disadvantages, it has been pointed out that the combination of data from superbeam and reactor neutrinos provides a possibility to resolve ambiguities and thus gives a much better sensitivity to oscillation parameters [82].

Moreover, the reactor neutrino experiment Double Chooz pursues a new strategy [9] to reduce the systematic uncertainties former reactor experiments suffered from. The concept is to make a competitive measurement with two identical detectors instead of using only one. A detector close to the reactor will be used for monitoring the total antineutrino flux, its spectral shape and time variations. A second detector will be located at a distance where the distortion of the antineutrino energy spectrum due to neutrino oscillations will allow to determine ϑ_{13} with an increased sensitivity.

3. The Double Chooz Experiment

The Double Chooz (DC) project is a neutrino experiment with the objective of the search for the third mixing angle, namely ϑ_{13}. Double Chooz, like its predecessor called Chooz [10], is a reactor neutrino disappearance experiment sited in the village Chooz, using the cores of the local reactor plant as efficient antineutrino sources. The Chooz experiment has already been able to determine the best upper limit known today for the parameter ϑ_{13}. Now, Double Chooz intends to finally determine ϑ_{13} or at least to improve its limit [9].

3.1. Double Chooz Concept

Figure 3.1.: Top view of the Chooz nuclear reactor plant sited at the river Meuse. The positions of the reactors as well as the close and the far detector of the DC project are indicated [31].

The Double Chooz experiment is located at the village Chooz in the French Ardennes near the border to Belgium (see fig. (3.1)). Chooz has one of the worldwide most powerful nuclear reactor plants (thermal power of 8.5 GW), which serves as an intense antineutrino source [9].

For the detection of the neutrinos, Double Chooz uses two underground detectors: The so-called *near detector* is meant to measure precisely the total antineutrino flux from the nuclear power plant, its spectral shape and time variations. Therefore, it is built under a small hill in a distance of only 400 m to the two reactor cores [9]. At this position, oscillation effects can be neglected (see fig. (3.2) and eq. (2.10)).
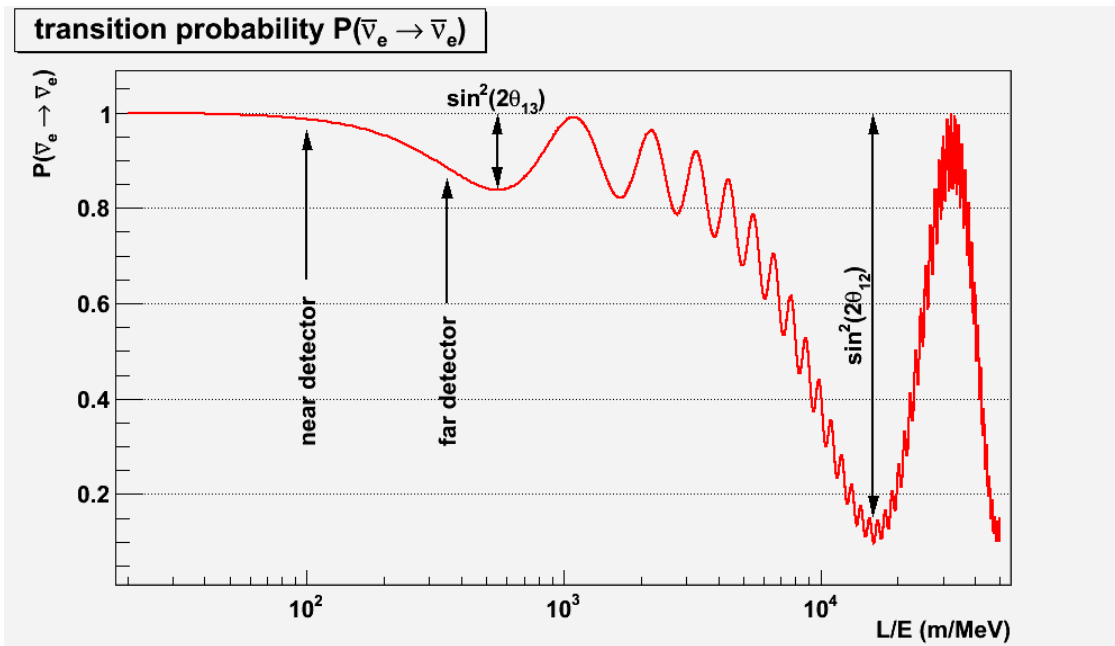
Figure 3.2.: *The survival probability of an electron antineutrino as a function of baseline L over neutrino energy E is plotted on a logarithmic scale [33]. For this plot the current data of [11] have been used. While the amplitude of the first oscillation minimum is given by $\sin^2(2\vartheta_{13})$, the amplitude of the second minimum is given by $\sin^2(2\vartheta_{12})$. Furthermore, the positions of the two DC detectors have been marked. While oscillation effects can be neglected at the location of the near detector, the effects from neutrino oscillations due to ϑ_{13} are nearly maximal at the position of the far detector.*

The *far detector* is located in a distance of about 1.05 km to the two reactors [9], which is near the location of the expected local minimum of the survival probability $P(\overline{\nu}_{e^-} \rightarrow \overline{\nu}_{e^-})$ (see fig. (3.2)). For a not too small mixing angle ϑ_{13}, the far detector will reveal the effects from the disappearance of the electron antineutrinos.

Comparing the total flux and the shape of the neutrino spectrum in both detectors, the mixing angle can be calculated.

By the use of two detectors and related to that the reduction of systematic uncertainties, a sensitivity, almost twice as high as by the use of only one detector, can be achieved. Currently, the installation of the first Double Chooz detector is close to completion. Double Chooz intends to start operating with the far detector only. The desired sensitivity after 1.5 years of data taking is $\sin^2(2\vartheta_{13}) \leq 0.06$. In the second phase both the near and the far detector will run simultaneously and the intended sensitivity after additional 3 years of data taking is $\sin^2(2\vartheta_{13}) \leq 0.06$ (for $\Delta m_{31}^2 \approx 2.5 \cdot 10^{-3} \text{eV}^2$ and a 90 % C.L.) [9]. Even if no effect was seen within the precision of the measurement, the known upper limit of ϑ_{13} could still be improved significantly. In both cases, the result will have great influence on the method of the determination of the CP violating phase δ, as the potential of future accelerator neutrino experiments particularly depends on the exact value of ϑ_{13} [32].

3.2. Detection Method

3.2.1. Signal

The Double Chooz experiment uses two underground liquid scintillator[1] based detectors. The electron antineutrinos undergo inverse beta decay in the scintillator liquid at an energy threshold of 1.8 MeV [9]:

$$\overline{\nu}_e + p \rightarrow e^+ + n \tag{3.1}$$

The positron as well as the neutron produce a flash of scintillation light, which can be used for a delayed coincidence measurement. Loosing its kinetic energy, the positron leads to a prompt signal and finally annihilates with an electron of the surroundings producing two 511 keV photons. The neutron thermalizes and, as the DC liquid scintillator is loaded with 1 g/l gadolinium (Gd), can afterwards be captured by a gadolinium nucleus releasing gamma quants with a total energy of about 8 MeV.

$$Gd + n \rightarrow Gd^\star \rightarrow Gd + \sum \gamma \, (8\,MeV) \tag{3.2}$$

On average, the time interval between the prompt annihilation and the neutron capture on gadolinium is 30 μs [34]. This delayed coincidence gives secure proof for one of the very seldom neutrino capture events and provides the opportunity to greatly reduce the number of background events. Without oscillations, the

---

[1]For the working principle of organic scintillators and further information see chapter (4).

expected neutrino rates are ~ 69 per day in the far and ~ 480 per day in the near detector.

Measuring the total energy of the positron yields the energy of the incoming electron antineutrino:

$$E_{\overline{\nu}_e} \simeq E_{e^+,vis} - 511\,keV + (m_n - m_p) \tag{3.3}$$

where $E_{e^+,vis}$ is the total visible energy of the positron containing the kinetic energy as well as the energy of the gamma rays from the annihilation process. m_n is the mass of the neutron and m_p the mass of the proton. The kinetic energy of the neutron has been neglected, which is a valid approximation for small neutrino energies.

3.2.2. Background

The reachable sensitivity in measuring ϑ_{13} is limited by systematical and statistical uncertainties. While statistical uncertainties can be reduced by increasing the detector mass and the measuring time, controlling the systematic uncertainties is more challenging. Many uncertainties former reactor-neutrino experiments suffered from, such as the uncertainty in the reactor antineutrino flux in the Chooz experiment [10], can significantly be reduced by the use of two detectors. The contribution of so-called *accidental* and *correlated* background events, however, remains.

Accidental background is caused by beta and gamma rays from natural radioactivity of the detector components that induce a prompt signal just as the positron from the inverse beta decay. Followed by an event creating an 8 MeV signal, such as slow neutrons produced by muons, this creates a delayed coincidence mimicking the antineutrino signal. Accidental background, however, can be measured, which allows to efficiently control its contribution to the systematical uncertainty [9].

Correlated background can be induced by cosmic muons in different ways. They are, for example, capable of producing fast neutrons via spallation in the surrounding rock, which then can cross the veto and buffer and deposit several MeV by thermalization in the γ-catcher or target scintillator before being captured on gadolinium causing a delayed coincidence.

Negatively charged muons can also be directly captured in the detector, followed by neutron emission. Finally, there is the possibility of muon spallation on ^{12}C, which can produce ^{8}He, ^{9}Li and ^{11}Li. Those isotopes decay on a timescale of 100 ms for ^{8}He and ^{9}Li and of a few ms for ^{11}Li and by doing so produce neutron cascades.

The systematics of the background due to fast neutrons cannot be measured efficiently. For its reduction, however, the determination of correlated events of fast neutrons in different active volumes of the detector, such as a threefold coincidence

of an energy deposition in the inner veto, the gamma catcher and the target, can be used [9].

3.3. Detector Design

Both detectors are built identically and consist of four concentric cylindrical volumes. Fig. (3.3) shows the scheme of a Double Chooz detector [9]:
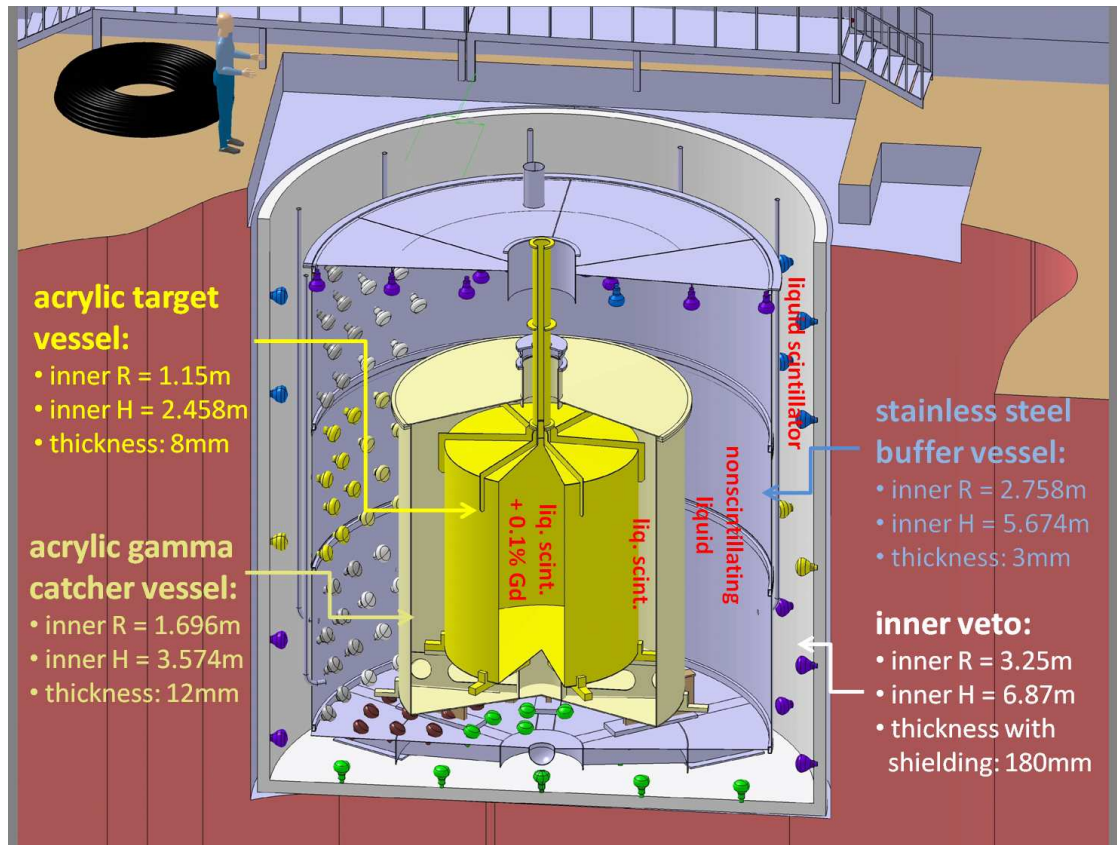

Figure 3.3.: Sketch of a Double Chooz detector [33]: Both the near and the far detector will be built identically. They will consist of four concentric cylindrical volumes. The neutrino target, the γ-catcher and the muon veto scintillator will be filled with liquid scintillators, whereas the buffer with the purpose of shielding the target volume from natural radioactivity will contain a non-scintillating liquid. The outer veto, consisting of plastic scintillator modules, will be installed on top of the detector and is not displayed in this figure. More detailed information is given in the text.

- Starting from the inside, there is the *neutrino target*, $10.3\,\mathrm{m}^3$ of an organic liquid scintillator loaded with $1\,\mathrm{g/l}$ gadolinium contained in a tank made of acrylic plastic material. The acrylic material was chosen to ensure chemical compatibility with the scintillating liquids, especially the gadolinium and to meet the condition of transparency to photons with wavelengths above $400\,\mathrm{nm}$ emitted by the scintillator.

- The vessel surrounding the target is also cylindrical shaped and made of acrylic plastic material. It it is filled with the so-called γ-*catcher*, more precisely, $22.6\,\mathrm{m}^3$ of a non-loaded scintillator. Its purpose is to efficiently measure the gamma rays released after the neutron capture on gadolinium as well as those produced by positron annihilation. Ensuring that also the gamma rays created at the edge of the neutrino target deposit their whole energy, the γ-catcher guarantees a homogeneous detector response.

- The next vessel is made of stainless steel and carries the 390 inner detector photomultiplier tubes[2]. It contains $114.2\,\mathrm{m}^3$ of the so-called *buffer* liquid[3]. This non-scintillating liquid has the purpose of shielding the target volume from natural radioactivity, mainly gamma rays emitted by the glass of the PMTs.

- The *inner veto* tank is filled with $90\,\mathrm{m}^3$ of a liquid scintillator, which acts as muon veto (MU) to distinguish between true neutrino signals and those that are signals caused by background events. For this reason the MU liquid scintillator is used to identify incoming muons [33]. Compared to a water Cherenkov veto, the use of a scintillating liquid yields a factor of 30 more photoelectrons per typical muon event and additionally grants the possibility of identifying incoming fast neutrons by their charged secondaries. Furthermore, the scintillation light in comparison to the Cherenkov light is diffuse, which is of advantage for the PMT arrangement at the inner surface of the vessel. Altogether, the inner veto houses 78 PMTs.

- On top, the detector will be covered with the *outer veto*. Consisting of 44 plastic scintillator modules, this veto system does not only provide crucial redundancy for the inner veto in tagging background associated coincidences, but also allows a higher tracking resolution. It can even tag those muons, which merely pass near the detector and might produce fast neutrons.

---

[2]In the following *photomultiplier tube* will often be abbreviated by PMT.
[3]For further information see chapter (4).

4. Organic Liquid Scintillator: Working Principle & Preparation

4.1. Organic Liquid Scintillator

Scintillators are used for the detection of particles and radiation [35]. Incident radiation or particles generate a light signal proportional to the energy they have deposited in the scintillator material. In general, one can distinguish between organic and anorganic scintillators. While anorganic scintillators are usually crystals doped with centers of activation, common organic scintillators are liquids as, for example, the DC scintillator for the muon veto is supposed to be. Charged particles crossing the scintillation medium deposit their energy mainly by electromagnetic interactions leading to the ionization of the state molecules. Besides from energy loss processes known as quenching, this leads to fluorescence light, usually, in the ultraviolet (UV) or the visible range [36, 37].

4.1.1. Scintillation Mechanism

An organic scintillator usually contains hydrocarbons in a structure of benzene [38]. Although the excitation of the strong sigma bonds is also possible, the main contribution to the scintillation light comes from the deexcitation of the π - electrons that are distributed equally and delocalized between each of the six carbon atoms of the ring of benzene [39]. Generally, there are two processes resulting in luminescence light, which differ in their time scale τ of light emission after excitation, as well as in wavelength. While in the case of fluorescence, absorption and excitation are immediately followed by the emission of light ($\tau \approx 10^{-8}$ s), a longer period of time can elapse between absorption and emission in the case of phosphorescence [40, 37].

Processes leading from the absorption of exciting light or excitation by particles to the emission of luminescence light can be explained by energy diagrams known as Jablonski diagrams [41]. A Jablonski diagram shows the energies of the electron transitions, which appear due to the excitation and emission of photons (see fig. (4.1)). Depending on the relative orientation of the spin of the excited electron, that is whether it is parallel or antiparallel compared to the same electron in the ground state, the niveau scheme splits into a singlet and a triplet part [35]. While the energy intervals of the electronic states ($S_0, S_1, ...$) are in a range of
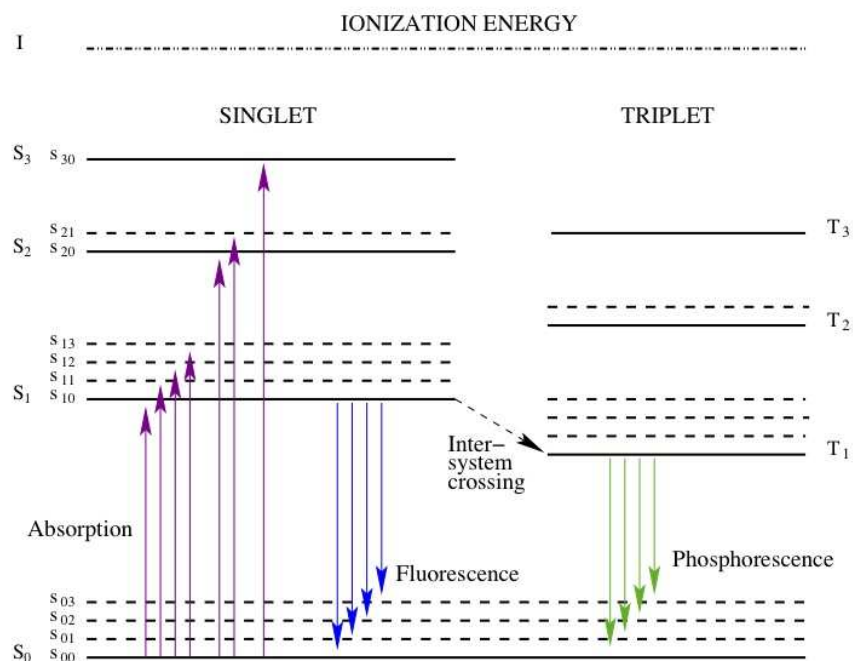
Figure 4.1.: *This Jablonski diagram gives the energy states of the π-electrons in an organic liquid scintillator molecule [40, 37, 42]. The different electron transitions that appear due to the excitation and emission of photons are illustrated. Depending on the relative orientation of the spin of the excited electron (parallel or antiparallel) compared to the same electron in the ground state, the niveau scheme splits up into a singlet ($S_0, S_1, ...$) and a triplet part ($T_1, T_2, ...$). Shown are the electronic states as well as the vibrational sub-levels (dashed lines). Once a molecule has been excited (absorption), the processes of fluorescence and phosphorescence can lead to the emission of luminescence light. Triplet states cannot be populated directly by absorption since electronic transitions in combination with a spin flip are forbidden by the rules of selection. The indirect population, however, is possible for the process of intersystem crossing. Here, the excited electron flips its spin through the interaction with another molecule in the same state of excitation.*

2 eV to 4.5 eV, the energy differences of the vibrational states of the molecules ($S_{00}, S_{01}, S_{02}, ...$) are about 0.1 eV. Although the simple picture of photon absorption by a molecule subsequent by reemission of a photon to give luminescence seems to be quite straightforward, there are nonradiative processes, which compete with photon emission. Populated singlet states, for instance, that are higher in energy than the lowest excited state and any state with excess vibrational energy (such as S_{11} or S_{12}) decay very fast (10^{-12} s) without emission of radiation dissipating energy in the form of heat via collisions with other molecules [42]. Nonradiative transitions between states of the same multiplicity (e.g. $S_1 \rightarrow S_0, S_2 \rightarrow S_1, T_2 \rightarrow T_1$) are referred to as internal conversion or electronic relaxation, whereas the decay of vibrational states (e.g. $S_{00}, S_{01}, S_{02}, ..$) is known as vibrational relaxation.

In a solution these nonradiative processes can occur during a negligibly short period of time [42] through efficient transfer of excess vibrational energy from the solute molecule to the solvent. In a simple organic scintillator molecule, the first effect after an excitation process to a state higher than the lowest electronic one hence is the nonradiative relaxation into the S_1 state. Luminescence light, however, is emitted by the radiative relaxation from the first excited levels into the ground state. The radiative transition from S_1 is referred to as fluorescence. Since the radiationless processes cause losses concerning the conversion of excitation energy to fluorescence light, the emission spectrum, actually, is shifted to longer wavelengths, which is known as *Stokes shift* (see fig. (4.2)) [35, 42]. Neither in the case of absorption nor in the case of fluorescence the spin of the affected electron does change. Electronic transitions in combination with a spin flip are highly forbidden by the rules of selection. As a result triplet states cannot be populated directly by absorption from $S_0 \rightarrow T_1$. This, however, is possible indirectly, either by recombination of ionized molecules, which in 75 % of the cases leads to triplet states [35], or by the so-called process of *intersystem crossing*. For the latter the excited electron has to flip its spin. Therefore, it is only possible through interaction with another molecule in the same state of excitation and occurs with a very low probability. Once the triplet state has been populated, there is the possibility of the relaxation from T_1 to the ground state S_0. As a consequence phosphorescence does occur. The necessary change of spin for this process leads to a comparatively long timescale in the range of microseconds. Most of the times, however, populated triplet states cause delayed luminescence by the transition from S_1 to S_0. For that, the state S_1 has to be repopulated, which is possible due to two processes: Firstly, the state T_1 can acquire thermal energy via collisions until it is sufficient to return to the S_1 state and secondly, two molecules in the same T_1 state can interact giving rise to one S_0 state and one excited singlet state S_1 [35].

4.1.2. Energy Transfer

The emission spectrum of a luminescent significantly overlaps with its own absorption spectrum [42, 43] as can be seen in fig. (4.2). This results in self-absorption of
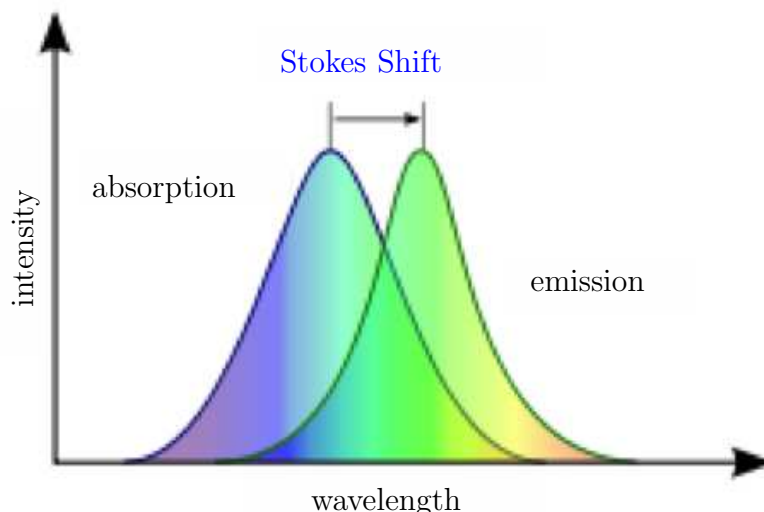
Figure 4.2.: *The figure displays a simplified illustration of the absorption and the emission spectrum of a fluorescent. There is a difference in wavelength, respectively energy, between photons being absorbed and photons being emitted via fluorescence and phosphorescence, which is referred to as Stokes shift. The remaining overlap of the emission spectrum of the fluorescent with its own absorption spectrum is significant and can lead to so - called self - absorption.*

the scintillation light and related to that in a loss of detection information. In order to ensure that the scintillation light still reaches the phototubes being installed at the edge of the detector volume, an organic liquid scintillator usually consists of one or more further fluorescents that are added to the primary solvent. These solutes are called *wavelength shifters* or fluors and shift the scintillation light to longer wavelengths before it is reabsorbed. Therefore, the energy emitted by the solvent has to be transferred to the fluor and - if there is more than one - also from the primary to the secondary fluor. Depending on the concentration and the material several mechanisms of transfer do exist.

Fig. (4.3) illustrates possible processes of energy transfer [37] using the example of singlet spin states S. The picture displays the energy spectra of two solvent molecules in order to explain the interaction between them, both denoted by X, and the energy levels of one solute molecule, denoted by Y. The excitation of the solvent molecule is represented by the purple lines and denoted by A_x and A_y, respectively. Having been brought to an excited electron state, there are several possibilities for the solvent molecule to transfer its energy [37]: At first, the molecule will decay radiationless to the lowest excited electron state S_{1x} releasing energy in the form of heat via collision processes. This is commonly known as internal quenching, whose probability is given by the rate k_{ic} and which is symbolized by the red dashed lines. In this state the molecule could decay to the ground state
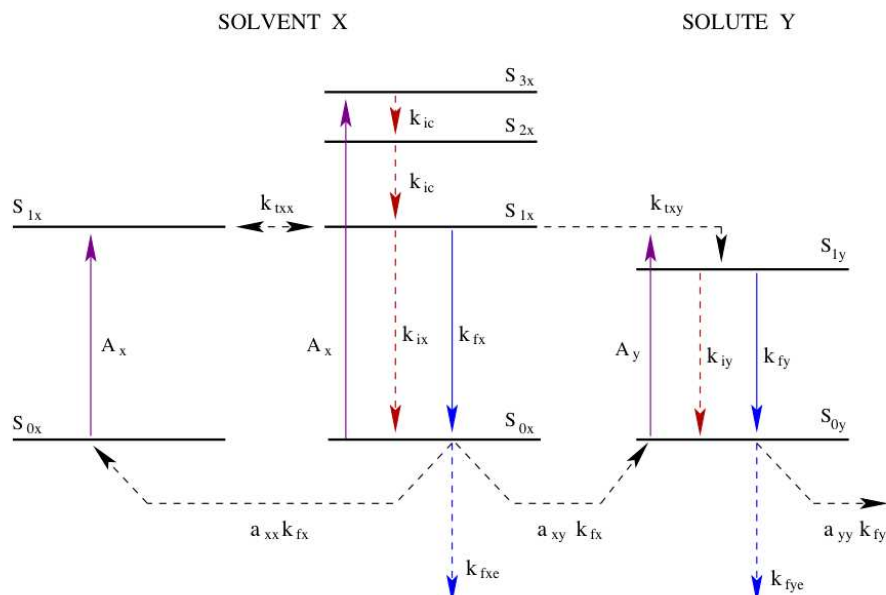
Figure 4.3.: *Energy transfer process illustrated in a two component system with only singlet spin states taken into account. The singlet spin states of the solvent X and the solute Y are shown [35, 37]. Having been excited by absorption (purple lines that are denoted by A_x and A_y), the molecules can decay either radiationless (red dashed lines) or by emitting fluorescence light (blue lines). The rates of the internal conversions thereby are represented by k_{ic} for states higher than the lowest excited one and by k_{ix} or k_{iy} for the first excited states. In the case of the fluorescence processes, the rates are denoted by k_{fx} and k_{fy}. Photons, which escape from the system are denoted by the dashed blue lines (k_{fxe}, k_{fye}). The upper black dashed lines represent energy transfer by collision or dipole-dipole interactions (k_{txx}, k_{txy}) and the lower ones by radiative transfer ($a_{xx}k_{fx}$, $a_{xy}k_{fx}$, $a_{yy}k_{fy}$). For details see text.*

S_{0x}, either again radiationless (red dashed line, with a rate denoted by k_{ix}) or by emitting fluorescence light (blue line, k_{fx}). The latter leads to detectable photons (blue dashed line, denoted by k_{fxe}), although, only to a certain amount as there is still the possibility of reabsorption by another solvent molecule. Apart from these two possible transitions, the energy could also be transferred to another molecule or to the solute. In general, this is possible via collisions, also called *energy hopping* [44], via *dipole-dipole interaction (Förster mechanism)* [40, 45], indicated by the upper black dashed lines (with the rates k_{txx} and k_{txy}) in fig. (4.3), or via radiative energy transfer indicated by the lower black dashed lines (with the rates $a_{xx}k_{fx}$, $a_{xy}k_{fx}$ and $a_{yy}k_{fy}$). In the case of liquid scintillators, the concentration of the solute usually is in the order of a few grams per liter. This is very small compared to the concentration of the solvent. As a result radiative processes can be neglected for the energy transfer from the solvent to the solute [40].

The dipole-dipole transfer can be described by the following formula [45].

$$\kappa = \frac{1}{\tau_{1x}} \left(\frac{R_0}{R} \right)^6 \tag{4.1}$$

Here κ is the dipole-dipole transfer rate between two interacting molecules and τ_{1x} is the radiative lifetime of the donor state, i.e. S_{1x} in fig. (4.3). R is the distance between the interacting molecules and R_0 is a constant describing the overlap between the emission spectrum of the first and the absorption spectrum of the second molecule. Once the solute's state S_{1y} has been populated, there are again the possibilities of radiationless transitions (red dashed line with k_{iy}) and radiative transitions (blue line with k_{fy}). Detectable photons are again denoted by the blue dashed lines and the related rate by k_{fye}. In the case of a secondary or even third wavelength shifter, the energy then has to be transferred further from one solute to the next. Here, radiative processes play the dominating role [46]. Measurements of fluorescence and absorption spectra show that the concentrations of the wavelength shifters usually are too small for an effective nonradiative energy transfer.

4.1.3. Light Output

When a charged particle crosses a scintillator, the main part of its kinetic energy, depending both on particle type and particle energy, is dissipated in the form of heat. Only a small fraction of the particle's energy is converted into fluorescence light. Any process that reduces the fluorescence intensity of a scintillation detector is commonly referred to as the effect of *quenching* (for the quenching factor see sec. (7.1)). Quenching, however, is not an effect of impurities and has to be distinguished from other processes that irreversibly decrease the luminescence such as the presence of oxygen [42]. The response of a scintillator to a charged particle can

be parameterized by the fluorescence energy emitted per unit path length dL/dx applying the semi‑empirical Birks formula [35]:

$$\frac{dL}{dx} = \frac{S\frac{dE}{dx}}{1 + kB\frac{dE}{dx}} \tag{4.2}$$

According to Birks theory, the specific light output dL/dx is related to the energy deposition per unit path length dE/dx. A charged particle is capable of producing a fraction $S \cdot dE/dx$ of excited molecular structures along its track in the scintillator according to the Bethe-Bloch law. These excitations hence are proportional to the specific energy loss with S being the absolute scintillation efficiency. The parameter kB is the Birks quenching factor, a proportionality constant, relating the density of ionization centers to dE/dx. Birks assumes that a fraction represented by $kB \cdot dE/dx$ of the excited molecules along the particles' wake contributes to the quenching effect, which reduces fluorescence intensity.
Consequently, in the absence of quenching, the light yield is proportional to the energy loss. This, for example, is the case for fast electrons directly induced by γ‑radiation, when dE/dx can be assumed small for sufficiently large values of E. The light output per unit path length dx then turns into [42]:

$$\left.\frac{dL}{dx}\right|_e = S\frac{dE}{dx} \tag{4.3}$$

This leads to a constant light output per unit energy loss

$$\left.\frac{dL}{dE}\right|_e = S \tag{4.4}$$

and hence to an absolute light yield proportional to the initial particle energy.

$$L = \int_0^E \frac{dL}{dE'}dE' = SE \tag{4.5}$$

For the same deposition of energy, the scintillation light yield of heavier ions on the other hand, is generally less than the light yield of electrons and γ‑ray interactions, respectively [47, 36]. The reason for this is that for an ion dE/dx becomes large. This approximately gives a specific light output of

$$\left.\frac{dL}{dx}\right|_{ion} = \frac{S}{kB} \tag{4.6}$$

where S and kB are depending on the scintillation medium. Integration results in an absolute light yield of

$$L = \frac{S}{kB} \cdot R \tag{4.7}$$

where R is the range of the considered ion. As a result, the absolute light yield for an ion is proportional to the distance it passes in the scintillator medium. In general, the effect of quenching hence is larger for ions that travel a shorter distance in the scintillator. This distance on the other hand is the shorter, the heavier the ion and thus the higher the specific energy loss. Nevertheless, it has to be emphasized that this is an approximation and experimentally some further dependence of dL/dx on the specific particle type in addition to dE/dx is observed [36]. [1]

4.1.4. Solvent

Linear Alkylbenzene

The solvent is the basic material of a scintillator. For the MU of the Double Chooz detector the decision has been made for linear alkylbenzene (LAB). More precisely, LAB is not a single compound, but a mixture solvent of different alkylbenzenes. Fig. (4.4) illustrates its chemical structure and table (4.1) shows its main properties.

LAB as a scintillator for the Double Chooz experiment offers several advantages including very high purity and transparancy. Moreover, LAB is classified neither as hazardous material nor as ecologically harmful, which makes its handling more plain. It additionally offers a relatively high flash point of $140\,°C$, which is a plus factor referring to safety considerations. Besides, LAB as a common basic material in the detergent industry, is available relatively inexpensive.

LAB from different companies have been under consideration. The companies at choice together with their products and the products' densities are listed in table (4.2). In order to decide between them, the products have been tested on their optical properties (see sec. (5.5.1)) as well as on their density. For the density measurements a digital laboratory density meter of type *DMA 38* from the company *Anton Paar* was used. It is able to measure the density for temperatures ranging from $15°\,C$ to $40°\,C$ with an accuracy of $0.001\,g/cm^3$. The measuring principle of the density meter is based on an electronic measurement of the oscillation frequency: The sample to be measured can be filled into a hollow, U‑shaped glass tube of a certain oscillation capacity. This container then gets electronically excited into undamped oscillations. The eigenfrequency thereby is influenced by the mass

---

[1]The results of this subsection will be used in chapter (7).

of the sample. The density meter measures the corresponding oscillation period with high resolution and, related to that, calculates the density.
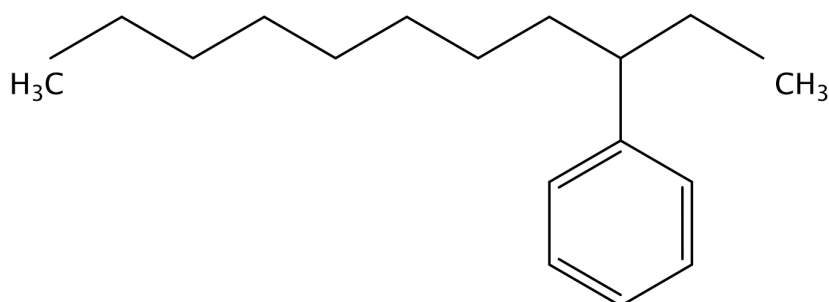
Figure 4.4.: *Chemical structure of LAB. The π - electrons of the ring of benzene are responsible for the emission of scintillation light.*

name	linear alkylbenzene
short name	LAB
molecular formula	$CH_3 - (CH_2)_n - CH[C_6H_5] - (CH_2)_m - CH_3$ $(n + m = 7 - 10)$ $(n, m = 0 - 10)$
CAS-number	67774-74-7 (Helm [48]), 68890-99-3 (Petresa/Cepsa [49])
flash point [°C]	140
absorption [nm]	260
emission [nm]	283

Table 4.1.: *Physical and chemical properties of LAB [50, 51].*

company	product name of LAB	density at 15 °C
Petresa/Cepsa [49]	LAB P-550 Q	0.859 g/cm^3
Wibarco [52]	Wibarcan	0.867 g/cm^3
Helm Spain [48]	LAB	0.860 g/cm^3
Helm Belgium [48]	LAB	0.860 g/cm^3

Table 4.2.: *The table gives the LAB products that have been tested for DC together with their companies and the density measured for 15° C.*

n - Paraffin and Tetradecane

In the special case of the DC experiment a further component is used in addition to the solvent. In order to achieve the desired density of 0.804 g/cm^3 the primary solvent is being diluted with a non - scintillating, non - reactive and highly transparent fluid. It is very important for all detector liquids to have exactly the same density, as the separating walls of the single detector volumes are very thin. They would not be able to withstand too strong buoyancy [53]. At choice were n - paraffins, a mixture of alkanes with common molecular formula C_nH_{2n+2}, where n is between 18 and 32, and tetradecane, higher alkanes with common formula $C_{14}H_{30}$. Fig. (4.5) illustrates the structure of n - paraffins.

Tetradecane with a density of 0.767 g/cm^3 as well as n-paraffins with a density of 0.748 g/cm^3 both provide a lower density than LAB, which has a density of 0.859 g/cm^3. This makes it possible to use both for adapting the required density. Both liquids are non - scintillating and non - reactive. They exhibit high transparency and are ecological harmless, which makes them appropriate candidates. The products again have been tested on their density (see table (4.4)) and their optical properties in order to make a decision. Finally, n - paraffin from CBR has been selected (see sec. (5.5.1)).

$$H_3C \diagdown \qquad \diagup CH_3$$
$$[CH_2]_{n-2}$$
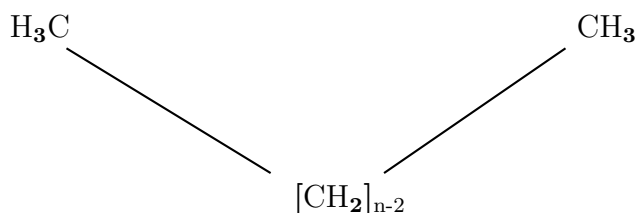
Figure 4.5.: *Chemical structure of n - paraffins with the common molecular formula C_nH_{2n+2}.*

name	n - paraffin	tetradecane
molecular formula	C_nH_{2n+2} with n = 18-32	$C_{14}H_{30}$
CAS-number	64771-72-8	629-59-4
flash point [°C]	70	104

Table 4.3.: *Properties of n - paraffins [54, 55].*

company	name of product	density at 15 °C
Petresa/Cepsa [49]	Petrepar n - C_{14}	0.767 g/cm^3
Wibarco [52]	n - paraffin	0.749 g/cm^3
Helm [48]	n - paraffin	0.749 g/cm^3
CBR [56]	Cobersol C70	0.749 g/cm^3

Table 4.4.: *The table shows the n - paraffins that have been tested for DC together with their companies and the density measured for 15°C.*

4.1.5. Wavelength Shifters

The main emission of the fluorescence and phosphorescence light of organic scintillators covers the UV region. As already mentioned this radiation has a very short reach due to self - absorption by the primary luminescent which is why wavelength shifters are added. These fluors absorb photons of a certain wavelength and reemit them at longer wavelengths (see fig. (4.9) and fig. (4.8)) in a process known as Stokes shift (see sec. (4.1.1)). Besides an absorption spectrum, that has a good overlap with the emission spectrum of the basic material, wavelength shifters should provide a high fluorescence efficiency and high solubility in the basic material. Furthermore, an optimal adaption to the spectral sensibility of the PMTs can be achieved through an appropriate mixture of the scintillator.

For Double Chooz two fluors are used. The primary one is 2,5 - diphenyloxazole (PPO), the second one is 1,4 - bis(2 - methylstyryl) - benzene (bisMSB). Their chemical structures can be seen in fig. (4.7) and fig. (4.6), and their main properties in table (4.5) and table (4.6). The second fluor can be excited by the emission of the primary one, because its maximum absorption lies in the wavelength region of the maximum emission of PPO. The emission maximum of bisMSB then is just about 430 nm as can be seen in fig. (4.8). The shift of the spectrum to longer wavelengths improves the transparency of the scintillator and the acrylic material used for the separation of the detector vessels (transparent at wavelengths larger than about 400 nm [9]). In addition, the efficiency of the PMTs in the region of the bisMSB emission is higher than in the region of the PPO emission.
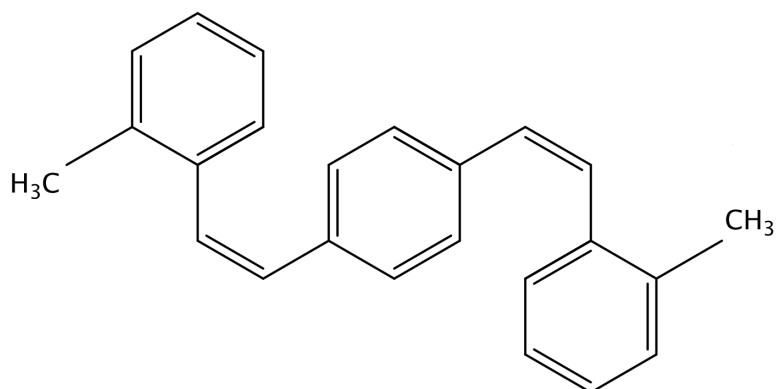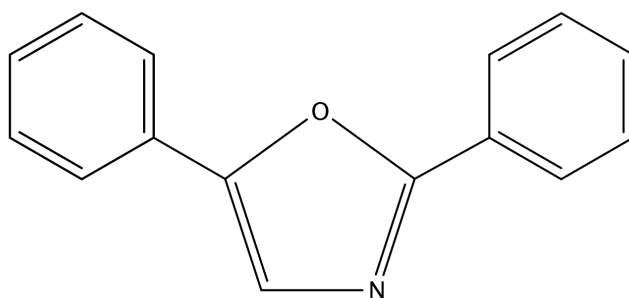
Figure 4.6.: *Chemical structure of the fluor bisMSB.*

Figure 4.7.: *Chemical structure of the fluor PPO.*

name	2,5 - diphenyloxazole
short name	PPO
molecular formula	$C_{15}H_{11}NO$
CAS-number	92-71-7
company	Perkin Elmer [57]
region of absorption	280 nm - 325 nm
region of emission	350 nm - 400 nm

Table 4.5.: *Properties of PPO [58, 59].*

name	1,4-bis(2-methylstyryl)-benzene
short name	bisMSB
molecular formula	$C_{24}H_{22}$
CAS-number	13280-61-0
company	Perkin Elmer [57]
region of absorption	320 nm - 370 nm
region of emission	380 nm - 450 nm

Table 4.6.: *Properties of bisMSB [60, 59].*
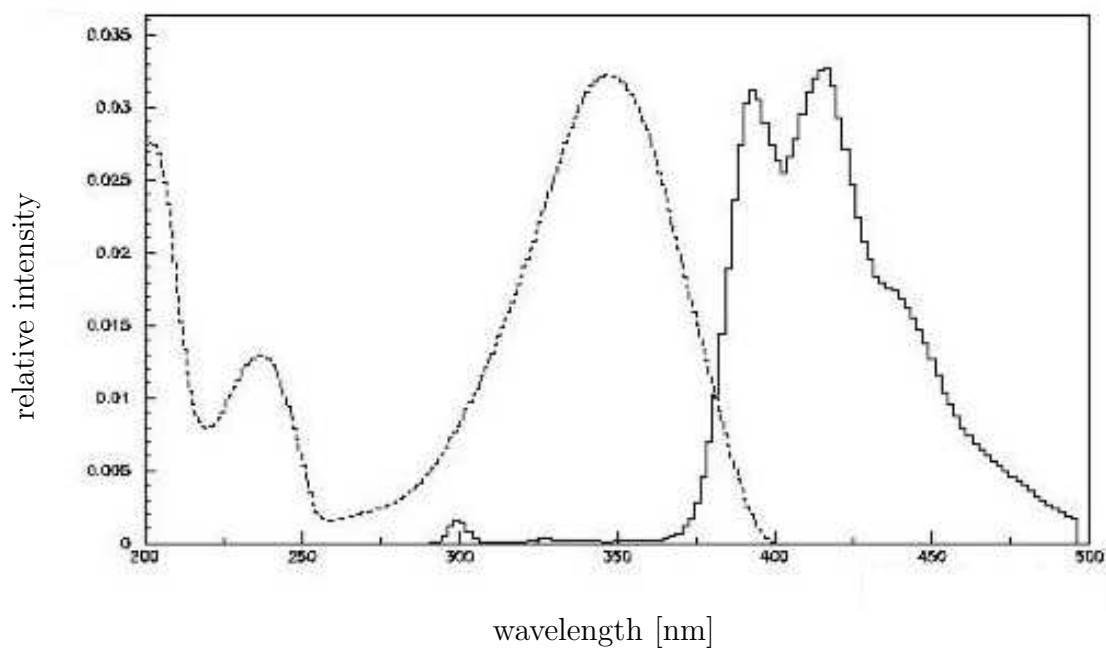
Figure 4.8.: *The plot gives the absorption spectrum (left) and the emission spectrum (right) of the wavelength shifter bisMSB [59]. The effect that the emission spectrum is shifted to larger wavelengths can clearly be noticed.*
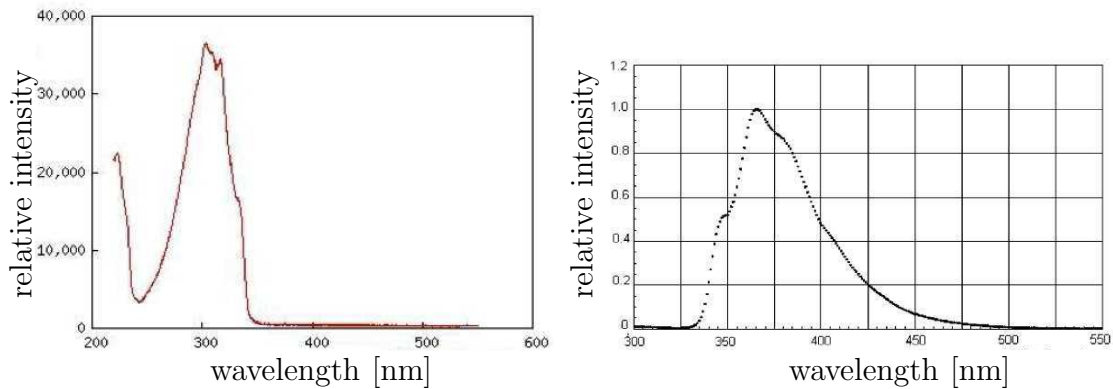
Figure 4.9.: *The plots display the absorption spectrum of the wavelength shifter PPO dissolved in cyclohexane (left) and the emission spectrum of PPO dissolved in pseudocumene (right) [59]. Comparing both one can see that the emission spectrum is shifted to a region of larger wavelengths.*

4.2. Buffer Liquid

The buffer (see sec. (3.3)) is designed to shield the active volume from natural radioactivity. On that account, the buffer volume of each of the two detectors has to be filled with a non-scintillating liquid. Besides the required density of $0.804\,g/cm^3$ (see sec. (4.1.4)), this liquid has to fulfill another crucial condition, namely, high transparency in the wavelength region of the scintillator emission. It has been foreseen to use pure mineral oil for the buffer. Mineral oil is derived from crude oil and mainly composed of alkanes (typically 15 to 40 carbons) and cyclic paraffins. White mineral oil, often referred to as white oil, is crystal clear, odorless and can be found in a variety of different viscosities. Two white mineral oils from the company Shell, Ondina 909 and Ondina 917, have been under investigation. Their characteristic values can be seen in table (4.7). In order to meet the density condition, n-paraffins, just as in the case of the MU scintillator, are added. Mineral oil, as well as different n-paraffins and tetradecane have been tested on their quality concerning their transparency (see sec. (5)). The buffer liquid composition has been foreseen to be 54 % by volume of mineral oil and 46 % by volume of n-paraffins. The decision concerning the buffer liquid has been made in favor of the white mineral oil Ondina 917 from Shell and n-paraffin from the company CBR (see sec. (5.5)).

mineral oil	Ondina 909	Ondina 917
company	Shell	Shell
density at 15 °C	0.825 g/cm^3	0.854 g/cm^3
flash point [°C]	125	200
dynamic viscosity at 20 °C [mPas]	5.1	36
kinematic viscosity at 20 °C [mm^2/s]	6.2	42
kinematic viscosity at 40 °C [mm^2/s]	3.8	18
kinematic viscosity at 100 °C [mm^2/s]	-	3.7

Table 4.7.: *Properties of the mineral oils Ondina 909 and 917 [61, 62].*

4.3. Sample Preparation

For mixing as well as for storing scintillator samples, glassware containers were used, to ensure chemical compatibility. Firstly, the liquid components of the scintillator were mixed, in detail LAB and n‑paraffins or tetradecane. Afterwards, the small amounts of the bisMSB and the PPO powder have been weighed and added. In order to guarantee a complete solution of the powder in the liquid, the mixture was put on a magnetic stirrer for some hours. It has been shown experimentally as well as theoretically that the presence of oxygen in a liquid scintillator has serious influence on the scintillator's optical properties [63]. The so‑called *oxygen quenching effect* [2] in LAB based liquid scintillators can lower the light yield, modify the fluorescence pulse shape and shorten the attenuation length. Therefore, it is of great importance to avoid possible reactions of oxygen, which can be achieved by flushing the samples with nitrogen in order to completely displace the oxygen in the liquid. This should be done after the mixing process of the sample, but also after each tensioning of the scintillator's container.

4.4. Preparation and Mixing of the Liquids for Chooz

The definite composition of the MU scintillator and the buffer liquid can be seen in table (4.8).
As a result of the light yield measurements, the PPO concentration for the MU scintillator has been set to 2 g/l (see sec. (6.6)). With the help of *Wacker Chemie*, a chemical company in Munich, the so‑called *Master Solution* containing the solutes of the DC MU scintillator was mixed. This Master Solution of totaling about

---

[2]Oxygen molecules have a triplet ground state and a singlet state as the next higher one, lying about 0.98 eV over the ground state. In aromatic molecules, the oxygen molecules can absorb the energy of the aromatic molecules' singlet states and make a spin allowed transition to the triplet state, which decreases fluorescence [63].

muon veto scintillator	company	buffer liquid	company
48.4 % vol. LAB	Helm Spain		
51.6 % vol. n-paraffin	CBR	46 % vol. n-paraffin	CBR
2 g/l PPO	Perkin Elmer	54 % vol. Ondina 917	Shell
20 mg/l bisMSB	Perkin Elmer		

Table 4.8.: *Final composition of the Double Chooz muon veto scintillator and the buffer liquid.*

5000 liters consists of LAB and the required wavelength shifters highly concentrated, which means PPO in a concentration of 40 g/l and bisMSB in a concentration of 0.4 g/l. It is not until on site in Chooz that this solution is being diluted by adding n-paraffins and further LAB to reach the favored concentration of 2 g/l PPO and 20 mg/l bisMSB. This method has the advantage that the huge amounts of LAB and n-paraffins can directly be delivered to Chooz by the manufacturing companies. Furthermore, this mixing plan makes it possible to exactly tune in the required density of 0.804 g/l for the scintillator with respect to the local temperature in Chooz. Due to the missing facilities necessary for preparing such huge amounts of liquid, the preparation of the Master Solution was not possible in Garching. The mixing itself took place as follows: The company Petresa delivered 5 ibc containers of 900 liters LAB each and Perkin Elmer delivered the fluors PPO and bisMSB. Firstly, a 1000 liters mixing vessel made of stainless steel was evacuated. Afterwards, LAB of an ibc container was pumped in and bubbled with nitrogen. To facilitate the dissolving of the substances PPO and bisMSB the vessel was heated up to about 50 °C while bubbling with nitrogen and stirring the liquid. As soon as the requested temperature had been reached, which took about one hour, the PPO and the bisMSB were weighed out. To be sure that both substances were completely solved, the LAB was stirred on two to three hours while bubbling with nitrogen. Using a 3 μm filter the final solution was then refilled in the ibc container.

The final mixing of the liquids as well as the adaption of density took place in Chooz, where for that reason three tanks for the MU scintillator and three tanks for the buffer liquid have been installed in the so-called *storage area*. The Master Solution, further LAB as well as the n-paraffins and the mineral oil were transported to Chooz. Once a truck with liquid had arrived, the liquid was filtered before being pumped in the tanks. Each tank features a device in order to flush the liquids with nitrogen from the bottom up. This is not only necessary for displacing the oxygen, but also supports the mixing process. Additionally, the MU tanks as well as the buffer tanks are connected among themselves so that the liquids could be mixed by circulating them.

5. Measurement of the Attenuation Length

5.1. The Attenuation Length

The decrease of intensity of light crossing a scintillator sample can formally be described by the following exponential function [64]:

$$I(x) = I(0) \cdot e^{-x/\Lambda} \tag{5.1}$$

Here, $I(0)$ is the intensity of the incident light, $I(x)$ the intensity of the light ray having covered the distance x and Λ the *attenuation length*, which is to be determined. The attenuation length is composed of both the *scattering length* Λ_{scat} and the *absorption length* Λ_{abs} via

$$\frac{1}{\Lambda} = \frac{1}{\Lambda_{\mathrm{abs}}} + \frac{1}{\Lambda_{\mathrm{scat}}}. \tag{5.2}$$

In spectroscopy, the *absorbance* A^1 as a function of the travelled distance x is defined by [65]:

$$A(x) = \log_{10}\left(\frac{I(0)}{I(x)}\right) \tag{5.3}$$

Eq. (5.1) applied to formula (5.3) results in the attenuation length

$$\Lambda = \frac{x}{A(x)} \cdot \log_{10}(e) \tag{5.4}$$

The attenuation length Λ hence is completely determined by the absorbance A,

---

[1]Absorbance here does not only refer to absorption as in common parlance, but does contain both absorption and scattering.

measurable by a spectrophotometer and the distance x that corresponds to the length of the measuring cell containing the liquid under investigation. In the case of a multi component system, the absorbance A_{total} is the sum of the absorbances of the single components $A_{total} = A_1 + A_2 + A_3 + ...$, which also affects the total attenuation length Λ_{total} [65]:

$$A_{total} = A_1 + A_2 + A_3 + ...$$
(5.5)

$$\frac{1}{\Lambda_{total}} = \frac{1}{\Lambda_1} + \frac{1}{\Lambda_2} + \frac{1}{\Lambda_3} + ...$$
(5.6)

The Lambert-Beer law relates the absorbance of light to the properties of the material through which it is traveling [66]:

$$A = \epsilon \cdot x \cdot c$$
(5.7)

where x is the travelled distance, c the concentration of the absorbing species in the material and ϵ the molar absorptivity, also known as molar extinction coefficient, which in contrast to the absorbance is an intrinsic property of the species. Here, both c and ϵ serve as theoretical description and are no measured variables.

The attenuation length, quantifying light propagation and optical transparency, is one of the key parameters of large-volume liquid scintillation detectors as the ones used in the DC experiment. Absorption and scattering from single molecules of the liquids as well as from possible impurities are competitive processes, which both contribute to the attenuation. In fact, scattered light cannot be traced back to its vertex point, but still contributes to the determination of the overall energy deposited in the medium. In contrast, photons having been absorbed do not arrive at the PMTs surrounding the scintillator volume and thus are lost for detection. For that reason, it is of vital importance for the a scintillator to be transparent to its own emission, to ensure that light of each event reaches the PMTs. In the region of about 430 nm, which is just about the emission maximum of the second wavelength shifter bisMSB (compare sec. (4.1.5)), an attenuation length of more than at least 5 m is required for the MU scintillator [9]. In the case of the buffer, light of the target scintillator, respectively the γ-catcher should be able to cross the buffer in order to arrive at the PMTs at the buffer vessels inner surface, which is illustrated in sec. (3.3), fig. (3.3). Just as for the target and the muon veto, a PPO and bisMSB combination was chosen for the γ-catcher to shift the light into the near UV and optical regions. Therefore, the wavelength regions of interest for the attenuation lengths of the buffer liquid are the same as in the case of the MU

scintillator. For the buffer liquid attenuation lengths of about $6\,\mathrm{m}$ or more are demanded.

5.2. Scattering

Scattering in scintillators mainly consists of two processes: *Rayleigh* and *Mie scattering*.

5.2.1. Rayleigh Scattering

Rayleigh scattering is the elastic scattering of light off particles much smaller than the wavelength λ of the light [67]. In contrast to *Thomson scattering*, which is elastic scattering of electromagnetic radiation off free charged particles, Rayleigh scattering refers to photons that scatter off bound electrons, for example, in the molecules contained in a liquid scintillator. Rayleigh scattering hence is an intrinsic characteristic of organic scintillators and also plays a role in the ideal case of a 100% pure scintillator. In the classical approach the bound electrons thereby are seen as dipol oscillators driven by the electromagnetic waves. In the limit of frequencies of the incident light that are small compared to the resonance frequency ω_0 of those oscillators ($\lambda \gg$ resonance wavelength λ_0), the absolute scattering cross section shows the following $1/\lambda^4$-dependence [68]:

$$
\begin{aligned}
\sigma_{tot}\left(\lambda, \lambda_0\right) \quad &= \quad \frac{8\pi}{3} \cdot \left(\frac{e^2}{4\pi\epsilon_0 m_e c^2}\right)^2 \cdot \frac{\lambda_0^4}{\left(\lambda^2 - \lambda_0^2\right)^2} \\
&\xrightarrow{\lambda \gg \lambda_0} \quad \frac{8\pi}{3} \cdot r_e^2 \cdot \left(\frac{\lambda_0}{\lambda}\right)^4
\end{aligned}
\tag{5.8}
$$

where $r_e = \frac{e^2}{4\pi\epsilon_0 m_e c^2}$ equals the classical electron radius of $2.8\,\mathrm{fm}$. As a consequence, light of shorter wavelengths is scattered much more than that of longer ones. At this point, a further advantage of the fluors added to the scintillator becomes evident: Shifting the light to longer wavelengths, they reduce the contribution of Rayleigh scattering.

5.2.2. Mie Scattering

Another possibility for scattering is Mie scattering [67]. It refers to the scattering of electromagnetic waves off microscopic spheric particles, that have a diameter in the dimension of the wavelength of the radiation. Mie scattering therefore may occur due to impurities like small particles contained in the scintillator. This is the reason why Mie scattering, in contrast to the intrinsic Rayleigh scattering, can be reduced by filtering of the scintillation liquid. For small particle sizes the Mie theory reduces to the Rayleigh approximation.

5.3. Determination of the Attenuation Length

For the attenuation measurements an UV/Vis-spectrophotometer of the type *Perkin Elmer LAMBDA 850* [57] was used. The samples to be examined were filled in a measuring cell consisting of quartz glass of a length of $10\,cm$. The LAMBDA 850 spectrometer features a possible wavelength range that spans from the UV region at $200\,nm$ to the region of the near infrared at $800\,nm$ and has two large sampling compartments. It provides the absorbance of the sample by measuring the attenuation of a light ray crossing the sample relative to a baseline. Therefore, it compares the sample beam (first compartment) with a reference beam (second compartment). The attenuation measurements were performed by comparison with the attenuation of the light ray in air. Typical spectra of the absorbance A_{exp} given by the spectrometer, can be seen in fig. (5.1) for different samples.

For every measurement with the cell, reflections at the boundary layers of the cell between air and quartz glass cannot be avoided. Since air was used as reference, the influence of these reflections on the obtained attenuation had to be considered. According to [64] the reflectivity R, respectively the transmission T is given by

$$R = \left(\frac{n_2 - n_1}{n_2 + n_1} \right)^2 \text{ and } T = 1 - R \tag{5.9}$$

when the light is at near-normal incidence to the interface. n_1 and n_2 are the refractive indices of the boundary layer.

This means that in the case of the cell filled with the sample, reflections at the transition of cell and sample can be neglected, because the refractive index for typical liquid scintillators approximately matches the one of quartz glass, which is $n \approx 1.5$ [64]. As a result only the two glass-air transitions are contributing to an error due to reflectivity. In the case of the empty cell on the other hand, the number of boundary layers contributing to reflection increases by a factor two, because of the two more air-glass transitions at the entering and exit layer of the cell. Neglecting multiple reflections the total transmission for an empty cell with a refractive index for air of $n_{air} = 1$ hence evaluates to $(1 - R)^4 = 0.83$ in a first approximation. This conforms to values obtained by measuring the empty cell with the spectrometer. At $430\,nm$, for example, the obtained absorbance of the empty cell is 0.0598, which corresponds to a transmission of 0.87.

The absorbance spectra obtained by the spectrometer have been corrected for reflections and the influence of quartz glass. A detailed calculation of the method used, as well as an explanation of the assumptions made in the course of this, can be found in the appendix (A). An elaborated description of the method is given in [69].

In the following, the steps of the correction are briefly outlined: Firstly, the empty cell was measured with the spectrometer. Then it was filled with the sample and

measured again. For the correction for additional reflections caused by the two additional air‑glass transitions for the empty cell, half of the absorbance values A_{cell} obtained for the empty cell were subsequently subtracted from the absorbance values A_{exp} obtained for the sample, according to $A'(\lambda) = A_{exp}(\lambda) - \frac{1}{2} \cdot A_{cell}(\lambda)$. For certain wavelengths, the attenuation of the considered sample is very small. Note, that the further proceeding of the method bases on the assumption that at the wavelength with the smallest absorbance value, absorbance is negligible, implicating that the transmission converges to infinity. Having determined the smallest absorbance value of the sample at a wavelength λ_{min}, this wavelength is used as reference. The value of the measurement for every wavelength then is corrected with this smallest value $A_{min}(\lambda_{min})$ using $A(\lambda) = A'(\lambda) - A_{min}(\lambda_{min})$. The resulting value $A(\lambda)$, finally, was used to calculate the attenuation length according to (5.4) [69].

Fig. (5.2) shows the corrected absorbance spectra for different samples. The absorbance $A(\lambda)$ that finally is used to calculate the attenuation length, is plotted versus the wavelength. In order to illustrate typical runs of the different types of liquids measured [2], $A(\lambda)$ of the following samples has been plotted:

- LAB from the company Helm Spain (dark blue)

- MU liquid with LAB from the company Helm Spain (light blue)

- n‑paraffin from the company CBR (red)

- mineral oil, namely Ondina 917 from the company Shell (green)

- buffer liquid with Ondina 917 from the company Shell (pink)

Fig. (5.3) gives the same spectra, but zoomed in. Organic compounds, especially those with a high degree of conjugation[3], absorb light in the UV or visible regions of the electromagnetic spectrum [65]. Just as in the case of the ring of benzene (see sec. 4.1.1), conjugation allows a delocalization of the π‑electrons that no longer belong to single atoms. The electronic molecular states of the π‑electrons split up in different energetic niveaus (see fig. 4.1 in sec. 4.1.1) that can be excited by absorption. A designated energy level corresponds to a certain vibrational and rotational state of the molecule. The fact that vibrational and rotational levels of the molecular orbitals are superimposed upon the electronic levels produces a combination of overlapping lines that appear as a continuous absorption band in the UV/Vis spectrum. The wavelengths of absorption peaks are correlated with the types of bonds in a given molecule. The presence of interfering substances,

---

[2]The results of the measurements of the single samples can be found in sec. (5.5).

[3]In chemistry, conjugation is the overlap of one p-orbital with another, which leads to an intervening sigma bond bridging the interjacent single bonds [39].

however, influences the absorption spectrum [65]. These substances may be added liquids, as in the case of the MU scintillator, or contained organic impurities due to manufacturing process. Furthermore, n-paraffin, for instance, is a mixture of different alkanes. Besides, sample properties like the temperature or experimental variations such as the slit width (effective bandwidth) of the spectrometer will also alter the spectrum.

In the first instance, the runs of the curves look similar. The higher the absorbance values of a curve in the diagram, the lower the attenuation length and hence the transparency. At some lower wavelength each of the spectra starts coming from infinite absorbance. For n-paraffin, Ondina and the buffer liquid this wavelength is at about 340 nm, in other words, these liquids are not transparent at wavelengths smaller than about 340 nm. LAB is not transparent at wavelengths smaller than 400 nm and the MU scintillator already shows no transparency at wavelengths smaller than 420 nm. The latter contains LAB, but additionally n-paraffin and the wavelength shifters PPO and bisMSB. Comparing the point of absolute absorbance of LAB with the one of the scintillator, the influence of the wavelength shifters gets visible. In the case of the scintillator, the point of complete absorbance is shifted to higher wavelengths. Since LAB does not completely absorb before 400 nm, and n-paraffin not before 340 nm, as just mentioned, this can be explained by the additional absorbance of PPO and bisMSB.

For increasing wavelengths, each graph features obvious absorption bands (see fig. (5.3)). All of the samples show a broad peak between 440 nm and 480 nm, which ends in a prominent sharp kink at 480 nm. There is a peak with a maximum at about 497 nm. At about 650 nm all of the curves have further absorption bands and a peak, clearly higher than the other ones (see fig. (5.2)) at about 760 nm. The peaks that can be found for all of the five different samples might be intrinsic to carbon hydrogen, which all of the liquids are based on.

In contrast to the other samples, both LAB and the MU scintillator feature a peak at 608 nm and at 715 nm (fig. (5.3)), which hence must be due to the LAB. These regions of absorbance could be specific to the ring of benzene.

5.4. Error Estimation

For the specification of the uncertainty of the attenuation length, systematical and statistical errors have been estimated.

Statistical Error

In order to investigate the statistical error, each measurement has been repeated at least twice. The resulting curves of the absorbances of the first and a second measurement hardly differ from each other. The statistical error on the attenuation length was calculated to be 1.4 %.
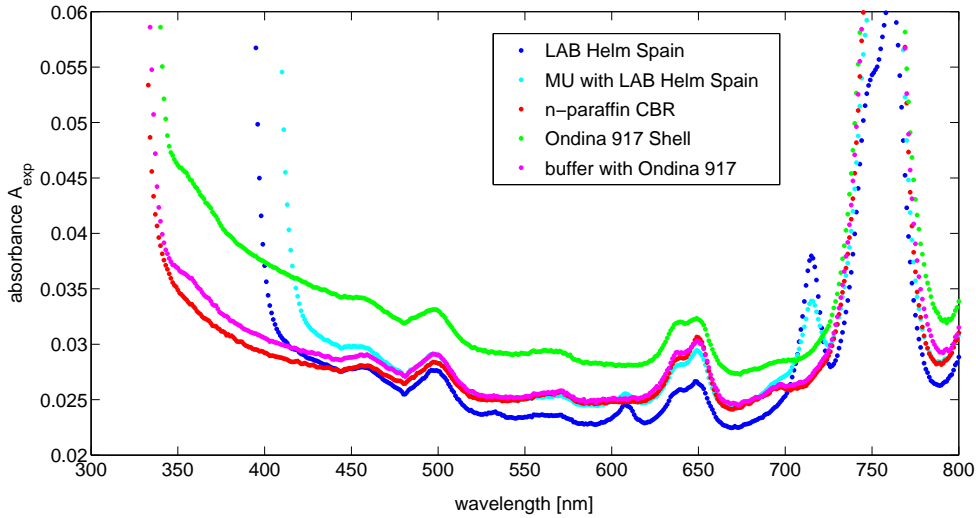
Figure 5.1.: *The plot exemplarily shows typical raw data absorbance spectra obtained with the UV/Vis - spectrometer for different samples. While the x - axis gives the wavelengths, the y - axis shows the measured absorbance A_{exp}. The spectral features are explained in the text.*
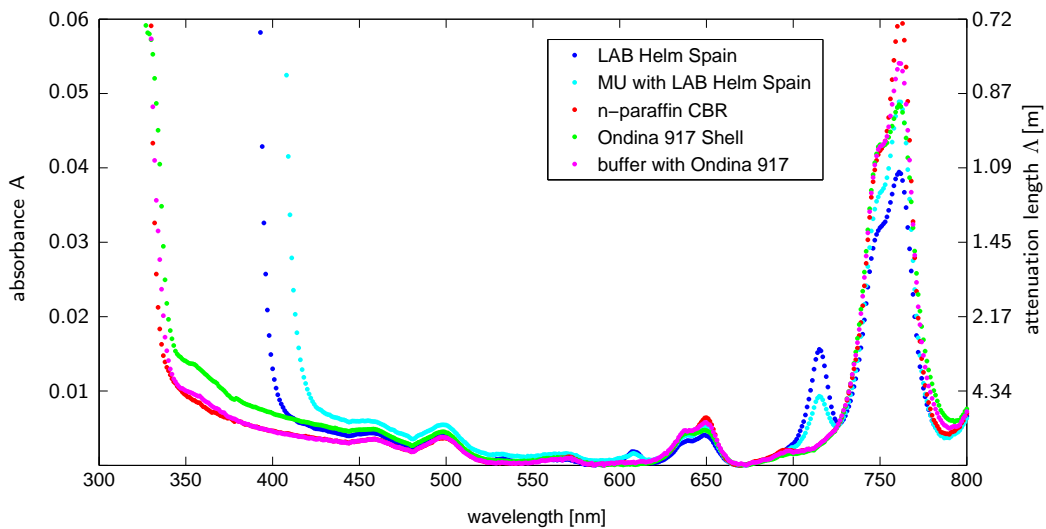
Figure 5.2.: *The absorbance $A_{exp}(\lambda)$ obtained by the spectrometer has been corrected for reflections as described in the text. Here, the resulting absorbance $A(\lambda)$ is given on the left y - axis. The x - axis displays the wavelengths and the right y - axis the corresponding attenuation lengths. An explanation of the spectral features is given in the text.*
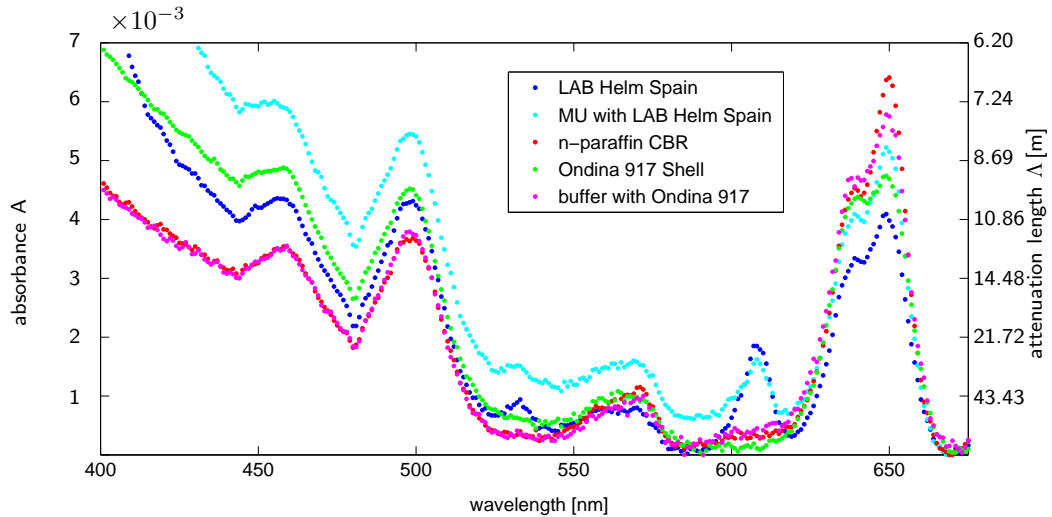
Figure 5.3.: *The plot shows the attenuation spectra of fig. (5.2), but zoomed in. The absorbance A that is used for the calculation of the attenuation length is plotted versus wavelength for different samples. A description of the spectral features can be found in the text.*

Systematical Error

For the contribution to an overall systematical error, the following uncertainties have to be considered:

- The errors in the absorbances obtained by the spectrometer, namely ΔA_{exp} and ΔA_{cell}. According to the technical descriptions and specifications of Perkin Elmer [57], they can be estimated to be about $\pm\,0.0003$ (which is about $\pm\,1\,\%$).

- The impact of an error in the determination of the correct position of λ_{min}.

- An error due to the assumption of maximal transmission at the position of the reference wavelength λ_{min}.

While errors in the measured absorbances have been specified by the company of the spectrometer, one has to put a finer point on a possible error due to the determination of the λ_{min}-position and the assumption made for the attenuation at λ_{min}.

For a start, the impact of an uncertainty in the position of λ_{min} has been examined. In fig. (5.4) the absorbance $A'(\lambda)$, whose minimum is searched for in the course of the used corrections (see sec. (5.3) and the appendix (A))) is plotted for different types of samples. Although, the runs of the curves differ in local peaks, minima,

maxima and slopes, it can easily be seen that they all show their global minimum in a wavelength range from about 660 nm to 680 nm. For different samples of one type, the curves are more or less the same, only shifted in the direction of the y‑axis depending on their transparency. This means the minima are quite well‑marked, in so far as there should not be another global minimum in a region of wavelengths completely different from the 660 nm to 680 nm range. Fig. (5.5), for instance, shows the absorbance $A'(\lambda)$ for different LAB samples. For LAB from the company Helm in Spain (red curve) the minimum can be found at a wavelength of 669 nm. The resulting attenuation length at 430 nm, determined with the method of sec. (5.3), is 9.09 m. Using this example, the error in the calculated attenuation length depending on a deviation d from the correct minimum position λ_{min} has been worked out. Fig. (5.6) illustrates this error. The x‑axis gives the deviation from the minimum position and the y‑axis the error in the attenuation length. This error increases with growing deviation from λ_{min} both in the direction towards higher and lower wavelengths. A deviation from the correct λ_{min}‑position of about ‑5 nm or +7.5 nm, for example, would lead to an error of 6 % (red dashed line). Variations like less than ‑6 nm or more than +10 nm would yield errors of more than 10 % (green dashed line). An error in the determination of the correct λ_{min}‑position could indeed occur for two reasons:

Firstly, the spectrometer has a wavelength inaccuracy, which might shift the minimum in x‑direction. According to Perkin Elmer this inaccuracy is ±0.08 nm. The attenuation lengths within this range of λ_{min}‑wavelengths have been calculated. The resulting errors in the attenuation length, however, are very small with less than 1 %.

Secondly, statistical fluctuations could have the effect that a different minimum from A_{min} suddenly becomes the global minimum. Considering fig. (5.6), however, the region of deviations in which this effect might appear can be estimated to be from about -4 nm to $+4$ nm. Outside this range the curve towards higher and lower wavelengths, respectively, steeply inclines so that statistical fluctuations do no longer pose a problem. The resulting error in the attenuation length hence is estimated to about 4 % (black dashed line in fig. (5.6)).

The main contribution to the systematic uncertainty, however, might originate from the assumptions made for the calculation of the attenuation length. As mentioned before, λ_{min} is used as reference wavelength and the attenuation for the corresponding absorbance A_{min} is assumed to be zero (equals a 100 % transmittance or an infinite attenuation length). Due to the fact that the entire calculation that follows is based on this assumption for the lowest absorbance A_{min}, the question arises, whether and to what extent a different assumption implicates a critical systematic error. As already mentioned, LAB from Helm in Spain (red curve in fig. 5.5) has an attenuation length of 9.09 m at 430 nm. To simplify matters, this attenuation length will be referred to as Λ_{LAB} in the following. For its calculation the atten-
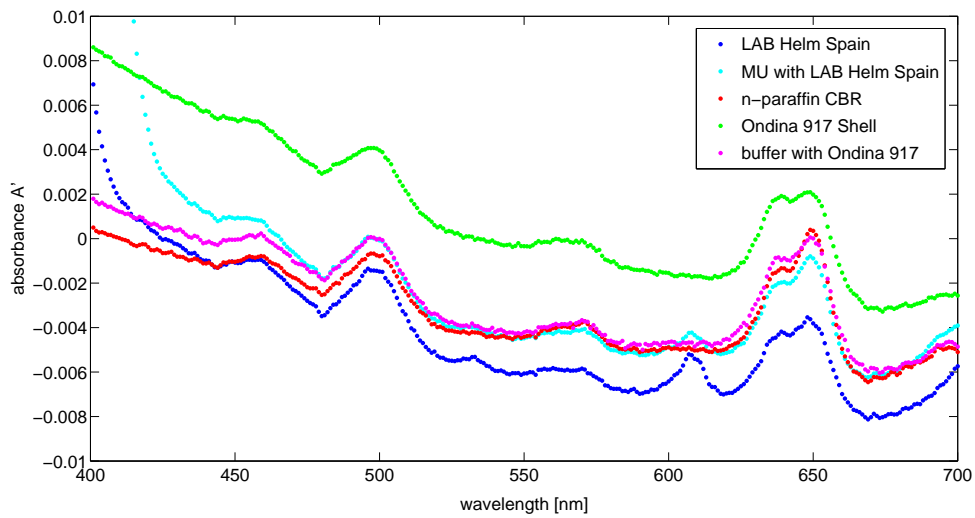
Figure 5.4.: *The absorbance $A'(\lambda)$ that, in the course of the used corrections (see sec. (5.3)), has been obtained by subtracting half of the absorbance values for the empty cell, is plotted for different types of samples. Depending on the type of liquid, the curves run differently, but for all of them an absolute minimum can be found in the wavelength range from about 660 nm to 680 nm.*
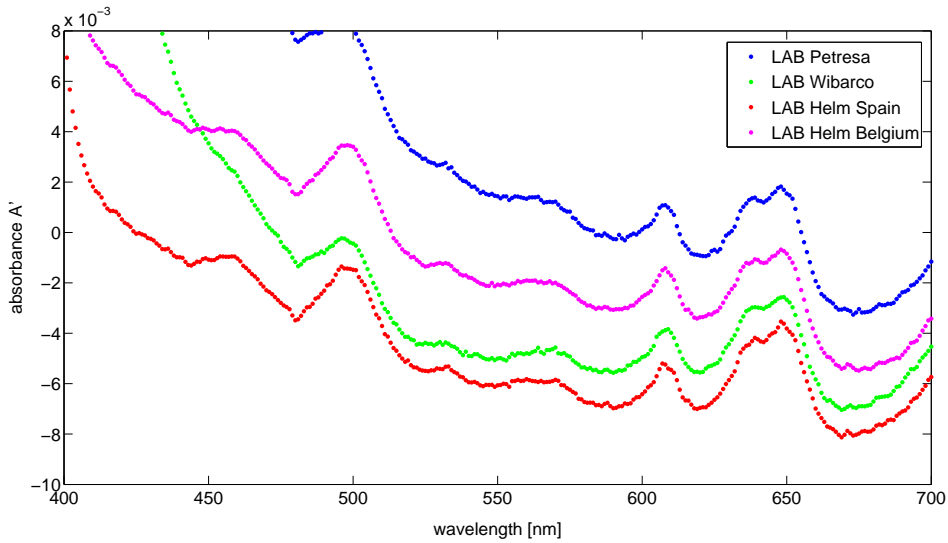
Figure 5.5.: *The absorbance $A'(\lambda)$, obtained by subtracting half of the absorbance values for the empty cell (see sec. (5.3)) is plotted for different LAB samples. The run of the different curves is more or less the same, only shifted in y-direction depending on their transparency. The absolute minimum for the LAB from Helm Spain (red graph), can be found at a wavelength of 669 nm. This is also the range, where the other samples have their absolute minimum.*
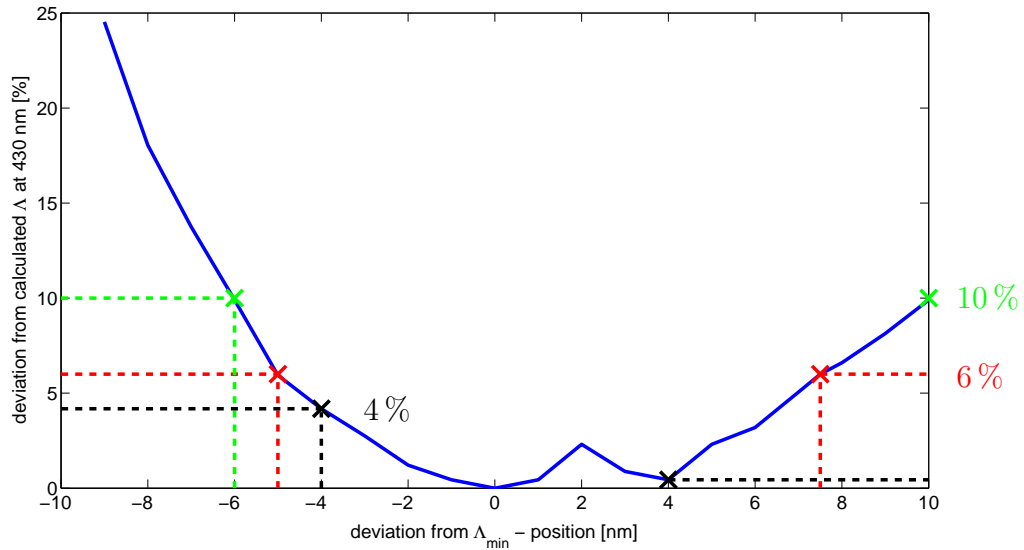
Figure 5.6.: *For the calculation of the attenuation length Λ, λ_{min} is used as reference as described in sec. (5.3). This plot illustrates the systematic error due to an uncertainty in the determination of the position of λ_{min}. The error in Λ is plotted versus the deviation from the correct λ_{min}-position (blue line). Deviations resulting in an error of 4%, 6% and 10% are marked.*

43

uation length at λ_{min} has been assumed to be infinite. In order to investigate the influence of different assumptions on Λ_{LAB}, the attenuation length has also been calculated for different assumed attenuation lengths (respectively transmittances) at λ_{min}. The resulting deviation from Λ_{LAB} has been plotted versus the assumed attenuation length Λ at λ_{min} (fig. (5.7)) and versus the assumed transmittance (fig. (5.8)). The graph in fig. (5.7) starts at zero and does not begin to rise before 1000 m. At an assumed Λ of 100 m the deviation from Λ_{LAB}, for example, has reached 8 %. For an assumed Λ of 50 m the deviation is already 15 %. The error rises very fast and the resulting attenuation lengths hence are strongly dependent on the assumption for A_{min}.

Dodecane, however, has been measured in [59] using a different experimental setup that is not based on such an assumption. With 3.65 ± 0.04 at 430 nm, Λ obtained there is in good agreement with the length of 3.87 nm measured with the spectrometer. This fact argues in favor of the method used. Its systematic error thus has been estimated to 5 %.

The total error for the attenuation length has been calculated by gaussian error propagation to be 9 %.
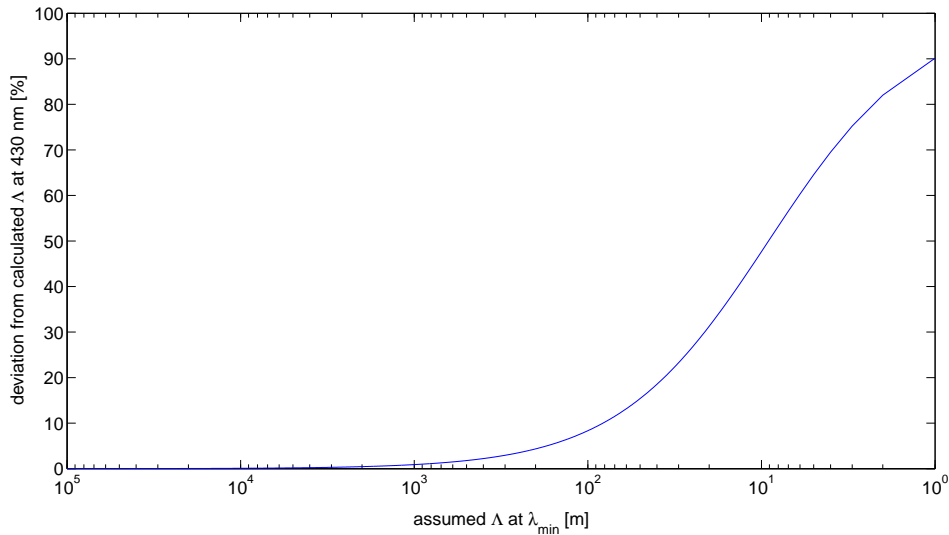
Figure 5.7.: *The systematic error due to the assumption made for the smallest oc-curring absorbance value A_{min} in the calculation of the attenuation length Λ is illustrated. In the method used, Λ at 430 nm (Λ_{LAB}) was obtained by assuming Λ at the position of A_{min} to be infinite. Here, the x - axis displays different assumptions for Λ at the position of A_{min}. For each of these assumptions, Λ at 430 nm has been calculated. Their deviation from Λ_{LAB} is plotted on the y - axis. The run of the graph does not start to increase before about 1000 m on the x - axis, but then rises very fast. The resulting Λ at 430 nm hence strongly depends on the assumptions made for Λ at λ_{min}. The error in the calculated Λ is clearly dominated by this systematic uncertainty.*
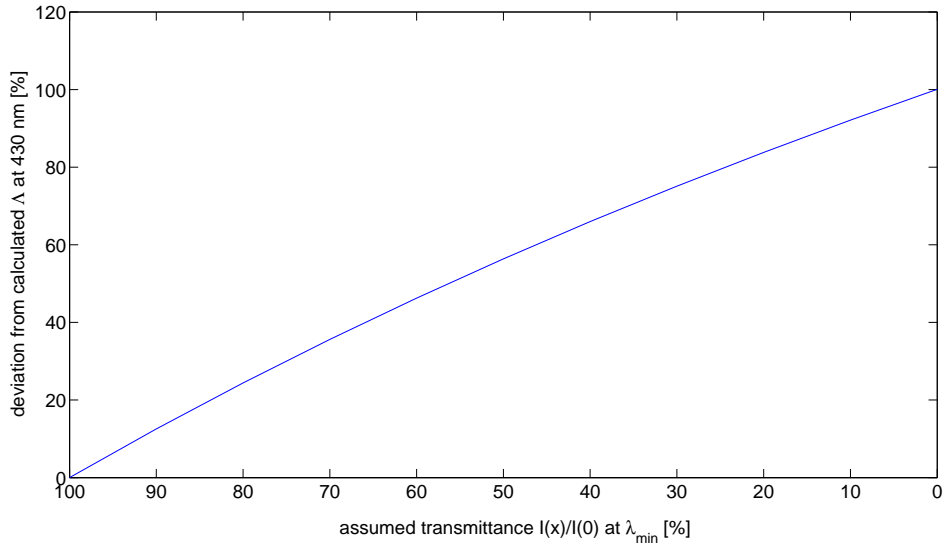
Figure 5.8.: *The systematic error due to the assumption made for the smallest occurring absorbance value A_{min} in the calculation of the attenuation length Λ is illustrated. In the method used, Λ at 430 nm (Λ_{LAB}) was obtained by assuming Λ at the position of A_{min} to be infinite. This equals an assumed transmittance T of 100 %. The x - axis gives different assumptions for T at λ_{min}. For each of these assumptions, Λ at 430 nm has been calculated. Its deviation from Λ_{LAB} is plotted on the y - axis. For an assumed T of 84 %, for example, the deviation already is 20 %. The resulting Λ at 430 nm hence strongly depends on the assumptions made for T or Λ at λ_{min}. This systematic uncertainty is the main contribution to the error in the calculated Λ.*

5.5. Results

5.5.1. Muon Veto Scintillator and Components

Attenuation Length of LAB

In order to obtain a MU scintillator with an attenuation length higher than 5 m, the attenuation lengths of the single components, namely LAB and n‑paraffin, should be as high as possible. LAB is not a single compound, but a mixture of different alkylbenzenes. As a petrochemical product, it also contains about $0.5\% - 3\%$ complex chemical impurities [70]. These impurities may greatly influence the optical properties of the liquid scintillator, i.e. decrease the light attenuation length of the solvent in the 400‑450 nm characteristic window. Regarding the selection of LAB for the scintillator, LAB samples provided by different companies were tested on their attenuation lengths. Fig. (5.9) gives an overview of the attenuation spectra measured with the UV/Vis spectrometer for the wavelengths of interest (emission of scintillator) and table (5.1) shows the corresponding attenuation lengths. While the results for the LAB of the companies Petresa and Wibarco with attenuation lengths between 2.15 m to 4.00 m do not meet the requirements for the DC MU scintillator (compare to section (5.1)), the resulting attenuation lengths for LAB of the company Helm exceed 6 m and therefore seem to be eligible candidates. Both LAB Helm Spain and Belgium are from the same company and hence manufacturing process, only from different locations of production. That they nonetheless show a difference in their attenuation length must be traced back to sampling, handling and transport at the respective location. This, however, is an effect that cannot be avoided and also occurs for samples of the same location of production when they are from different charges. Since Helm offered both LAB from Belgium and Spain at the same price, the decision finally has been made for the LAB of Helm Spain due to its slightly better results.

Attenuation Length of n-Paraffins and Tetradecane

N-paraffins, respectively tetradecane, are kown to be very transparent. For both the MU scintillator and the buffer liquid, several products were tested on their attenuation lengths in order to make a decision. Fig. (5.10) gives an overview over the attenuation spectra measured with the UV/Vis spectrometer and table (5.2) shows the attenuation lengths at 420 nm, 430 nm and 440 nm. The resulting lengths for all of the n‑paraffins are very high. In the considered region of wavelengths all of them far exceed 10 m. Their high transparency is demonstrated by the low absorbance lines that all lie close together. The tetradecane from Petresa, on the other hand is less transparent. At 430 nm its attenuation length is shorter than 5 m. Its absorbance graph runs different from the others. Coming from higher absorbance values at 400 nm, it is decreasing for increasing wavelengths, but still does not reach the low absorbance levels of the n‑paraffins. All n‑paraffins were
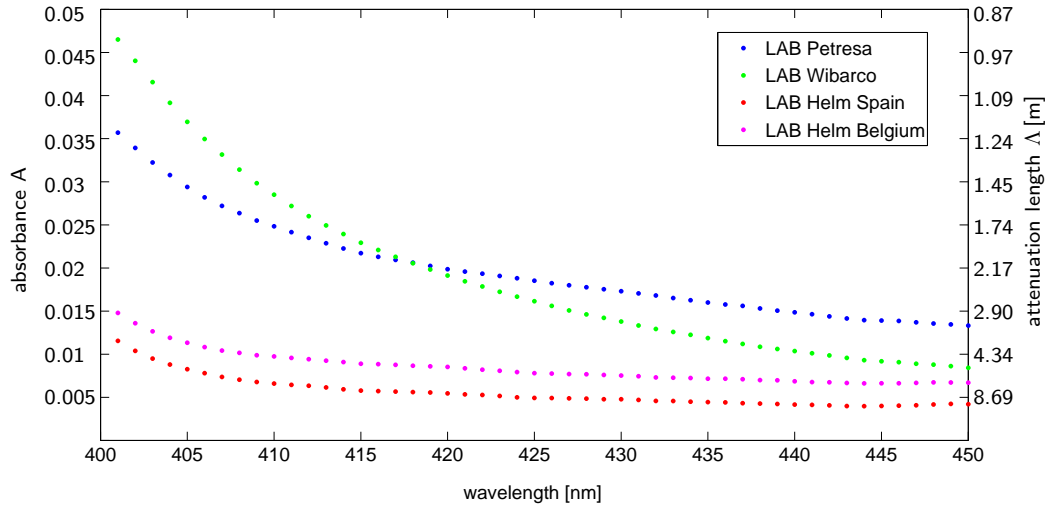
Figure 5.9.: *The absorbance A of different LAB samples is plotted versus the wavelength. The corresponding attenuation length is given by the right y-axis. The higher A, the higher the attenuation and the lower Λ. The best results, exceeding 8 m, were obtained with the LAB from the company Helm Spain. The curve of the LAB from Helm in Belgium runs similar to the one from Helm Spain, but shifted to higher absorbances. This close resemblance is due to the fact that actually both LAB Helm Spain and Belgium is from the same company and hence manufacturing process only from different locations of production. The resulting attenuation lengths are lower than 8 m, but with 6 m to 7 m still close to the result of the LAB from Helm Spain. That they nonetheless show a difference in their Λ must be traced back to sampling, handling and transport at the respective location. The spectra of the LAB from Petresa and Wibarco yield attenuation lengths of about 3 m, which is far from the lengths of the others. As described in the text, LAB contains chemical impurities due to the manufacturing process, which results in the differences of Λ for the different samples. The decision has been made for LAB Helm Spain which was the most transparent liquid.*

transparent enough to be used for Double Chooz. Due to a better offer and for logistic reasons, the decision has finally been made for the company CBR.
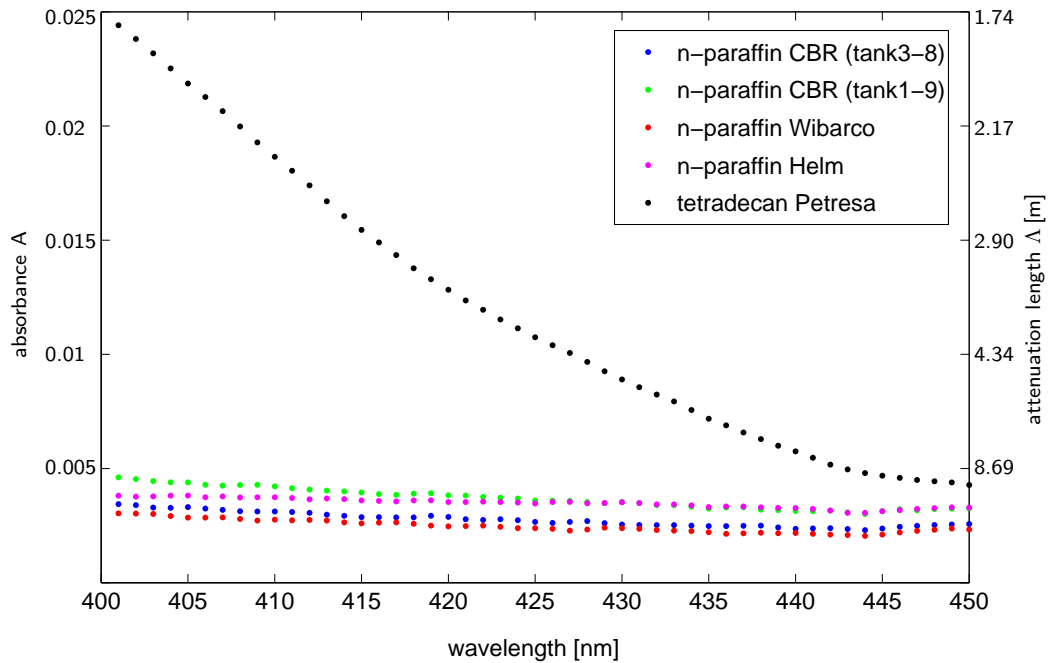
Figure 5.10.: *The absorbance A of different n-paraffins and tetradecane is plotted versus the wavelength. The corresponding Λ is given by the right y-axis. All n-paraffin samples show similar curves resulting in very good attenuation lengths exceeding 10 m. The graph for tetradecane obviously runs different from the others. Starting from a higher absorbance than the other samples, it is steeply falling off with increasing wavelength, but never reaches absorbances as low as the ones of the n-paraffins.*

company	Λ_{420} [m]	Λ_{430} [m]	Λ_{440} [m]
Helm Belgium	6.18 ± 0.56	7.14 ± 0.64	7.98 ± 0.72
Helm Spain	8.36 ± 0.75	9.73 ± 0.88	11.25 ± 1.01
Petresa	2.29 ± 0.20	2.64 ± 0.24	3.08 ± 0.28
Wibarco	2.15 ± 0.19	3.00 ± 0.27	4.00 ± 0.36

Table 5.1.: *The table gives the attenuation lengths of different LAB samples. LAB from the company Helm both located in Belgium and in Spain shows very good results, whereas the LAB from Petresa and Wibarco with less than 4 m is not that transparent. Due to its high transparency the decision has been made for LAB Helm Spain.*

product	company	Λ_{420} [m]	Λ_{430} [m]	Λ_{440} [m]
n-paraffin	CBR (1-9)	10.73 ± 0.97	11.65 ± 1.05	12.40 ± 1.12
n-paraffin	CBR (3-8)	15.50 ± 1.40	17.17 ± 1.55	19.13 ± 1.72
n-paraffin	Helm	12.40 ± 1.12	12.46 ± 1.12	12.32 ± 1.11
n-paraffin	Wibarco	19.34 ± 1.74	20.68 ± 1.86	22.15 ± 1.99
tetradecane	Petresa	3.23 ± 0.29	4.57 ± 0.41	6.95 ± 0.63

Table 5.2.: *The table gives the attenuation lengths at the wavelengths 420 nm, 430 nm and 440 nm, for different n‑paraffins and tetradecane. In the case of the n‑paraffin from CBR, (1‑9) and (3‑8) are internal labels of the company indicating the number of the tanks the sample has been taken from. All n‑paraffin samples show very good results exceeding 10 m. The lengths for tetradecane from Petresa are significantly shorter.*

Attenuation Length of the Muon Veto Scintillator

Initially, the idea was to use LAB and tetradecane from Petresa for the MU scintillator. The PPO concentration had not been fixed yet, whereas the bisMSB concentration was set to be 20 mg/l. Scintillator samples in a concentration of 37.5 % vol. LAB, 62.5 % vol. tetradecane, 20 mg/l bisMSB and PPO in different concentrations were prepared and measured. At this, the percentage of LAB and tetradecane is given by the required density (see sec. (4)). Table (5.3) gives an overview of the attenuation length for the wavelength of 430 nm and the density that has been measured using the density meter described in sec. (4.1.4). With increasing PPO concentration the attenuation length tends to decrease. At a concentration of 1.0 g/l the attenuation length is 4.08 m. At a fourfold increase of the PPO concentration, the attenuation length falls by 20 %. Although 430 nm does not lie in the region of maximal absorption of PPO, which is 280 nm to 325 nm (compare sec. (4.1.5)), PPO still absorbs at 430 nm. The increasing attenuation with increasing concentration must be an effect due to self‑absorption of the PPO. Due to the LAB measurements it turned out that LAB from other companies did show higher attenuation lengths (see sec. 5.5.1). In order to decide on the products used for the scintillator liquid, it is practically sufficient to measure the single components. If two components both show high transparency, this is also applies to a mixture of them. In the course of the attenuation measurements, the decision had been made for LAB from the company Helm Spain and n‑paraffin from CBR. As a cross check, however, some MU scintillator samples with LAB and n‑paraffin from different companies with an PPO concentration of 2 g/l PPO and 20 mg/l bisMSB were mixed and tested on their attenuation. The measured absorbance spectra and the calculated attenuation lengths can be seen in fig. (5.11) and table (5.4). The best results again have been obtained with the LAB from the company Helm. Both in the case of being mixed to n‑paraffin CBR as well as to n‑paraffin Helm, a required length of more than 5 m at 430 nm was achieved. With the products from Petresa and Wibarco on the other hand, a length of more than 5 m could not be attained. In the case of the Petresa products, this is apparent since the results of the single components did not reach the 5 m limit. Concerning the Wibarco scintillator, the poor result most probably is the influence of the LAB since the measurement of the Wibarco LAB yielded an attenuation length of only 3 m, whereas the n‑paraffin was very transparent with more than 20 m.

PPO concentration [g/l]	Λ_{420} [m]	density [g/cm^3]
1.0	4.08 ± 0.37	0.8018
1.5	4.08 ± 0.37	0.8019
2.0	4.10 ± 0.37	0.8020
2.5	3.36 ± 0.30	0.8022
3.0	3.38 ± 0.30	0.8022
3.5	3.31 ± 0.30	0.8025
4.0	3.23 ± 0.29	0.8027

Table 5.3.: *The table gives the attenuation lengths Λ for the MU scintillator with fixed components 37.5 % vol. LAB, 62.5 % vol. tetradecane, 20 mg/l bisMSB and a varying PPO concentration. Also shown is the density which has been measured with a density meter. For an increasing PPO concentration, respectively density, Λ tends to decrease. This must be due to self-absorption of PPO.*

company of LAB	company of n-paraffin/tetradecane	Λ_{420} [m]	Λ_{430} [m]	Λ_{440} [m]
Helm (Belgium)	CBR	4.39 ± 0.40	5.55 ± 0.50	6.38 ± 0.57
Helm (Spain)	Helm	5.30 ± 0.48	7.77 ± 0.70	9.04 ± 0.81
Petresa	Petresa	2.84 ± 0.26	4.33 ± 0.39	6.00 ± 0.54
Wibarco	Wibarco	2.94 ± 0.26	4.42 ± 0.40	5.49 ± 0.49

Table 5.4.: *The table gives the attenuation lengths Λ at the wavelengths 420 nm, 430 nm and 440 nm, calculated for MU scintillators with products from different companies. In case of CBR, Helm and Wibarco n-paraffin was added to the LAB, while it was tetradecane in the case of Petresa. Both liquids with the LAB Helm Spain and the one with the LAB Helm Belgium have the required attenuation length of more than 5 m. The attenuation lengths of the scintillator with LAB from Petresa and Wibarco are shorter.*
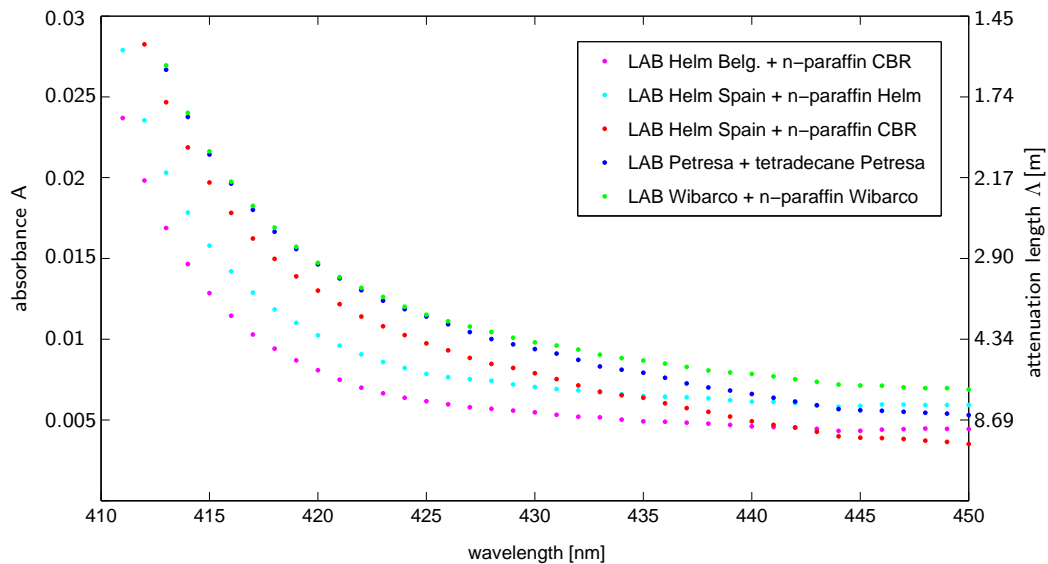
Figure 5.11.: *The absorbance A for MU scintillators with LAB as well as n - paraffin from different companies is plotted versus the wavelength. In the region of 420 nm to 440 nm the lowest absorbances and the highest attenuation lengths, respectively, were reached with the mixture LAB Helm Spain and n - paraffin CBR, LAB Helm Spain and n - paraffin Helm as well as LAB Helm Belgium and n - paraffin CBR. The transparency of the mixtures LAB and n - paraffin Wibarco as well as LAB and tetradecane Petresa turned out to be lower. Due to measurements of the single components the decision had been made for LAB Helm Spain and n - paraffin CBR. The mixed scintillator of both components shows the desired attenuation lengths of more than 5 m which confirms the decision.*

5.5.2. Buffer Liquid and Ondina

Attenuation Length of Ondina

Mineral oil from the company Shell, namely Ondina 909 and Ondina 917, has been tested on its transparency. While fig. (5.12) shows the obtained absorbance spectra, table (5.5) gives the corresponding attenuation lengths. Ondina 909 06 and Ondina 909 08 indicate that the sample was taken in 2006, respectively 2008, whereas february and april refer to the month of delivery in 2010. Ondina 909 as well as Ondina 917 february show very good results. Ondina 917 april, however, with an attenuation length of only 3.32 m at 430 nm, does not meet the requirement of an attenuation length of more than 6 m. Ondina 917 and Ondina 909 are both white mineral oils that mostly differ in their viscosity (see sec. (4.2)). They therefore should feature attenuation lengths in the same order, which is true except for the Ondina 917 april sample. Ondina 917 from february and april should even be the same product, only received at another time. Due to the fact, that both samples have passed the same manufacturing process, the difference in their attenuation lengths might be traced back to the sampling at Shell, transport or to a contamination after delivery. Since Ondina 909 was discontinued by Shell, Ondina 917 was selected. Barring the april sample, the attenuation lengths of Ondina 917 are sufficient.

Attenuation Length of the Buffer Liquid

Based on the measurements of the single components, the decision in the case of the buffer liquid has been made for Ondina 917 from Shell and n‑paraffin from the company CBR. In the case of two components featuring high transparency, the high transparency also applies to the mixture of both provided that it is not contaminated during the mixture process. Nevertheless, some different buffer samples mixed with the mineral oil Ondina 917 from Shell and n‑paraffin from Wibarco and Helm as well as Ondina 909 from Shell and tetradecane from Petresa have been measured. In fig. (5.13) you see the results for the absorbance spectra. Both curves for the buffer liquids with Ondina 917 run similarly. They result in attenuation lengths of more than 11 m for the one with n‑paraffin from Wibarco and in lengths of more than 7 m for the one with n‑paraffin from Helm. Therefore, both liquids are very transparent exceeding the required 6 m attenuation length. The curve of the buffer liquid mixed with Ondina 909 and tetradecane from Petresa, on the other hand, runs different from the others. It is shifted to higher absorbance values and shows a steep decline for increasing wavelengths. The attenuation lengths at 420 nm, 430 nm and 440 nm can be seen in fig. (5.6). Due to the attenuation lengths exceeding 9 m that have been measured for Ondina 909 (see subsec. (5.5.2)), the low lengths that have been achieved with the Ondina 909 and tetradecance mixture, might be due to the lower lengths measured for tetradecane (see subsec. (5.5.1)).
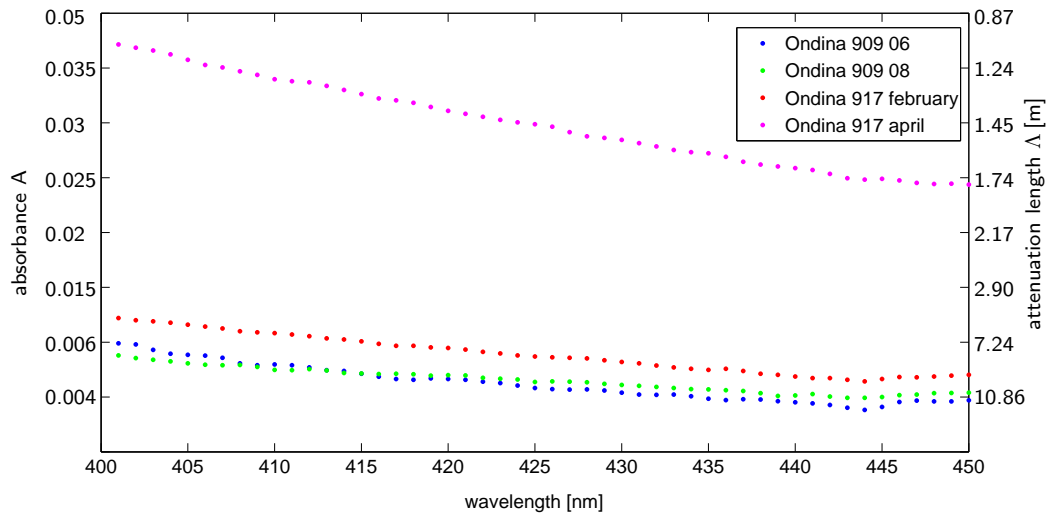
Figure 5.12.: *The absorbance spectra of different mineral oils are plotted versus wavelength. Ondina 909 and Ondina 917 are two types of white mineral oil from Shell that mostly differ in their viscosity. While 06 and 08 indicate the year of sampling for Ondina 909, Ondina 917 was produced in 2010 and april, respectively february, denotes the month they have been received. Ondina 909 shows better results than Ondina 917. Ondina 917 (february) is still very transparent, but Ondina 917 (april) does not meet the required Λ of 6 m. Both Ondina 917 samples should actually be the same product, the difference in their results might be traced back to some contamination after the production process.*
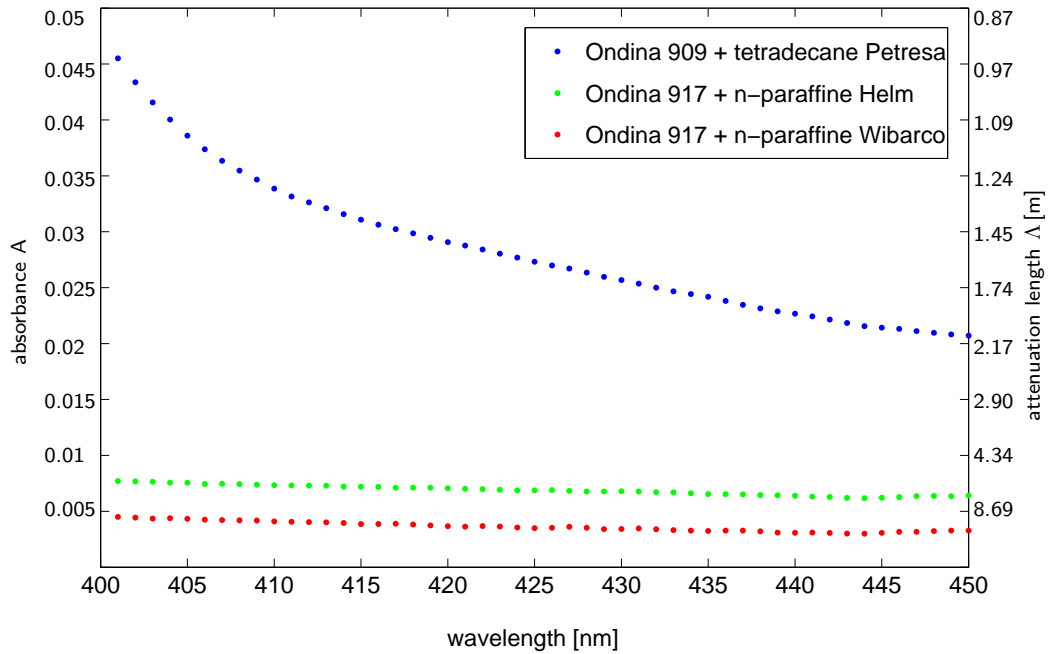
Figure 5.13.: *The absorbance spectra of different buffer liquids are plotted versus wavelength. The lowest absorbance was achieved with the mineral oil Ondina 917 from the company Shell and n‑paraffin from Wibarco resulting in a Λ of more than 11 m for the wavelength range shown in this plot. The buffer liquid with Ondina 917 and n‑paraffin from Helm also meets the requirement of a Λ of more than 6 m. This does not apply to the mixture of Ondina 909 and tetradecane from Petresa, whose absorbance runs clearly higher than the ones of the others.*

product	Λ_{420} [m]	Λ_{430} [m]	Λ_{440} [m]
Ondina 909 06	9.33 ± 0.84	10.45 ± 0.94	11.40 ± 1.03
Ondina 909 08	8.76 ± 0.79	9.62 ± 0.87	10.29 ± 0.93
Ondina 917 (february)	7.13 ± 0.64	7.70 ± 0.70	8.52 ± 0.77
Ondina 917 (april)	3.07 ± 0.28	3.32 ± 0.30	3.60 ± 0.32

Table 5.5.: *The table lists the attenuation lengths Λ for the mineral oils Ondina 909 and Ondina 917 from the company Shell. Both are types of white mineral oil and mostly differ in their viscosity. While 06 and 08 indicate the year of sampling for Ondina 909, Ondina 917 was produced in 2010 and april and february denote the month they have been received. While Λ of both Ondina 909 and 917 (february) exceeds the required $6\,m$ for the buffer liquid, Λ of Ondina 917 (april) does not. Since both Ondina 917 samples should actually be the same product, this might be traced back to some contamination after the production process.*

buffer mixture	Λ_{420} [m]	Λ_{430} [m]	Λ_{440} [m]
Ondina 909 + tetradecane Petresa	2.69 ± 0.24	3.04 ± 0.27	3.45 ± 0.31
Ondina 917 + n-paraffin Wibarco	11.02 ± 0.99	11.90 ± 1.07	13.13 ± 1.18
Ondina 917 + n-paraffin Helm	7.47 ± 0.67	7.47 ± 0.67	7.61 ± 0.68

Table 5.6.: *The table shows the attenuation lengths at $420\,nm$, $430\,nm$ and $440\,nm$ for different buffer liquids. The buffer liquid with Ondina 917 and n-paraffin from Wibarco as well as from Helm features lengths exceeding the required $6\,m$. The liquid with Ondina 909 and tetradecane from Petresa on the other hand yields lengths under $4\,m$, which are not sufficient.*

5.5.3. Samples from Chooz

LAB from Chooz

Having been produced in Spain the LAB was delivered to Chooz, filtered and pumped in the tanks of the storage area. LAB samples from the truck as well as from the tanks after the filtering process have been taken. The corresponding attenuation lengths are summarized in table (5.7). The LAB from the truck shows lengths of about 5 m to 7 m, which meets the requested 5 m for the MU scintillator, but is not as good as the LAB Helm Spain samples measured in Munich (see subsec. 5.5.1). For the case of a possible contamination during transport (sampling and contact to tanks), LAB just as all the other liquids has been filtered. As can be seen in table (5.7), filtering influenced the transparency leading to a clearly noticeable increase of the attenuation length. After filtering, the LAB shows results similar to the ones of the LAB samples measured in advance.

LAB Chooz from...	Λ_{420} [m]	Λ_{430} [m]	Λ_{440} [m]
...truck	5.08 ± 0.46	5.87 ± 0.53	6.80 ± 0.61
...tank after filtering	7.76 ± 0.70	9.22 ± 0.83	10.55 ± 0.95

Table 5.7.: *The table displays the attenuation lengths at 420 nm, 430 nm and 440 nm of LAB from Chooz. The samples have been taken from the truck directly after delivery and the filtering process. Filtering clearly increased the transparency and consequently the attenuation length. With 9.22 m at 430 nm the filtered LAB has the desired length.*

Mineral Oil from Chooz

Having been transported to Chooz, Ondina samples from the truck as well as from the tanks after unloading and filtering were tested on their attenuation. The resulting attenuation lengths are very good as can be seen in fig. (5.8), exceeding the values measured in advance (compare with subsec. (5.5.2)). Unfortunately, in contrast to the LAB samples, the lengths after filtering are slightly worse. Since filtering should not lower transparency, this is most probably due to a contamination while taking the sample or to negligent handling at the filling process of the spectrometer's cell. Nevertheless, the final mineral oil from Chooz is very transparent.

Ondina Chooz from...	Λ_{420} [m]	Λ_{430} [m]	Λ_{440} [m]
...truck	9.23 ± 0.83	10.12 ± 0.91	11.21 ± 1.01
...tank	8.93 ± 0.80	9.82 ± 0.88	10.90 ± 0.98

Table 5.8.: *The attenuation lengths at 420 nm, 430 nm and 440 nm of the mineral oil from Chooz are shown. Samples have been taken from the truck directly after delivery and from the tank after the filtering process. All lengths exceed the values from the Ondina samples measured in advance in Munich. The lengths after filtering, however, are slightly worse than the ones of the unfiltered oil. This is most probably due to a contamination while taking the sample or to negligent handling at the spectrometer measurements.*

Muon Veto Scintillator from Chooz

After the preparation of the MU scintillator in Chooz, samples have been taken of each of the three MU tanks in the storage area. As the MU liquids have been circulated through all the tanks, each tank, actually, should obtain scintillator with the same properties. Fig. (5.14) gives the resulting absorbance spectra. As can be seen, the run of the curves for the three samples is almost the same. Table (5.9) yields the corresponding attenuation lengths. In each tank they are about the same and meet the required transparency. The final liquid even tends to have higher attenuation lengths than the small samples mixed in advance. One reason for this could be that the single liquids provided by the companies were more transparent. Another reason could be that contamination due to negligent liquid handling during sample preparation on a small scale has a higher effect on the overall transparency than the contaminations that could occur on large scale due to contact with slightly polluted tubes or anything similar. Summarizing one can claim that the MU scintillator in Chooz exhibits the desired attenuation lengths.

MU Chooz	Λ_{420} [m]	Λ_{430} [m]	Λ_{440} [m]
tank 1	5.10 ± 0.46	8.16 ± 0.73	9.94 ± 0.89
tank 2	5.20 ± 0.47	8.39 ± 0.76	10.49 ± 0.94
tank 3	5.33 ± 0.48	8.46 ± 0.76	10.30 ± 0.93

Table 5.9.: *The attenuation lengths of the final MU scintillator from Chooz are shown. A scintillator sample has been taken from each of the three tanks of the storage area. The liquids in the tanks had already been circulated, which is why Λ should be the same for each of the samples. The resulting lengths are very good and even tend to be higher than the ones achieved by the samples mixed in the laboratory in Munich.*
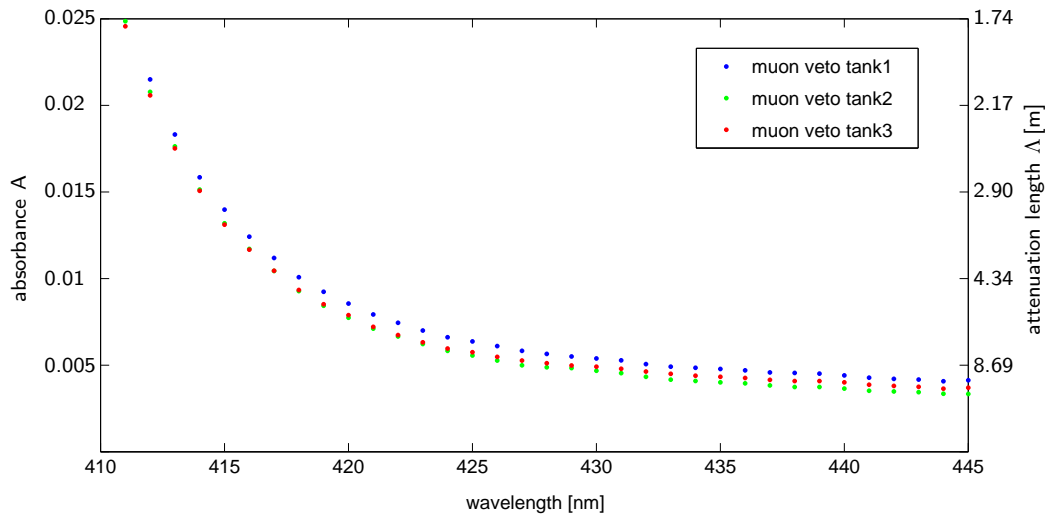
Figure 5.14.: *The absorbance spectra of the final MU scintillator from Chooz are plotted versus wavelength. The right y‑axis gives the corresponding attenuation lengths. A scintillator sample has been taken from each of the three tanks of the storage area. The liquids in the tanks had already been circulated, which is why Λ should be the same for each of the samples. All curves run very close to each other. For every tank the transparency, respectively the resulting Λ is very good and even tends to be higher than the ones achieved by the samples mixed in the laboratory in Munich.*

Buffer Liquid from Chooz

After the preparation of the buffer liquids in Chooz, samples have been taken from the three buffer tanks. Since the liquids in the buffer tanks likewise the liquids in the MU tanks had been circulated, each of the buffer tanks should contain the same liquid. The results of the measurements can be seen in table (5.10). Especially, the attenuation length of the first tank differs from the others. This might be due to some contamination while sampling or during the handling at the spectrometer measurements. Nevertheless, the buffer liquids of all tanks far exceed the required attenuation lengths. Since contamination can always only decrease the attenuation length, the better results, i.e. the ones of tank 2 and tank 3 can be regarded as indicative lengths.

buffer liquid Chooz	Λ_{420} [m]	Λ_{430} [m]	Λ_{440} [m]
tank 1	11.12 ± 1.00	11.98 ± 1.08	13.27 ± 1.19
tank 2	13.93 ± 1.25	15.07 ± 1.36	16.64 ± 1.50
tank 3	13.95 ± 1.26	15.46 ± 1.39	17.00 ± 1.53

Table 5.10.: *From each of the three buffer tanks in the storage area in Chooz a sample has been taken and tested on its transparency. All attenuation lengths are larger than the required 6 m for the buffer liquid. Compared to tank 2 and tank 3, the liquid from tank 1 has lower lengths. Due to the fact that all tanks should contain the same liquid, this might be the result of some contamination during sampling or the sample measurement itself.*
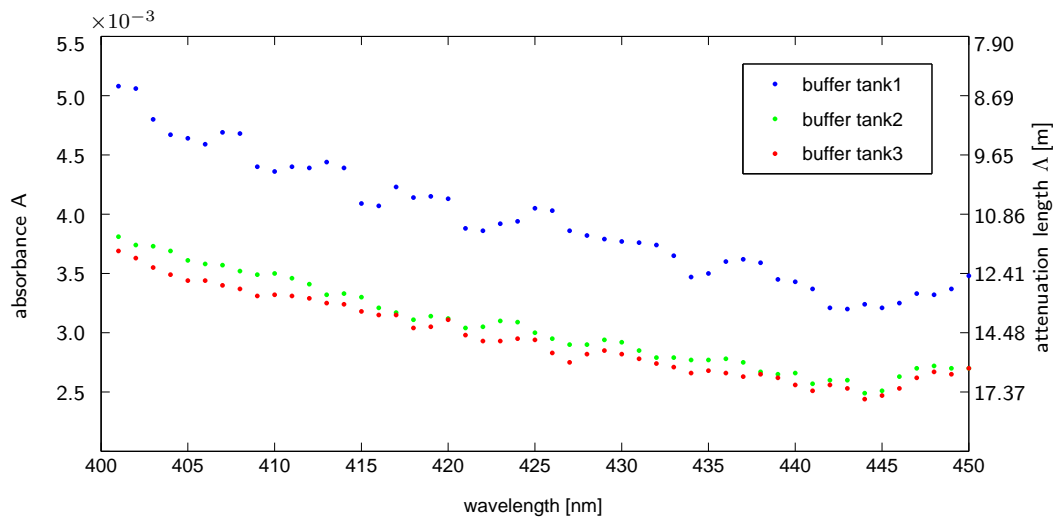
Figure 5.15.: *The absorbance spectra of the buffer liquid from the three tanks of the storage area in Chooz are plotted versus wavelength. The right y - axis gives the corresponding attenuation lengths. The buffer liquid had already been circulated, which is why Λ should be the same for each of the samples. For tank 2 and 3 the curves run close together. The liquid of tank 1 obviously shows a higher absorbance, which must be the result of some contamination during sampling or the measurement. Nevertheless, the transparency of all liquids is very good.*

6. Measurement of the Light Yield due to γ - Irradiation

6.1. Light Yield

Light yield, one of the key parameters of a liquid scintillation detector, characterizes the efficiency regarding to the conversion of deposited energy into detectable photons. Light yield is commonly defined by the ratio of the number of photons N_{ph} produced in the scintillator or in the phototubes of the detector to the energy deposited E_{dep}.

$$LY = \frac{N_{ph}}{E_{dep}} \tag{6.1}$$

In this chapter a measurement of the relative light yield is presented. The best PPO concentration for the Double Chooz muon veto scintillator gaining the highest light yield was determined. The muon veto scintillator then was prepared with the help of *Wacker Chemie* in Munich. The resulting liquids and samples of the final scintillator from Chooz have likewise been checked on their light yield.

6.2. Experimental Setup

For feasibility reasons a relative measurement was performed. A measurement of the absolute light yield is almost impossible without a real 4π- detector geometry. Furthermore, very precise information about the efficiency of the used phototubes would be essential [71]. As a consequence, the determination of the optimal PPO concentration was carried out by comparing the results for different PPO concentrations. Fig. (6.1) gives a schematic overview of the experimental setup. The liquid scintillator stored in a container that will be described later on, indicated by the dark blue cylinder, is excited by γ- rays from a ^{137}Cs $-$ source (orange sphere). The Cs-source has a distance of about $9\,\mathrm{cm}$ to the liquid scintillator cell and an activity of $370\,\mathrm{kBq}$. In the scintillator the γ-quants of the Cs-source perform *Compton scattering* and hence confer part of their energy on electrons. The energy E_{dep} of such a Compton electron under a fixed angle θ can be evaluated via the following formula [36]:

$$E_{dep} = E_\gamma \cdot \left(1 - \frac{1}{1 + \frac{E_\gamma}{m_e \cdot c^2} \cdot (1 - cos\theta)} \right) \qquad (6.2)$$

E_γ thereby is the energy of the initial γ - ray, m_e the electron mass and θ denotes the scattering angle. For a fixed angle one hence gets monoenergetic events. In the used case of a scattering angle of 180° and a γ - ray of 662 keV from the Cs - source the deposited energy is 478 keV. The Compton electrons in return are responsible for the excitation of the molecular states of the fluorescent in the scintillator. The light produced in the liquid scintillator is detected by a PMT connected to the scintillator container ensuring a high light collection efficiency. At this, the glass window of the PMT has the same diameter as the one of the liquid scintillator. A small air gap is left between the two windows to assure the reproducibility of the measurement. The γ - quants scattered backwards are registered by a plastic scintillator (indicated by the light blue cylinder). The distance between plastic scintillator and liquid scintillator cell is about 46 cm. For the measurement, only signals with a coincidence between those two detectors are taken into account. This ensures the signal to be a true event induced by the Cs - source and not a background event caused by cosmic muons.

PMTs are very sensible to light. Therefore, the whole setup has been installed in a black box in order to prevent them from external light and on that account the measurement from disturbance. The black box has a length of about 2 m and a height and width of about 1.10 m each. The experimental setup itself has been installed on a table inside the black box. Lead bricks are used to shield the surroundings from the γ - source. The internal walls of the box have been wainscotted with black felt to guarantee light tightness. The small connector tube at the one side of the box for both the high voltage supply and the signal cables of the PMTs have been light - tightened equally with black felt. Additionally, a black felt has been chosen to cover the whole box.

After the preparation of the samples (see sec. (4.3)) the scintillator cell of the experiment was filled with the first sample. The measuring cell, which can be seen in fig. (6.2), has been made of aluminum, because it is highly reflective. The cell is cylindrical shaped and has a volume of about 20 ml. One side has a quartz glass top, which can be screwed on the cell with an o - ring seal made of teflon. On the other side, there is a little vent with a screw plug and an o - ring seal for filling the cell. Before each filling, the cell was cleaned and dried carefully. In doing so, especially the glass top had to be handled with care. For cleaning the following steps have turned out to be the most effective: Firstly, rinsing out the cell with isopropyl alcohol. Secondly, using distilled water to dissolve and remove the alcohol. Then brushing the cell using warmed water and industrial detergent in order to remove remaining oil films and finally, rinsing it out with distilled water. Due
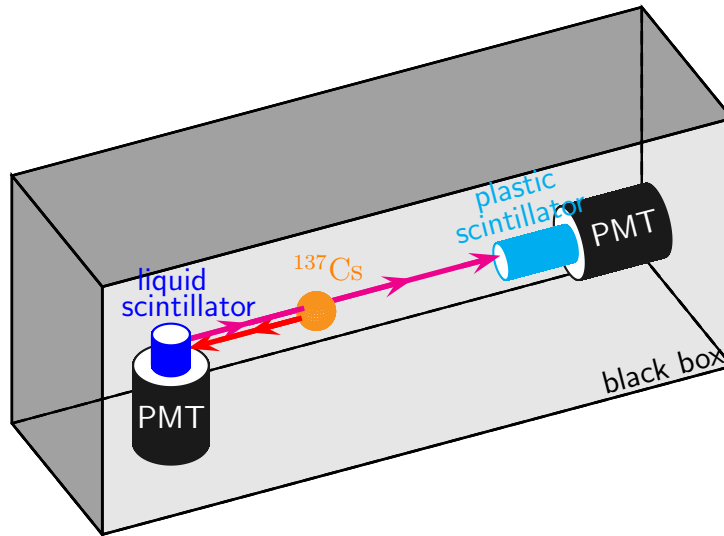
Figure 6.1.: The experimental setup of light yield measurement is illustrated. For details see text.

to the contact with oxygen, corrosion phenomena of the aluminum get noticeable for a long‑term use. In this manner, the reflectivity of cell is diminished, which affects the results of the light yield measurements. For that reason, the aluminum should either be polished regularly or even better, should get anodized. For the latter one should ensure the anodized layer to show the same properties as the original material.

Having screwed the glass top on the cell, it was filled half with the prepared scintillator liquid before being flushed with nitrogen. Finally, the remaining volume was filled with scintillator, too. Being careful that no oxygen remains in the cell, so that the measurement results are not distorted, the cell was closed. The sample then was ready to be placed in the experimental setup. This should be done in darkness to protect the PMTs.

6.3. Read‑out Electronics

For the read‑out electronics a NIM‑based system has been chosen. Fig. (6.3) shows a block diagram of the used electronics. The several electronic devices are summarized in table (6.1). The photomultiplier for the *liquid scintillator* is operated at a voltage of ‑ 810 V, whereas the one for the *plastic scintillator* is operated at a voltage of ‑ 800 V. First of all, the signals of both PMTs are amplified. Afterwards, they are split by a *Fan In/Fan Out* in order to guide them to both the *transient recorder* (explained later on) and to the *discriminators* for further evaluation. The

Figure 6.2.: *The photo depicts the scintillator container that was used for the light yield measurements. It has been made of aluminum due to its high reflectance.*

signals are discriminated at a threshold of 200 mV for the liquid and at a threshold of 60 mV for the plastic scintillator. The logical signals of both discriminators are passed on to a *And Gatter*. The pulse of the PMT of the liquid scintillator is additionally delayed by 16 ns. This is due to the fact that the detector response of the plastic scintillator is significantly slower than the one of a liquid scintillator and to adjust differences in cable lengths. When an event is registered in the liquid scintillator and shortly after within a time range of 20 ns also in the plastic scintillator, the And Gatter triggers both channels in order to record them with a 10 bit transient recorder.

A scaler is used to monitor the coincidence rate and the rates of both PMTs. With the settings described above the plastic scintillator showed a stable rate of about 77 Hz. The rate of the liquid scintillator and therefore the rate of the coincidences, depend on the scintillator under investigation. With a mean rate of about 425 Hz for the different liquid scintillators used, the rate of coincidence was about 0.029 Hz. As the time window for a coincidence was 20 ns, random coincidences can be estimated less than 2% of all events recorded. For this reason, random coincidences are negligible. Correlated background, on the other hand, can originate from gammas that might undergo multiple scattering off the surroundings, for example, the lead sheets.

The PMTs used are models of the company *ETL/ETEL* of the type *9111B*. They are equipped with blue - green sensitive bialcali photocathodes with plano - concave
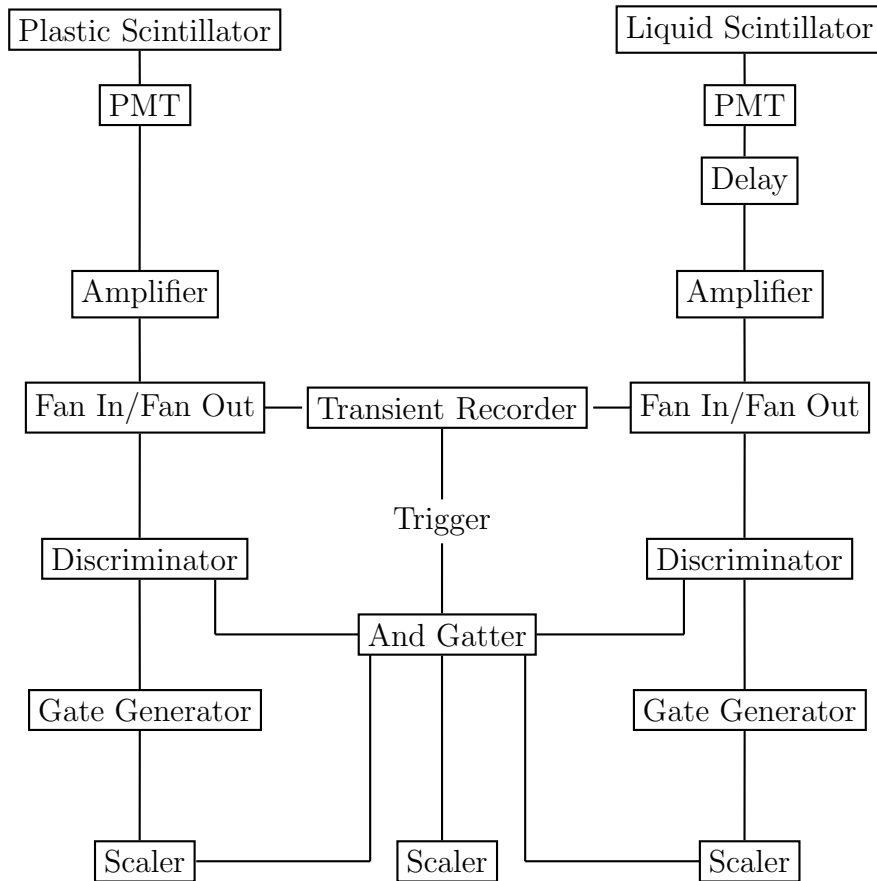
Figure 6.3.: *The block diagram shows the electronics used for the light yield measurement.*

Element	Model
Amplifier	CAEN Mod. N979
Fan In/Fan Out	CAEN Mod. N625
Attenuator	Le Croy Mod. A101
Discriminator	CAEN Mod. N840
Gate Generator	MPI Dual Gate Pulse Generator
And Gatter	CAEN Quad Coincidence Logic Unit Mod. N455
Scaler	CAEN Quad Scaler + Preset Counter Timer Mod. N1145
Transient Recorder	Gage CS82G

Table 6.1.: *The table lists the several electronic devices used for the light yield measurement.*

window and a diameter of 25 mm designed for fast timing. In order to reduce the influence of external electromagnetic fields, the PMTs are shielded by a protective μ - metal. The technical specifications of the above - named PMTs are listed in table (6.2). *PMT 1* refers to the liquid scintillator and *PMT 2* to the plastic scintillator.

	PMT 1	PMT 2
Type	Electron Tubes 9111B	Electron Tubes 9111B
Serial number	20918	20934
Dark current	20 Hz	1000 Hz
Peak-to-Valley	1.3	no single photon
Window	borosilicate	borosilicate

Table 6.2.: *Technical specifications of photomultipliers used for light yield measurement [72].*

For the last measurements PMT 1 had to be exchanged. The new photomultiplier was of the same model 9111B of the company ETEL. Due to the fact that each PMT, even if of the same type, features different characteristics attributable to the manufacturing process, the settings for the high voltage as well as for the discrimination thresholds had to be adapted. Therefore, of course, also the rate of the resulting events generated in the liquid scintillator and, consequently, the coincidence rate did change. Using the scaler, the random coincidence rate could again be justified to be negligible. The changed discrimination threshold, however, did not affect the results of the measurements as they are relative ones comparing different samples to a reference. The absolute light yield had been determined by remeasuring the reference sample of known absolute light yield in the new setup.

6.4. Analysis

The signals were read out using an analogous data analysis program called *Gage scope*. For every measurement 3600 counts were recorded, in order to reduce the statistical error to an acceptable size. The acquired events were read out with a program written in C++. The pulse heights of the detected coincidences were binned into a histogram. A typical energy spectrum generated by a liquid scintillator can be seen in fig. (6.4). For the analysis of the spectra a fit was implemented. Considering that the background decreases exponentially in energy, whereas the pulse height spectrum of detected coincidences shows a Gaussian distribution, the following fit function has been used:

$$N = p2 \cdot \exp\left(-\frac{1}{2} \cdot \left(\frac{x - p3}{p4}\right)^2\right) + \exp(p0 + p1 \cdot x) \tag{6.3}$$

Here N indicates the number of events per channel, x is the channel number proportional to the energy and $p0$ to $p4$ are arbitrary fit parameters. The position of the maximum, $p3$, is proportional to the light yield and thus gives a measure of it. The absolute light yield was calculated using

$$LY_{sample} = \frac{LY_{ref}}{p3_{ref}} \cdot p3_{sample} \tag{6.4}$$

6.5. Error Estimation

The channel with the maximum was determined by the fitting program. The statistical error for the position of this channel is given by the fit. Due to the high statistics, this error can be evaluated to be only about 0.4% and therefore is negligible. The error of the light yield measurement is clearly dominated by the systematical error. As sources for the latter, the mixing of the scintillator samples, the cleaning process and the filling of the cell, as well as the mounting of the cell in the experimental setup have to be mentioned. Imperfection in mixing, especially, for small samples, can lead to uncertainty in the composition of the scintillator, which can affect the scintillation characteristics. In the case of an insufficient cleaning, oil streaks can remain on the quartz glass, which influence transparency. Additionally, inclusion of air in the sample volume, which can appear due to negligent filling of the cell, can also result in changes of the scintillation characteristics. Little variations in the mounting position of the cell, for example, caused by turning the cell, might lead to uncertainty. In order to install the cell in exactly the same position
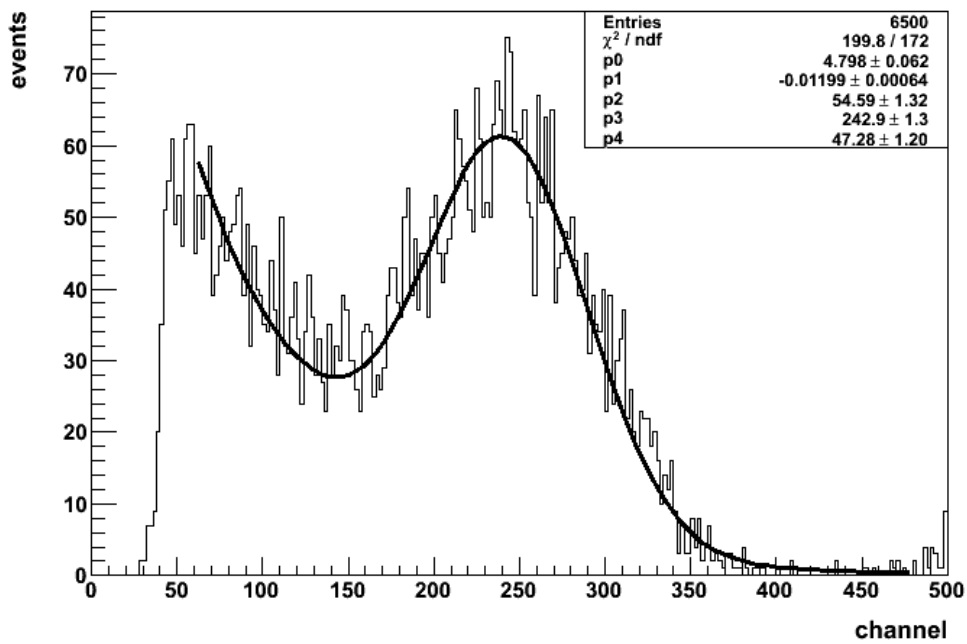
Figure 6.4.: *The picture shows an energy spectrum of a typical coincidence measurement. The applied fit considers both the exponentially decreasing background and the Gaussian peak from the energy deposition of the gammas in the liquid scintillator. While N indicates the number of events per channel, x is the channel number proportional to energy and p0 to p4 are arbitrary fit parameters.*

for the next measurement and in this manner guarantee reproducibility, a mark at the cell can be used. For an estimation of the systematical uncertainty and to investigate the reproducibility, measurements of one defined liquid scintillator concentration were repeated. Thereby, the whole sample preparation and filling procedure was carried out again. This way, the uncertainty has been assigned to be about 4 %. Since the absolute light yield of the used reference sample is given with an accuracy of 10 % [73], the total systematical error has been estimated to be 11 % by quadratic error propagation.

6.6. Results

For determining the optimal PPO concentration of the MU scintillator, samples were prepared in a composition of 37.5 % vol. LAB P - 550Q, 62.5 % vol. tetradecane[1], 20 mg/l bisMSB and PPO, whose fraction was varied from 1 g/l to 4 g/l in steps of 0.5 g/l. The other components thereby were kept fixed at their particular concentrations. The determination of the absolute light yield is very difficult as it is strongly dependent on the respective experimental setup. For this reason, the light yield of a sample of known absolute light yield was measured in the same experimental setup. The comparison with this sample allows the determination of the absolute light yield for any other sample measured in this setup. As reference sample, the Borexino liquid scintillator [2] with an absolute light yield of 11 ± 1 ph/keV [23, 73] was used.

The diagram in fig. (6.5) depicts the relative light yield depending on the PPO concentration. The x - axis shows the PPO concentration in g/l. The y - axis gives the absolute light yield in photons per energy in keV. As it can be seen, the graph begins with a slope that later on for a PPO concentration of about 1.5 g/l saturates. Based on this diagram, the decision on the PPO concentration has been made in favor of 2 g/l PPO. For this concentration the light yield is no longer in the steep region of the curve. A higher PPO concentration, on the other hand, would not significantly improve it. The considered concentration therefore is high enough to achieve the favored light yield and at the same time is the least necessary one. A higher PPO concentration, of course, would also imply higher costs. In addition, too high concentrations of the wavelength shifters offer the risk of self - absorption.

The results for the absolute light yield are summarized in table (6.3). "tetradecane + LAB + bisMSB" thereby indicates the fixed components in their particular concentration, namely 62.5 % vol. tetradecane, 37.5 % vol. LAB and 20 mg/l bisMSB.

---

[1]Due to the measurements of the attenuation length (see sec. (5.5)), LAB P - 550Q has later on been replaced by LAB Helm Spain and tetradecane by n - paraffin CBR. Due to slightly different densities, the percentages of the liquids changed to 48.4 % vol. LAB, 51.6 % vol. n - paraffin.

[2]Pseudocumene (PC) with 1.5 g/l PPO [23]
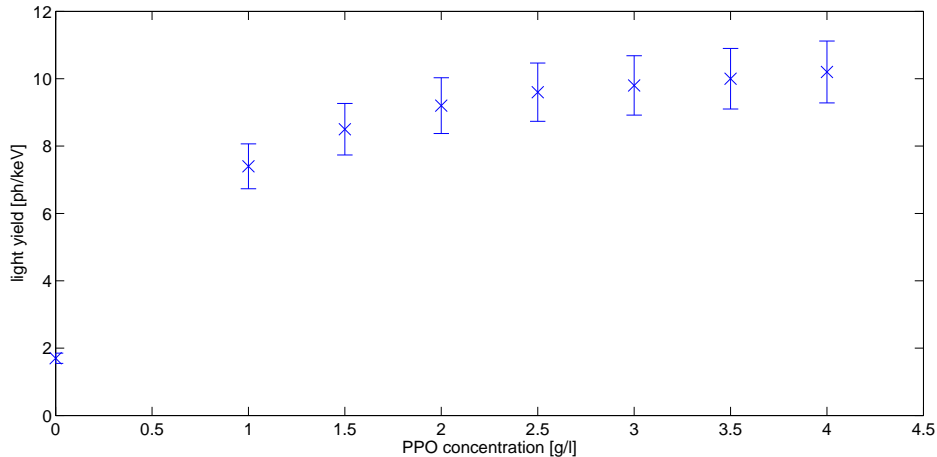
Figure 6.5.: *The diagram gives the absolute light yield of the muon veto scintillator depending on the concentration of PPO. The light yield curve starts with a slope that for higher PPO concentrations shows saturation. Based on this diagram it has been decided to use a PPO concentration of 2 g/l PPO. For this concentration the light yield is no longer in the steep region of the curve. A higher PPO concentration, on the other hand, would not significantly improve it. Too high concentrations of the fluors offer the risk of self-absorption and imply higher costs. The considered concentration hence is not only high enough to achieve the favored light yield, but also the least necessary one.*

scintillator sample	absolute light yield [ph/keV]
LAB + tetradecane + bisMSB + 0 g/l PPO	1.7 ± 0.2
LAB + tetradecane + bisMSB + 1.0 g/l PPO	7.4 ± 0.8
LAB + tetradecane + bisMSB + 1.5 g/l PPO	8.5 ± 0.9
LAB + tetradecane + bisMSB + 2.0 g/l PPO	9.2 ± 1.0
LAB + tetradecane + bisMSB + 2.5 g/l PPO	9.6 ± 1.1
LAB + tetradecane + bisMSB + 3.0 g/l PPO	9.8 ± 1.1
LAB + tetradecane + bisMSB + 3.5 g/l PPO	10.0 ± 1.1
LAB + tetradecane + bisMSB + 4.0 g/l PPO	10.2 ± 1.2

Table 6.3.: *The table lists the absolute light yield that has been determined for the muon veto scintillator, namely 62.5 % vol. tetradecane, 37.5 % vol. LAB and 20 mg/l bisMSB with varying PPO concentration. The absolute light yield increases with increasing PPO concentration. The decision has been made for 2 g/l PPO resulting in a light yield of 9.2 photons/keV.*

Table (6.4) gives an overview of the absolute light yield of different scintillator samples as well as of n‑paraffins and the mineral oil Ondina that also have been tested for scintillation. MU in this case stands for the final composition of the DC MU scintillator, which is to say 48.4 % vol. LAB, 51.6 % vol. n‑paraffin, 2 g/l PPO and 20 mg/l bisMSB. Helm Belgium and Helm Spain indicate the company of the LAB used for the MU scintillator, either from the company Helm in Belgium or from the same company in Spain. MU from Master Solution means that the Master Solution has been diluted to the final muon veto scintillator concentration in the laboratory in Munich, whereas MU Chooz are samples of the ready muon veto scintillator from Chooz.

Neither the n‑paraffins nor the Ondina did show any scintillation. Together with other requirements, such as high transparency and radiopurity, this makes them suitable candidates for the buffer liquid.

The absolute light yield of the mixture of LAB and tetradecane both of the company Petresa in the final MU composition with 2 g/l PPO but without any bisMSB turned out to be 7.4 ph/keV (see table (6.4)). This is less than the light yield of 9.2 ph/keV of a sample with the same components, but with bisMSB added (see table (6.3)) and demonstrates the influence of bisMSB as a second wavelength shifter. Within the ranges of uncertainty the light yield of this MU scintillator made of Petresa products (see table (6.3)) could also be achieved by the MU Helm Belgium and MU Helm Spain (see table (6.4)). The MS with (9.6 ± 1.1) ph/keV, of course, shows a higher light yield, since it only contains the fluorescent LAB and the highly concentrated wavelength shifters.[3] Having been diluted, the light yield of the MS (MU from MS) with (8.4 ± 0.9) ph/keV, is in the range of the MU scintillator samples previously prepared in the laboratory.

The absolute light yield of the ready MU scintillator from Chooz has been determined to be (9.0 ± 1.0) ph/keV. The desired light yield of the MU scintillator thus has been achieved.

---

[3]The MS contains PPO in a concentration of 40 g/l and bisMSB in a concentration of 0.4 g/l.

scintillator sample	absolute light yield [ph/keV]
n-paraffin CBR	no scintillation
n-paraffin Helm	no scintillation
n-paraffin Wibarco	no scintillation
Ondina	no scintillation
LAB + tetradecane + 2.0 g/l PPO	7.4 ± 0.8
MU with LAB Helm Belgium	7.8 ± 0.9
MU with LAB Helm Spain	8.7 ± 1.0
Master Solution	9.6 ± 1.1
MU from Master Solution	8.4 ± 0.9
MU Chooz	9.0 ± 1.0

Table 6.4.: *The table gives the absolute light yield that has been determined for different samples. Neither the n-paraffins nor the Ondina did show any scintillation, which is a requirement concerning the buffer liquid. The mixture LAB + tetradecane + 2.0 g/l PPO does not contain bisMSB. Its light yield is less than the light yield of a muon veto scintillator that additionally contains the bisMSB as a second wavelength shifter. The MU scintillator samples with LAB Helm Belgium and Spain show light yield in the same order of magnitude, which could also be achieved by the MU scintillator obtained from the Master Solution and the final scintillator from Chooz.*

7. Measurement of the Light Yield due to Neutron Irradiation

Organic liquid scintillators mainly contain protons. The principal interaction of neutrons incident on the scintillator is elastic neutron‑proton scattering. The recoiled protons are responsible for the ionization of the scintillator molecules and hence the light output. In order to analyze the light yield of the DC muon veto scintillator with respect to neutrons, it was the aim to determine the proton‑quenching factor (see also sec. (4.1.3)).

7.1. Proton‑Quenching Factor

By definition, the *quenching factor (QF)* is the ratio of the recoil energy E_R which is the totally deposited energy in the scintillator and the fluorescence energy L [1].

$$QF = \frac{E_R}{L} \tag{7.1}$$

As described in sec. (4.1.2) and sec. (4.1.3) quenching, the reduction of the fluorescence intensity of a scintillator, is related to the ionization density, which is considered in the formula of Birks. The QF is a function of the energy and the mass of the primary recoiling nucleus as well as of the scintillator's chemical composition and its temperature [47].

7.2. Kinematics of Neutron Elastic Scattering

For organic liquid scintillators, which mainly contain protons, the effect of quenching does occur for neutrons that undergo elastic neutron‑proton scattering. The scattered proton in the scintillator leads to ionization and as a consequence luminescence light will be emitted by the scintillator. In the following, elastic neutron‑proton scattering, which is the principal interaction for neutrons with an energy of

---

[1] The light yield L of nuclear recoils is usually expressed in terms of a so‑called *electron‑equivalent energy* E_{ee}, i.e. the energy of a recoiled electron that results in the same light output as the nuclear recoil in the detector (compare with (6.1)).

less than 1 GeV [36], will be discussed. At energies of several MeV, the problem may be treated nonrelativistically.

Fig. (7.1) illustrates a single collision in the laboratory frame between a nucleus of mass M and a neutron with velocity v_n. The nucleus is assumed to be at rest [36]. The angle between the direction of the incoming neutron and the recoiled nucleus is denoted by θ_{lab}. Considering conservation of energy and momentum yields

$$
\begin{aligned}
E_n &= E_A + E_{n,s} \\
\Rightarrow \frac{\vec{p}_n^2}{2m} &= \frac{\vec{p}_A^2}{2mA} + \frac{\vec{p}_{n,s}^2}{2m}
\end{aligned}
\tag{7.2}
$$

and

$$
\vec{p}_{n,s} = \vec{p}_n - \vec{p}_A
\tag{7.3}
$$

with E_n the energy of the incoming neutron with momentum $\vec{p}_n$ and $E_{n,s}$ the energy of the scattered neutron with momentum $\vec{p}_{n,s}$. E_A denotes the energy of the recoiled nucleus and $\vec{p}_A$ the corresponding momentum. The mass of the neutron is indicated by m and the mass number of the nucleus by A. Furthermore, the following approximation for the mass M(A) of a nucleus with mass number A has been used

$$
M(A) = m \cdot A.
\tag{7.4}
$$

Equation (7.3) squared results in

$$
\vec{p}_{n,s}^2 = \vec{p}_n^2 - 2\,|\vec{p}_n|\,|\vec{p}_A|\cos(\theta_{lab}) + \vec{p}_A^2
\tag{7.5}
$$

which applied to equation (7.2) gives the recoil energy of the nucleus:

$$
E_A = \frac{4A}{(A+1)^2} \cdot E_n \cdot \cos^2(\theta_{lab}).
\tag{7.6}
$$

In the particular case of elastic neutron-proton scattering (A=1), it simplifies to

$$
E_p = E_n \cdot \cos^2(\theta_{lab}),
\tag{7.7}
$$
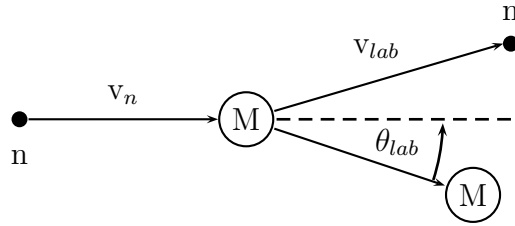
Figure 7.1.: *Scheme of elastic scattering in the laboratory frame. A neutron of velocity v_n indicated by n scatters on a nucleus of mass M at rest. v_{lab} is the velocity of the neutron after the scattering and θ_{lab} denotes the angle between the direction of the incoming neutron and the recoiled nucleus.*

where E_p is the recoil energy of the proton.

In order to determine the energy distribution of the scattered neutrons, one can make use of the fact that at neutron energies of less than about 15 MeV, isotropic s-wave scattering is a good approximation to describe the neutron scattering [36]. As derived in [36], the probability of an originally monoenergetic neutron to have the energy $E_{n,s}$ after the scattering process is

$$\frac{dw}{dE_{n,s}} = \frac{(A+1)^2}{4A} \cdot \frac{1}{E_n} = const. \tag{7.8}$$

which simplifies to

$$\frac{dw}{E_{n,s}} = \frac{1}{E_n} = const. \tag{7.9}$$

in the case of neutron-proton scattering. The energy distribution of the scattered neutron after a single scattering process hence is constant. Due to

$$\frac{dw}{E_p} = \frac{dw}{dE_{n,s}} \cdot \frac{dE_{n,s}}{dE_p} = \frac{1}{E_n} \cdot (-1) = const. \tag{7.10}$$

this also refers to the energy distribution of the recoil proton. This result will be used in sec. (7.5.5).

7.3. Experimental Setup

7.3.1. The MLL Accelerator

For the determination of the proton-quenching factor of the Double Chooz muon veto scintillator, the accelerator of the *Maier Leibnitz Laboratorium* (MLL) in Garching served as a neutron source.
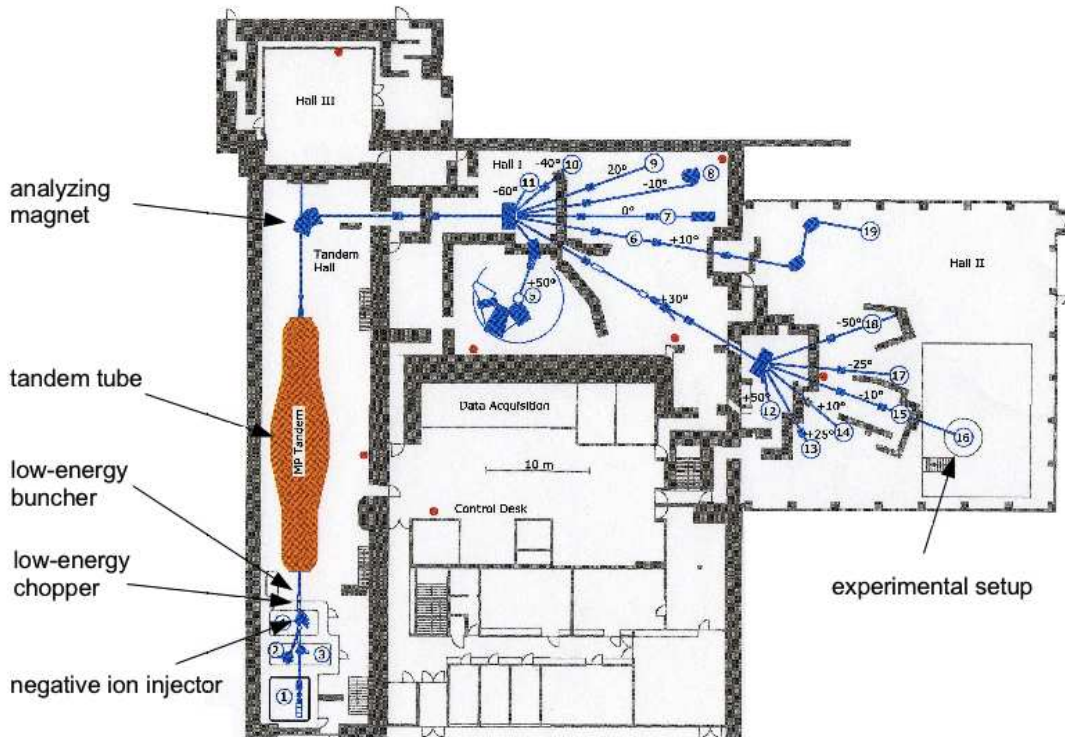
Figure 7.2.: *Top view of the MLL accelerator facility in Garching [74]. The several devices denoted in the picture are explained in the text.*

The tandem accelerator is an advancement of a Van-de-Graaff accelerator. It can reach high ion energies by using the acceleration voltage (up to 15 MeV) twice. Accelerated by a potential difference, negatively charged ions are being stripped of their electrons by a stripping foil inside the tube of the tandem accelerator. The change of polarity allows to accelerate them again by the same potential difference [74].

Fig. (7.2) shows a top view of the accelerator facility. For the first step of acceleration the tandem accelerator requires negatively charged ions, which are produced by the *negative ion injector*. For the production of neutrons ^{11}B ($E_{kin} \sim 61.5$ MeV) has been chosen. The boron ions are pre-accelerated by the extraction voltage (~ 10 kV), before they are injected into the *tandem accelerator tube*. The ions

produced usually consist of different charge numbers and thus of miscellaneous energies. To produce a monoenergetic beam, a 90° *analyzing magnet* is used to select the desired energy and isotope. The adapted beam can then be focused into the beamline in order to be guided to the experimental setup.

The time‑of‑flight measurements used for the investigation of the quenching factor need a sharply pulsed beam (width 2‑4 ns) which is achieved by the so‑called *low‑energy buncher* and the *low‑energy chopper*. The low-energy buncher periodically compresses the continuous beam into units (pulse width ~ 20 ns). The low‑energy chopper cuts off the parts between the beam bunches in order to further sharpen them. A logical pulse from the pulsing devices is used as a start signal for the time‑of‑flight measurements [74].

7.3.2. Neutron Production

At the end of the beamline neutrons are produced inside a so‑called *hydrogen cell* (see fig. (7.3)). The cell's inner diameter is about 1 cm and its length is 3 cm. Charged with 2 bar of hydrogen, neutrons in the MeV regime are generated via the nucleus reaction $p(^{11}B,n)^{11}C$. A 5 μm thick molybdenum foil separates the cell from the vacuum in the beamline. This foil can stand the pressure difference of 3 bar and allows the high energetic ^{11}B‑beam to pass with an average energy loss of about 5 MeV. A ^{11}B‑beam of an energy of 55.4 MeV is found to be the optimal value, leading to a resonant production of 11 MeV neutrons in forward direction [74].
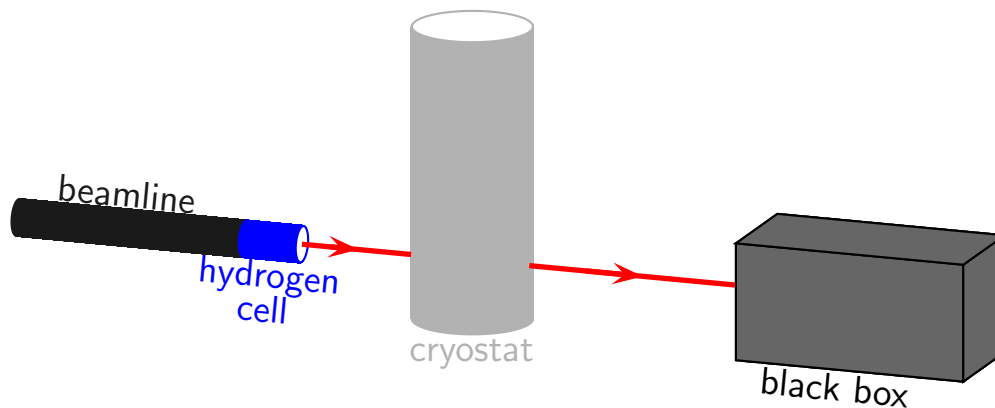
Figure 7.3.: *The picture illustrates the side view of the experimental setup for the measurement of the QF at the MLL. The DC scintillator has been installed in a black box located in the beamline of the accelerator behind the cryostat of the CRESST scattering experiment. Also shown is the hydrogen cell for the production of the neutrons.*

7.3.3. Scintillator Setup

The measurement of the proton‑quenching factor was carried out in the context of the *CRESST* scattering experiment [74, 75], which uses a cryogenic detector installed in the beamline of the accelerator. Placed in Hall II of the MLL (see fig. (7.2) on page 78), this scattering setup allows unique experiments to measure quenching factors of scintillating crystals at mK temperatures.

For the proton‑quenching factor measurement of the DC muon veto scintillator, a scintillator sample coupled to a PMT was installed at this facility (see fig. (7.3) and fig. (7.4)). The scintillator was a sample of the final liquid from Chooz. The cell has a volume of 20 ml and is made of aluminum to ensure a high rate of light reflection. To minimize background (parasitic scattering of neutrons), the walls of the cell have been made as thin as possible (see fig. (6.2) on page 66).
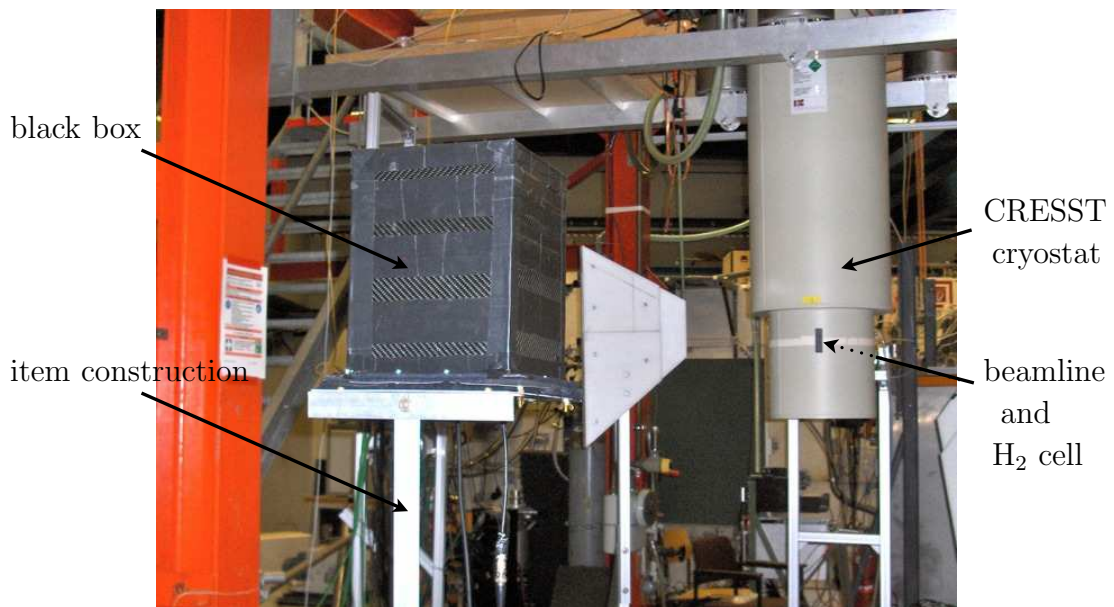
Figure 7.4.: The photo shows the experimental setup for the light yield measurement due to neutron irradiation of the DC muon veto scintillator. A scintillator sample was installed in the beamline of the MLL accelerator in Garching at the CRESST scattering facility. The PMT and the scintillator cell are covered by a light tight housing (black box) made of carbon. The box is mounted on a rack constructed of the aluminum profile system *item* [76] and is located behind the CRESST cryostat at 0°.

The PMT and the sample are covered by a light tight housing (black box) (see fig (7.4)). In order to reduce background due to additional scattering of neutrons, all components of the setup are built as light as possible. The black box with height

of 28 cm and a square basis with an edge length of 20 cm is made of carbon fiber. Cracks between the single carbon fiber sheets are additionally masked with scotch tape. The PMT is hold by an aluminum clamp and the whole box is mounted on a rack constructed of the variable aluminum profile system *item* [76]. The box is located at 0°, at a distance of 3.65 m to the hydrogen cell. Shorter distances have not been possible due to experimental constraints of the CRESST scattering experiment.

7.4. Setup of Data Acquisition

The pulse parameters of the *PMT* signals are recorded by an *analog‐to‐digital converter (ADC)* and all timing information is registered by a *time‐to‐digital converter (TDC)*. The signals of the PMT are amplified and fed in the ADC and a *constant‐fraction discriminator (CFD)*. The CFD triggers on a certain fraction of the pulse height which makes the trigger time independent. The output of the CFD is directly connected to the TDC which continuously records the event times of the PMT and the starting information provided by the pulsing devices.

The ADC, CFD and TDC modules are part of a VME‐based system that was chosen and developed in [75]. The *VME bus* connects the *VME controller* to a *standard PC* by an optical‐fiber cable. The events of the detector during the measurement campaigns are recorded and the analysis is performed offline. Coincidences between the bunches of the accelerator and events in the photomultiplier are determined.
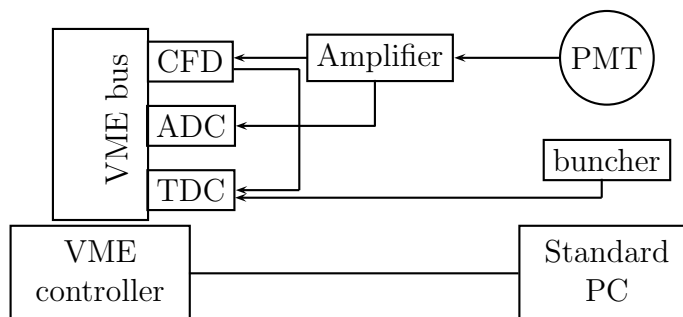
Figure 7.5.: *Wiring scheme of the VME‐based modules and the photomultiplier.*

Element	Model
PMT	ETL/ETEL type 9111B
Amplifier	CAEN Mod. N979
Constant Fraction Discriminator	CEAN v812
Time to Digital Converter	CAEN v1190
Analog to Digital Converter	Struck Sis3320
VME controller	CAEN v2718

Table 7.1.: *The several electronic devices used for the proton‑quenching measurement are listed.*

7.5. Analysis

7.5.1. Time‑of‑Flight Plot

In fig. (7.6) a typical time‑of‑flight (ToF) plot is shown. The y‑axis of this scatter plot gives the scintillation energy measured with the PMT in arbitrary units. The x‑axis gives the time of flight Δt in ns with the zero value provided by the pulsing devices as described in sec. (7.3.1). The first distribution found at a Δt of about 300 thereby is the so‑called γ-distribution. Together with the neutrons, a large amount of gammas is produced in the hydrogen cell, which also reach the liquid scintillator. Depositing their energy, they lead to luminescence light that can be detected with the photomultiplier. As the gammas have travelled the distance x of 3.65 m from the cell to the PMT with velocity of light c, the γ‑distribution corresponds to a time of $t = \frac{x}{c}$. This information is used to calibrate the x‑axis.

The second distribution in fig. (7.6) at a Δt of about 369, originates from the fastest neutrons that reach the detector. They are due to the resonant neutron production of about 11 MeV in the hydrogen cell (see (7.3.2)). At later flight times neutrons with lower energies arrive in the detector causing the decreasing shaded area behind the prominent neutron peak. The calibration of the x‑axis (fig. (7.10)) yields a ToF of $t = 81$ ns for the fastest neutrons. According to that, the maximum energy of the neutrons in the beam can be derived using

$$E_n = \frac{1}{2} \cdot m\, v_n^2 = \frac{1}{2} \cdot m \left(\frac{x}{t} \right)^2 \qquad (7.11)$$

where m is the neutron mass, v_n its velocity, x the travelled distance and t the time‑of‑flight. This results in a maximum neutron energy of 10.6 MeV.
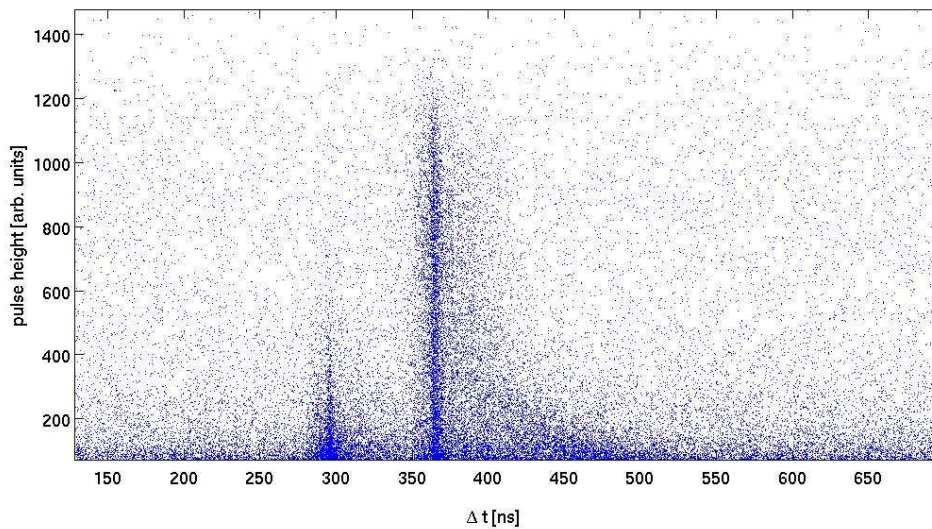
Figure 7.6.: *The figure shows a typical ToF scatter plot of the DC muon veto scintillator under irradiation of neutrons measured during a beamtime at the MLL. While the x-axis gives the time difference Δt between the starting signal for the ToF-measurements given by the pulsing devices and the PMT signal in ns, the y-axis gives the pulse heights measured with the PMT. The left distribution is due to the gammas that are produced together with the neutrons in the hydrogen cell. The right distribution originates from the neutrons.*

source	process of γ production	branching	$T_{1/2}$ [y]	E_γ [keV]	E_{CE} [keV]
^{137}Cs	β^-	85 %	30	662	478
^{22}Na	β^-/EC	100 %	2.6	1275	1062

Table 7.2.: *For the calibration of the ToF measurement a ^{137}Cs-source and a ^{22}Na-source have been used. The sources together with the respective process of gamma production, branching, their gamma energy E_γ and the energy of the Compton edge E_{CE} are shown [77].*

7.5.2. Energy Calibration

The constituents of organic scintillators feature low Z - values which is why no photo peaks are visible to realize energy calibration. Therefore, the energy calibration of the experiment was carried out by the use of different γ - sources (see table (7.2)). The emitted γ - rays undergo *Compton scattering* in the liquid scintillator and transfer part of their energy to the so - called *Compton electron* whose energy is given by

$$E(\theta, E_\gamma) = E_\gamma - \frac{E_\gamma}{1 + \frac{E_\gamma}{m_e c^2}(1 - \cos\theta)} \tag{7.12}$$

where E_γ is the energy of the incident gamma ray, m_e the electron mass and θ the scattering angle [36].
The maximum energy deposition E_{max} is achieved by backward scattering at an angle of $\theta = 180°$. By plotting the counts in the PMT versus the energy measured with the scintillator, this becomes visible as an edge in the spectrum that generally is referred to as *Compton edge* and can serve as a calibration point. For the calibration of the energy axis the following procedure has been applied: The spectrum with counts plotted versus the pulse height in arbitrary units, which has been measured in the scintillator, has been fitted with a Gaussian fit function in the high energy region (see fig. (7.7) and fig. (7.8)). For the energy of the Compton edge E_{CE}, the point x_{CE}, which is the pulse height channel at which the spectrum has decreased to half of its maximum towards higher pulse heights, has been chosen [42]. The calibration can be obtained by a linear fit to the calibration points ($x_{CE,i}$, $E_{CE,i}$) where i refers to the different γ - sources. The fluorescence energy L hence is given by

$$L = \frac{E_{CE,i}}{x_{CE,i}} \cdot x = c \cdot x \tag{7.13}$$

where x is the pulse height channel.
The resulting plot leading to the calibration factor c can be seen in fig. (7.9). It is in good agreement with the assumption of a linear detector response. Fig. (7.10) shows the energy measured in the liquid scintillator plotted versus the time - of - flight after calibration of the axes.
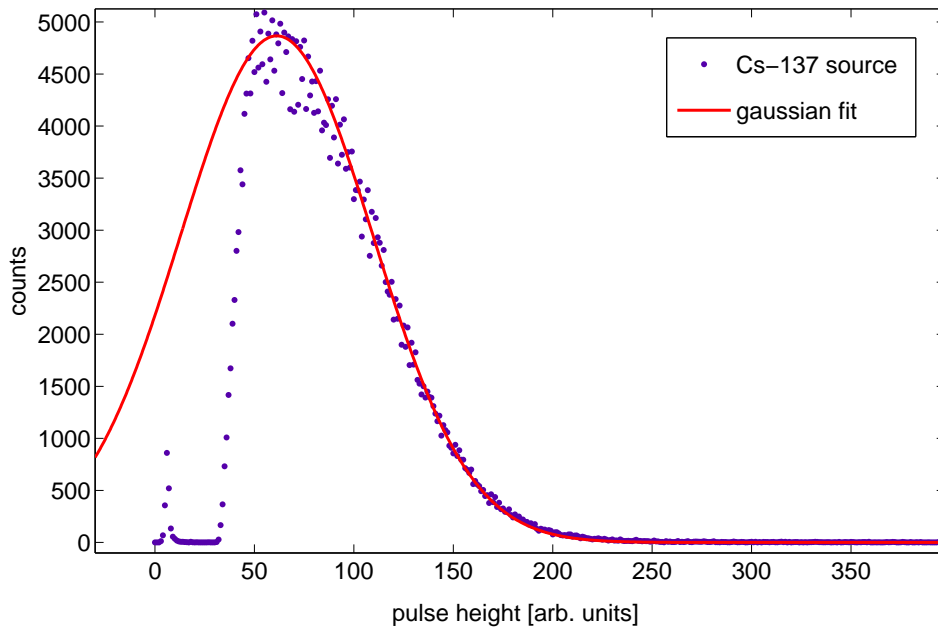
Figure 7.7.: *Pulse height spectrum of the DC muon veto scintillator under irradiation of a ^{137}Cs - source. The Compton edge has been fitted using a Gaussian fit function.*
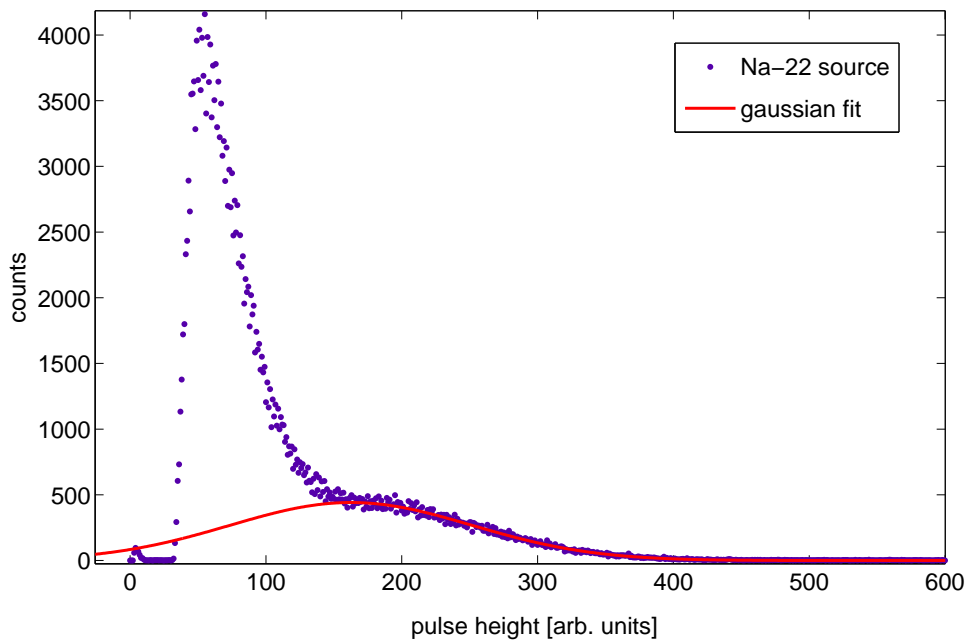
Figure 7.8.: *Pulse height spectrum of the DC muon veto scintillator under irradiation of a ^{22}Na - source. The Compton edge has been fitted using a Gaussian fit function.*
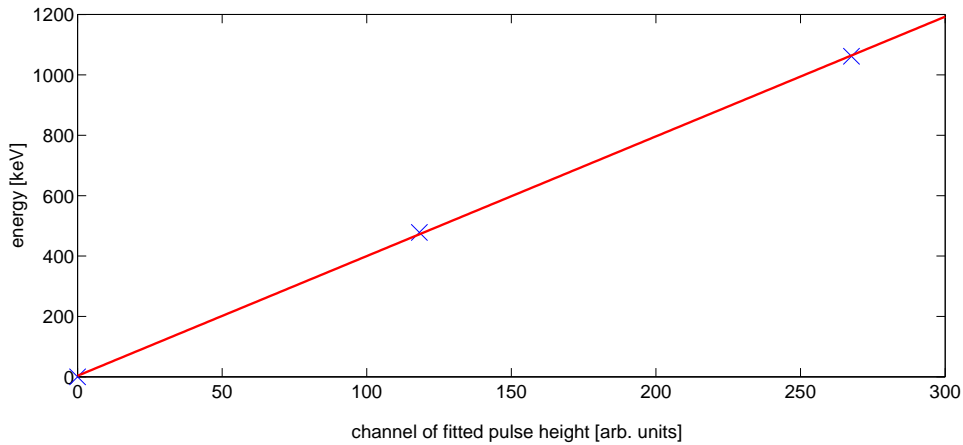
Figure 7.9.: *The calibration points for the DC muon veto scintillator from a ^{137}Cs - source and a ^{22}Na - source have been fitted with a linear function.*
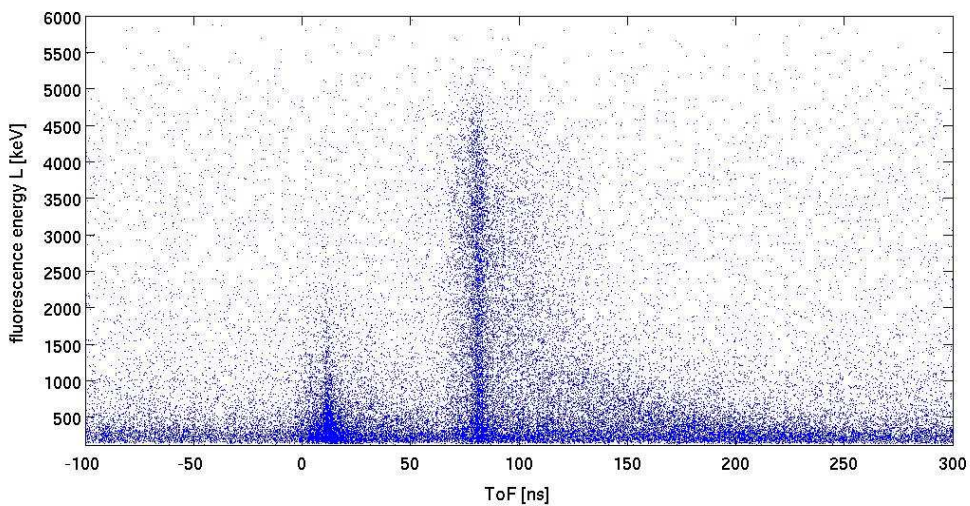
Figure 7.10.: *The plot shows the time - of - flight spectrum of the DC muon veto scintillator under irradiation of neutrons after the calibration of the axes. The left distribution belongs to the gammas that are produced together with the neutrons in the hydrogen cell. The right distribution originates from the neutrons.*

7.5.3. Neutron-γ Discrimination

As described in sec. (4.1.1), the light emission of organic scintillators is dominated by a single fast component, but also features a substantial slow component. Both contributions depend on the energy deposition per unit path length dE/dx. For heavier and slower particles, for example, this deposition in the scintillator material is large compared to the one of fast electrons. This results in a higher ionization for heavier particles and consequently a higher fraction of delayed fluorescence. Scintillators, where this impact on decay time and hence pulse shape is strong, are capable of *pulse-shape discrimination*, i.e. capable of distinguishing between different types of incident particles by the shape of the emitted light pulse [36]. For such a scintillator, fig. (7.11) qualitatively shows the pulses of alpha particles, fast neutrons (proton recoils) and gamma rays for comparison.
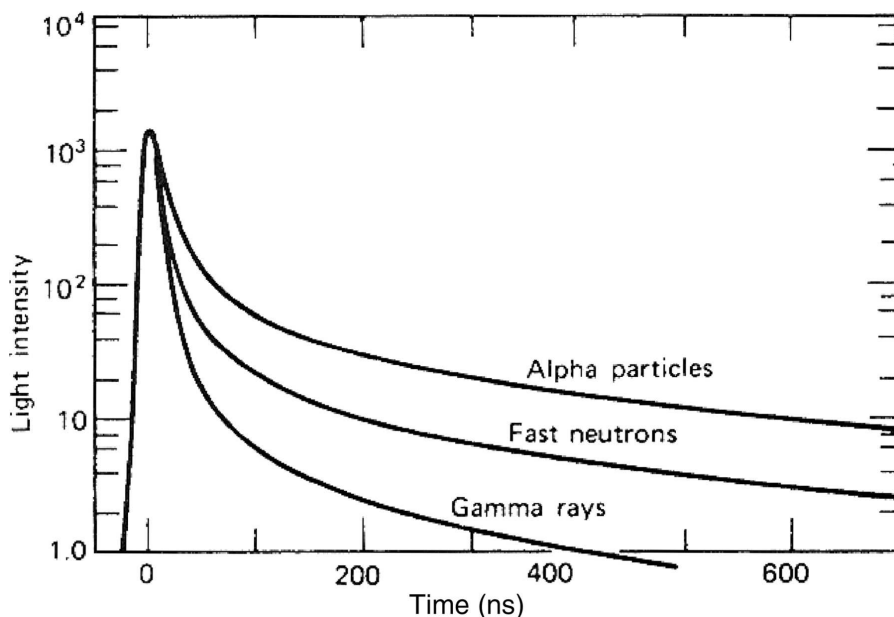
Figure 7.11.: *The time dependence of scintillation pulses in a typical liquid scintillator due to the excitation by alpha particles, fast neutrons and gamma rays is illustrated qualitatively. Scintillators, where the overall decay time of the emitted light pulse varies with the type of incident particle can be used for pulse-shape discrimination [42].*

The muon veto scintillator has been checked on its neutron-γ discrimination capability. For the discrimination, a scintillation pulse can be integrated over different time intervals. In order to distinguish between neutrons and gammas it is sufficient to apply two integration gates, a short one ($\sim 50\,\text{ns}$) and long one ($\sim 500\,\text{ns}$) [74, 75]. With the help of the acquisition software (see (7.4)) that has a graphical interface to display pulses of the detector during the measurement, integration gates for the pulse-shape discrimination can be applied. They can be optimized checking the neutron-γ discrimination in a live discrimination plot. Fig. (7.12) shows the discrimination parameters for a set of pulses containing neutrons and gammas in a scatter plot. The ratio of the integrated pulse signals of the short and the long integration gate is plotted versus the long gate. A ToF-cut has been applied to the 10.6 MeV neutron-distribution as well as to the γ-distribution. The neutrons are indicated by the red color, whereas blue dots represent the gammas. Fig. (7.13) shows the ratio of the integrated pulse signals of the short and the long integration gate binned in a histogram, where again only the events from the γ-cut (indicated by blue color) and the 10.6 MeV neutron-cut (indicated by red color) are shown.
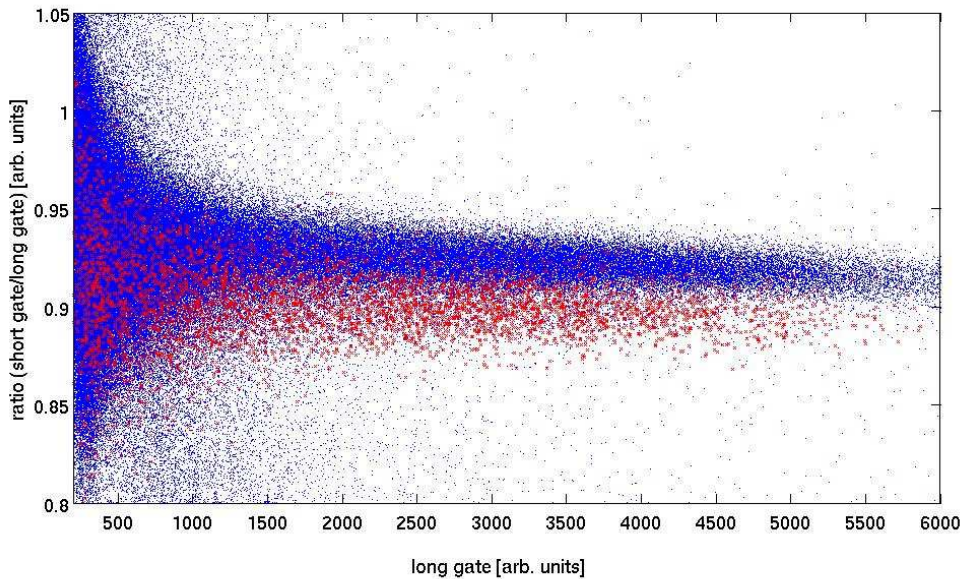
Figure 7.12.: *The ratio of the integrated pulse signals of the short and the long integration gate is plotted versus the long gate, which is a measure for the deposited energy. The upper population (blue dots) represents gamma events, whereas the lower band (red dots) originates from neutron-induced protons.*
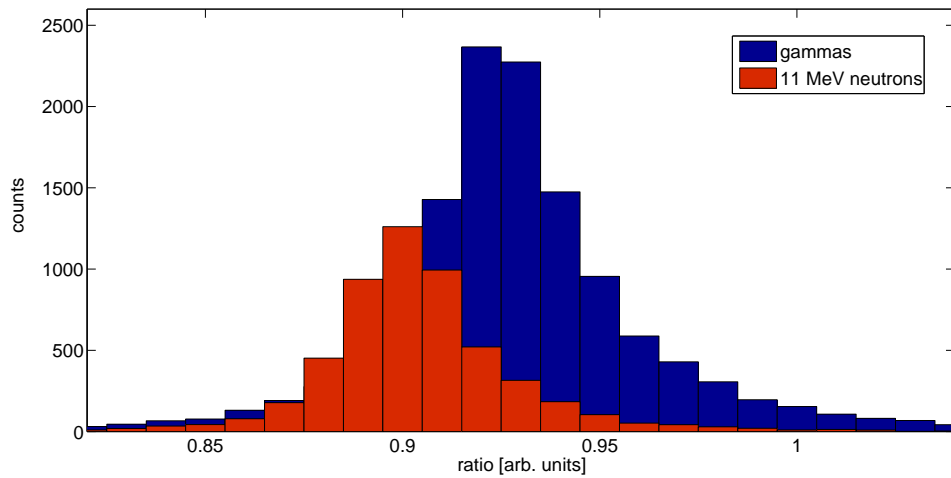
Figure 7.13.: *The ratio of the integrated pulse signals of the short and the long integration gate has been binned into a histogram. Here, only events from the γ - distribution (indicated by blue color) and the 10.6 MeV neutrons (indicated by red color) have been taken into account.*
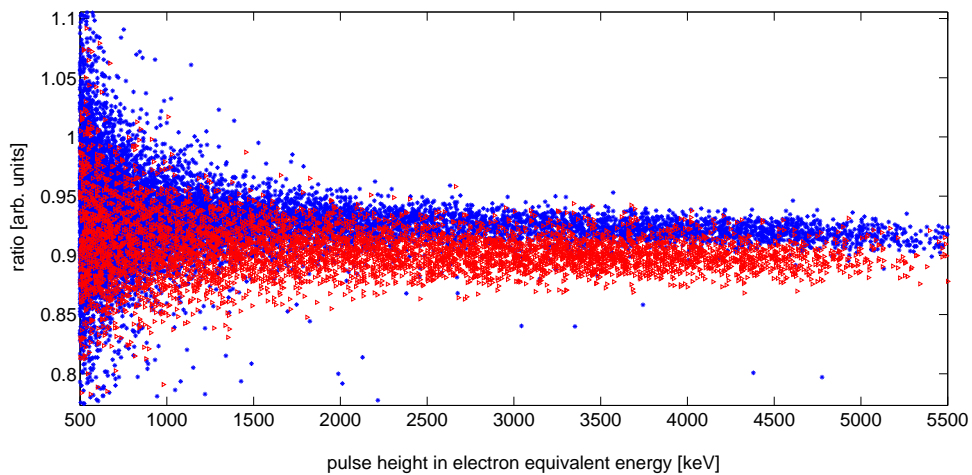
Figure 7.14.: *The ratio of the integrated pulse signals of the short and the long integration gate is plotted versus the pulse height in electron - equivalent energy measured in the detector.*

In order to examine whether electron and proton recoil events can be distinguished, the following steps have been taken.

- The ratio of the short versus the long integration gate has been plotted versus the pulse height in electron-equivalent energy measured in the detector (see fig. (7.14)).

- All events from $1\,\mathrm{MeV}$ to $5\,\mathrm{MeV}$ were binned with a $250\,\mathrm{keV}$ binning.

- To each gamma- and neutron-distribution of each energy bin, a gaussian fit was applied. Fig. (7.15) exemplarily shows the fitted gaussian distributions for one of those bins. The discrimination capability is quantified by the extent of the overlap of both distributions.

A $1\,\sigma$-discrimination is possible, if those distributions do not overlap on a $1\,\sigma$-level. In fig. (7.16) the mean values of the gaussian fits are plotted versus the energy. The blue line denotes the gammas and the red line the $10.6\,\mathrm{MeV}$ neutrons. The dashed lines have been obtained by adding and subtracting, for each energy cut, the corresponding $1\,\sigma$ to and from the mean values of the gamma and neutron distributions, respectively. The dashed lines therefore indicate an error band of $1\,\sigma$-width around the averages demonstrating to what energy neutron and gamma events can be distinguished on a $1\,\sigma$-level. Above an energy of about $2180\,\mathrm{keV}$ the error bands do not overlap, which means that on a $1\,\sigma$-level, neutron-γ discrimination is possible above an energy threshold of $2180\,\mathrm{keV}$ in electron equivalent energy.
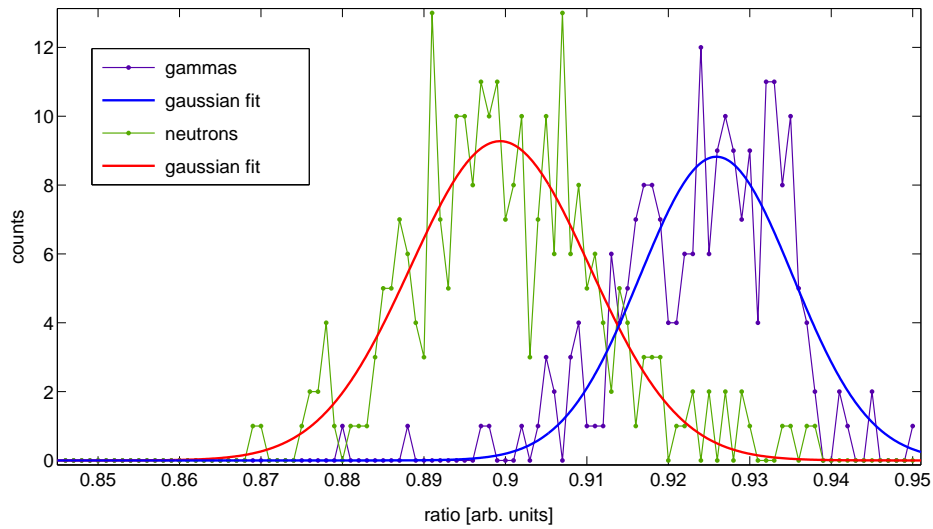
Figure 7.15.: *Cuts on the energy measured in the detector have been applied. Binned in a histogram of the ratio, these events show two distributions due to the electron and proton recoils as can be seen exemplarily in this figure. Each distribution has been fitted with a gaussian fit function. Neutrons are indicated by green dots and the red fit and the gammas by purple dots and the blue fit, respectively.*
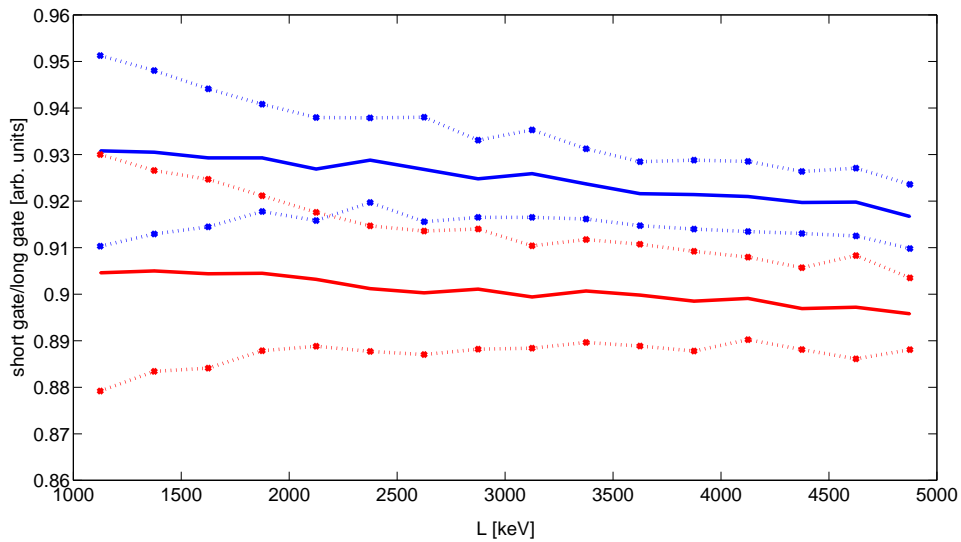
Figure 7.16.: *The mean values of the ratio of event rates in the short and long integration gate of the neutron - (red color) and γ - distribution (blue color) are plotted versus the fluorescence energy L in the detector. Also shown are the 1σ - lines above and below the mean values illustrating the discrimination capability on a 1σ - level.*

7.5.4. Proton - Quenching - Factor at 10.6 MeV

According to eq. (7.1) on page 75, two informations are of importance for the evaluation of the proton-quenching factor: the light yield of the scintillator L and the recoil energy E_R. While L corresponds to the scintillation energy that can directly be measured with a PMT, E_R refers to the energy E_p that has been transferred to the recoil proton. Depending on the scattering angle this energy varies (see sec. (7.2)). Knowing the incident neutron energy via ToF measurement, the highest visible scintillation light output L_{max} induced by neutrons must belong to elastically backscattered neutrons (angle of 180°), transferring all their energy (E_n) on the proton. Using eq. (7.1) the quenching factor thus becomes:

$$QF = \frac{E_R}{L} = \frac{E_n}{L_{max}} = \frac{\frac{1}{2}m(\frac{x}{t})^2}{L_{max}} \tag{7.14}$$

Thus the quenching factor at an energy of about 10.6 MeV can be determined using the prominent 10.6 MeV neutron peak. Therefore, the first step is to assign the maximal scintillation energy L_{max}, for which the following procedure has been used: A cut of 10 ns has been applied to the neutron peak from 76.2 ns to 86.2 ns in fig. (7.10). Having done so, 4658 events remained. Subsequently, the events fulfilling the ToF condition have been binned in a histogram of the scintillation energy and the statistical background known from measurements without neutron beam has been subtracted. Having subtracted the background, 4188 events remained. In order to determine the maximum energy, a Gaussian fit has been applied to the high energy region as can be seen in fig. (7.17). As maximum energy, the value, where the spectrum has decreased to half of its maximum, has been chosen [42]. Fig. (7.18) shows the point that has been determined that way together with the scatterplot.

The proton - quenching factor for an energy of 10.6 MeV has been evaluated to be $2.6 \pm 16\,\%$ (for the error estimation see sec. (7.5.6)).
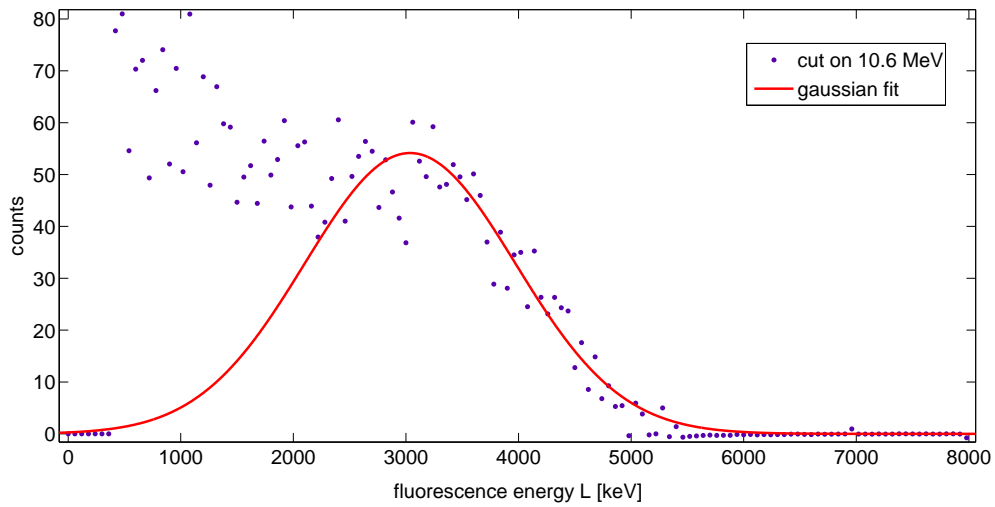
Figure 7.17.: *The events of the cut on the prominent neutron peak ($\sim 10.6\,MeV$) have been binned in a histogram and a gaussian fit has been applied in order to determine the maximum energy.*
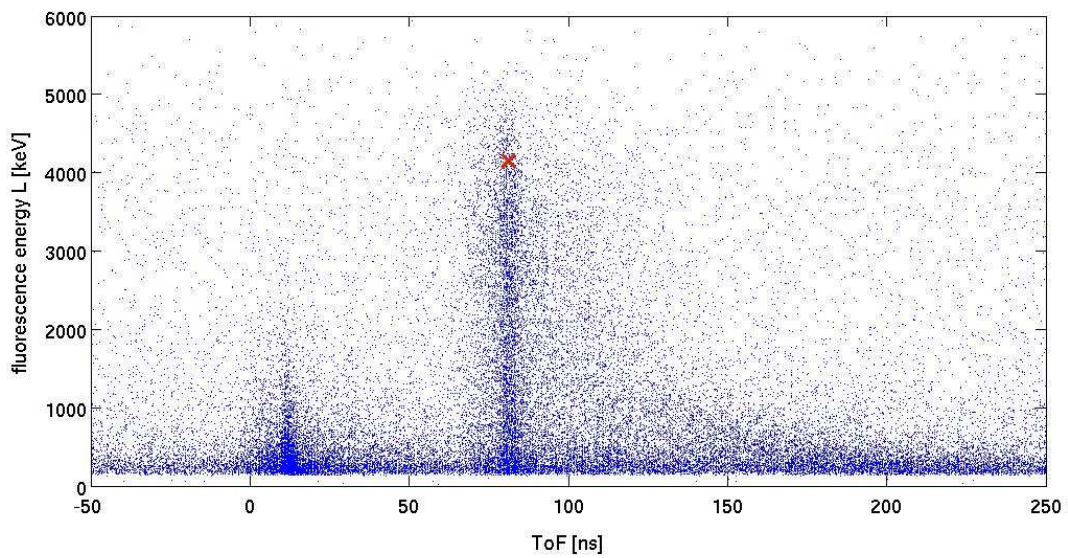
Figure 7.18.: *The time-of-flight scatter plot is shown together with the maximum scintillation energy (indicated by the red cross) that has been determined for the 10.6 MeV neutrons.*

7.5.5. Quenching-Factor Dependence on the Recoil Energy

The quenching factor, actually, is not a constant, but dependent on the recoil energy [42]. In order to assign the quenching factor for lower energies, the first attempt was to apply further cuts on subsequent lower energies (increasing time of flight) of the incoming neutrons and to proceed just as in the manner of the 10.6 MeV cut. Quenching factors determined for lower energies by using this method, however, show a clear trend towards too low values for increasing time of flight. There are several reasons, why this method is only applicable to the highest energetic neutrons:

- Above all, an electronic problem, which has not been resolved yet, did occur during the beamtime. Once adjusted the settings for the buncher and the chopper (see 7.3.1), that are responsible for the timing properties of the pulsed beam, did not stay constant over time. As a result typical beam structures were influenced in so far as neutron production was less confined in time. Although this does not affect the described proton-quenching factor determination for the highest energetic neutrons, it does for higher times of flight since a broadening smears out the decreasing time-of-flight spectrum towards lower energies. A correct determination of the highest fluorescence energy at higher times of flight therefore was not possible.

- The same effect may occur due to a background of neutrons, that have scattered off the large mass surrounding the scintillation detector and thus been delayed in time. That way, intrinsically higher energetic neutrons additionally contribute to longer times of flight. The scattering might mainly be off the cryostat, in detail the Helium dewar (aluminum) and parts of the cryostat around the detector module (mainly copper and steel), which the neutron beam passes before reaching the scintillator cell, but also off the scintillator setup itself.

- The prominent peak of the neutron energy spectrum is at about 10.6 MeV originating from the resonant production of neutrons in the hydrogen cell (see 7.3.2). Due to the distribution of the neutrons, however, the statistics get worse for different energies making it difficult to determine the maximal fluorescence energy.

For the reasons listed above, only the cut on the highest energetic incoming neutrons is confidable. Fig. (7.17) on page 93 shows the corresponding pulse height distribution. In order to examine the energy dependence of the quenching factor on the proton energy $QF(E_p)$, the shape of this spectrum was reconstructed using

a Monte Carlo method.

Neglecting additional contributions from competing reactions at high energies and multiple scattering effects (for the discussion see sec. (7.5.6)), the shape of the pulse height spectrum can be described by a function

$$f(L) = const. \cdot \int \left(g(E_p, L) \otimes QF(E_p) \cdot \frac{dw}{dE_p} \right) dE_p. \tag{7.15}$$

The distribution hence can be obtained by integrating over the quenching factor $QF(E_p)$ (see sec. (4.1.3) and (7.1)), the cross section of the elastic neutron-proton scattering that is proportional to the energy distribution of the recoil proton dw/dE_p and the gaussian energy resolution $g(E_p, L)$ of the detector in the limits of possible proton energies. With dw/dE_p being constant (see sec. (7.2)), $f(L)$ becomes

$$f(L) = const \cdot \int \left(g(E_p, L) \otimes QF(E_p) \right) dE_p \tag{7.16}$$

Using eq. (7.16) the spectrum has been simulated. The recoil proton energy thereby has been randomly chosen between zero and the maximum energy of the incoming neutron (10.6 MeV). The energy resolution of the detector has been assumed proportional to $\sqrt{E_p}$ according to

$$\sigma(E_p) = \sigma_0 \cdot \sqrt{E_p} \tag{7.17}$$

with σ_0 being a proportional constant. From the gaussian fit in fig. (7.17) that describes the maximal energy transfer of the 10.6 MeV neutrons on the proton, the proportional constant σ_0 has been determined to be 0.22.

For a first approach this has been done for an energy independent QF. As a value 2.6 was assumed, as it is the value obtained for the 10.6 MeV protons. The resulting plot can be seen in fig. (7.19).

Supposing an ideal detector resolution, a linear light output of the scintillator and a constant energy distribution of the recoil protons, the expected pulse height distribution should be rectangular with a steep cutoff. Just as in the case of the measured spectrum, the simulated distribution varies from the distinct rectangular structure at the highest recoil energies, where it is washed out due to the detector resolution. The curve of the measured data, however, features an additional rise for lower scintillation energies. This slope should not be due to background since the background has been considered and subtracted by applying the 10.6 MeV cut
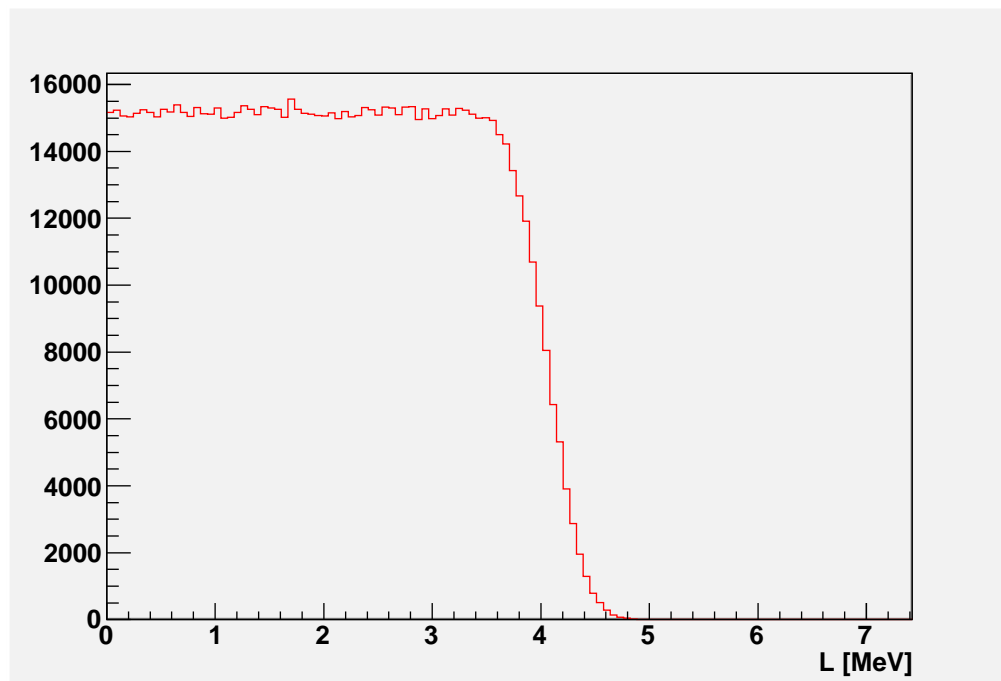
Figure 7.19.: *The pulse height distribution for the 10.6 MeV neutrons has been simulated. The quenching factor has been assumed to be constant. Compared to the experimentally measured data the graph misses the rise for lower energies. As discussed in the text this can mainly be traced back to the influence of the energy dependence of the quenching factor.*

(see sec. (7.5.4)). Even if there was some background left, it should be negligible and the rise less marked. The increase of events for low energies thus can mainly be traced back to the influence of the energy dependence of the QF.

In the next step the behavior of the QF with the energy was estimated. As discussed in sec. (4.1.3) the light output per unit path length dL/dx of a liquid scintillator is given by the formula of Birks [35]:

$$\frac{dL}{dx} = \frac{S\frac{dE}{dx}}{1 + kB\frac{dE}{dx}} \tag{7.18}$$

where kB is the Birks factor, S the absolute scintillation efficiency and dE/dx the energy deposition per unit path length of the ionizing particle. dE/dx is given by the Bethe‐Bloch formula [42]:

$$-\frac{dE}{dx} = \frac{4\pi e^4 z^2}{m_0 v^2} \cdot NZ \left(\ln \frac{2m_0 v^2}{I} - \ln \left(1 - \frac{v^2}{c^2} \right) - \frac{v^2}{c^2} \right) \tag{7.19}$$

where v and ze are the velocity and the charge of the primary particle, N and Z are the number density and the proton number of the absorber atoms, m_0 is the electron rest mass, e the electronic charge and I denotes the average ionization potential of the absorber.

With 10.6 MeV at maximum the neutrons for the proton‐quenching experiment and thus also the recoiled protons can be treated nonrelativistically. For nonrelativistic charged particles ($v \ll c$), however, the terms within the parentheses can be neglected. Thus the specific energy loss of a recoiled proton is proportional to $1/v^2$ or varies inversely with particle energy according to

$$-\frac{dE}{dx} \sim \frac{1}{v^2} \Rightarrow -\frac{dE}{dx} = \frac{a}{E_p} \tag{7.20}$$

with a being a constant and E_p the energy of the proton. As discussed in sec. (4.1.3), dE/dx becomes large for an ion which is the reason why in that case the 1 in the denominator can be neglected and the specific light output approximately is

$$\left. \frac{dL}{dx} \right|_{ion} = \frac{S}{kB} \tag{7.21}$$

where S and kB are depending on the scintillation medium. In a rough approximation this also applies to a proton as will be illustrated by the example of the

E_p [MeV]	9	8	7	6	5
$QF(E_p)$	2.7 ± 0.1	3.0 ± 0.1	3.4 ± 0.1	4.0 ± 0.2	4.8 ± 0.2

Table 7.3.: *Based on the energy dependence that was derived from a Monte Carlo simulation, the quenching factor was calculated for different energies within the range of the measured data.*

borexino scintillator [23] whose kB factor is known:
The energy deposition per unit path length of a 1 GeV proton in hydrogen is 4.5 MeVcm^2/g [78]. With the density of the borexino scintillator of $\rho = 0.8$ g/cm^3 this becomes $\sim$ 4 MeV/cm energy deposition per unit path length. Using eq. (7.20) the energy deposition for protons of about 10 MeV hence can be derived to 400 MeV/cm. The kB factor for the borexino scintillator is 0.02 cm/MeV [79] leading to $kB \cdot (dE/dx)_{10\,MeV} \approx 8 > 1$. As a result dL/dx approximately tends to a constant.

Using eq. (7.21) integration hence results in the absolute light yield due to a recoiled proton:

$$L = \int_0^{x_m} \frac{dL}{dx}\, dx = \int_{E_p}^0 \frac{dL}{dx}\frac{dx}{dE}\, dE \overset{(7.20)}{=} -\int_{E_p}^0 \frac{S}{kB}\frac{E}{a}\, dE = k \cdot E_p^2 \qquad (7.22)$$

Here, x_m is the range of the proton, E_p its energy and k a constant.
Using its definition (see eq.(7.1)) the quenching factor becomes

$$QF = \frac{E_p}{L} = \frac{k}{E_p}. \qquad (7.23)$$

with k being a constant. The best result has been obtained with $k = (24 \pm 1)$ MeV. The simulated distribution can be seen in fig. (7.20). Using eq. (7.23) and $k = 24$ MeV the quenching factor has been calculated for different energies within the energy range of the measured data. The results together with the errors due to the uncertainty in k are listed in table (7.3).
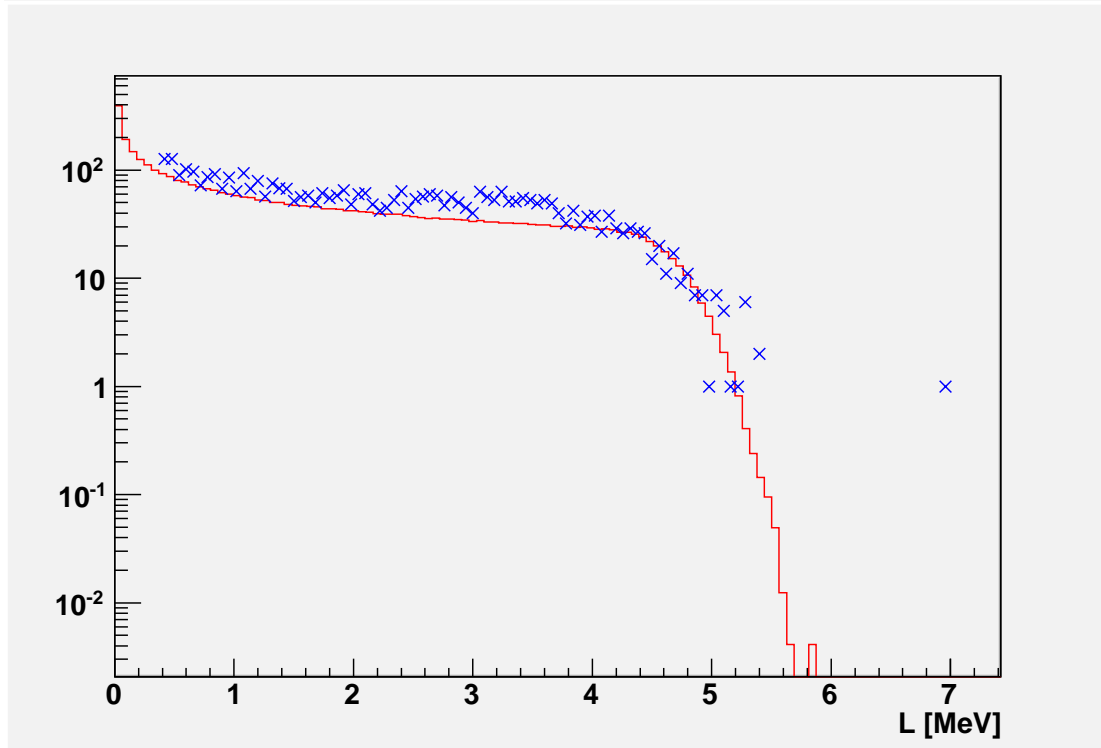
Figure 7.20.: *The pulse height distribution for the 10.6 MeV neutrons has been sim-
ulated (indicated by red color). Also shown is the measured spectrum
(indicated by blue color). For the simulation the quenching factor has
been assumed to be $QF = \frac{k}{E_p}$ with E_p being the proton energy and the
constant k being 24 MeV. Compared to the plot obtained by a constant
QF (see fig. (7.19)) of 2.6, the curve increases for lower energies and
gives a quite good fit to the experimental data.*

7.5.6. Error Estimation and Discussion of the Results

Error Estimation of the Proton‑Quenching Factor

For the estimation of uncertainty for the proton quenching factor at 10.6 MeV, the following errors have been taken into account:

- A systematical error in the resolution for the time of flight measurement that can be estimated to be about $\Delta t = 4$ ns.

- A systematical error in the distance x due to the distance from hydrogen cell to the scintillator cell that had been measured and the size of the scintillator cell. This uncertainty can be assumed to be about 1 cm.

- A statistical error of about 15 % in the maximal scintillation energy L_{max} due to the fit on the energy spectrum used for its determination.

Linear error propagation of the total systematical and the total statistical error resulted in a total error of about 16 %. The proton‑quenching at an energy of 10.6 MeV hence is 2.6 ± 0.4.

Discussion of the Simulated Energy Dependence

The simulated distribution (fig. (7.20)) obtained with the energy dependent QF approximately describes the run of the experimental data. In comparison to the plot obtained by a constant QF (see fig. (7.19)), its curve increases for lower energies. Nevertheless, the simulated spectrum still deviates from the measured data. For one reason, this can be explained by the approximations made at the derivation of the energy dependence of the QF, more precisely, in the Birks and Bethe‑Bloch formula. Furthermore, the following effects result in a further distortion of the pulse height spectrum, but have not been considered in the simulation:

- *Edge effect*: If the range of the recoil protons is not small compared with the detector dimensions, effects due to escaping protons from the scintillator medium can occur [42]. Those effects might be applicable to the setup of the measurement since the volume of the scintillator, with only about 20 ml, is sufficiently small and, additionally, the neutron energy with about 11 MeV quite high. Escaping protons are not able to deposit their whole energy, which means they still create events, but shifted to lower energies. That way, these events distort the pulse height spectrum by causing a further increasing slope in the region of lower pulse heights.

- *Competing reactions at high energies*: For neutron energies higher than 8 or 9 MeV two competing reactions contribute to the overall response of organic scintillators [42]: $^{12}C(n, \alpha)^{9}Be$ at an energy threshold of 6.17 MeV and

^{12}C(n, n')3α at an energy threshold of 7.98 MeV. Both reactions become significant above 9 MeV and in this range lead to an increase in the pulse height distribution.

In general, the shape of the pulse height distribution could additionally be influenced by neutrons that undergo multiple scattering off hydrogen or scattering off carbon followed by scattering off hydrogen [42].[2] For the scintillator setup used, however, the contribution of multiple scattering can be neglected since the detector volume with only 20 ml is too small.

At an energy of 10.6 MeV the quenching factor was determined from the pulse height distribution. With 2.6 $\pm$ 0.4 this quenching factor agrees with the quenching factor of 2.3 $\pm$ 0.4 obtained by the simulation at the respective energy. This result is also in the range of the proton-quenching factor that has been assumed for the KamLAND scintillator [80].

---

[2]The neutron elastic scattering from carbon itself does not contribute much to the detector output, as according to Birks (see (4.1.3)) the scintillation efficiency for particles with a high energy deposition per unit path length is low.

8. Conclusion and Outlook

The discussion of possible neutrino oscillations started with the discovery of the solar neutrino discrepancy problem in 1968 [5]. Since that time neutrino oscillations have been confirmed by several experiments. The underlying oscillation theory has six independent parameters, namely three mixing angles $\vartheta_{12}, \vartheta_{23}$ and ϑ_{13} as well as two mass-squared differences Δm_{21}^2 and Δm_{32}^2 and a CP-violating phase δ. With $\Delta m_{21}^2 = (7.59_{-0.21}^{+0.19}) \cdot 10^{-5}\,\text{eV}^2$, $\Delta m_{32}^2 = (2.43 \pm 0.13) \cdot 10^{-3}\,\text{eV}^2$ in the case of the mass differences and with $\sin^2(2\vartheta_{12}) = 0.87 \pm 0.03$ and $\sin^2(2\vartheta_{23}) > 0.92$ in the case of the mixing angles, all parameters of the neutrino mixing matrix except for the small mixing angle ϑ_{13} and the phase δ have been determined to high accuracy [11]. For ϑ_{13} only an upper limit of $\vartheta_{13} < 0.16$ [11] could be set. There are further unknown fundamental properties of the neutrinos such as the absolute mass scale, the hierarchy of the mass eigenvalues of the neutrinos, and whether neutrinos are Majorana particles or not that currently are under investigation or have to be addressed by future experiments.

The reactor neutrino experiment Double Chooz in the French Ardennes provides a promising possibility to finally assign the missing angle ϑ_{13} [9] or at least to improve its limit. In both cases, the result will have a significant impact on the determination of the CP violation phase δ since the potential of future accelerator neutrino experiments regarding its finding particularly depends on the exact value of ϑ_{13} [32]. Using the Chooz nuclear reactor plant as a powerful neutrino source Double Chooz pursues a new concept of making a competitive measurement with two identical detectors. While the so-called near detector is meant for flux monitoring, the far detector will be sensitive on effects from neutrino oscillations due to ϑ_{13}. The detectors are based on liquid scintillators. In order to control the background induced by cosmic muons, both detectors feature an *inner veto* which is a dedicated muon identification system based on liquid scintillator. Additionally, the *buffer* containing a non-scintillating liquid has been installed to shield the target from natural radioactivity. Optical properties, such as the light yield and the attenuation length of all liquids of the detectors, have a significant influence on the physical success of the Double Chooz experiment.

In the course of this thesis, measurements of the light yield of the DC muon veto scintillator as well as of the attenuation length of both the muon veto scintillator and the buffer liquid have been carried out in order to decide on the composition of the liquids.

Concerning the MU scintillator, an attenuation length of more than $5\,\text{m}$ at $430\,\text{nm}$, which is the characteristic wavelength of light emission, is required to guarantee

that light of every event located in the liquid reaches the PMTs at the detector volumes surface. In the case of the buffer liquid, the same applies to the events in the target leading to a desired attenuation length of more than 6 m. In order to make a decision concerning the products used for both muon veto scintillator and buffer liquid, samples of different candidates have been tested on their attenuation length using an UV/Vis-spectrometer. As primary luminescent for the muon veto scintillator different LAB have been under consideration. The best results with an attenuation length of more than 9 m at 430 nm, which is the wavelength of interest, were obtained by the LAB from the company Helm in Spain. In order to adapt the scintillator to the required density of $0.804 \, g/cm^3$, a second component is added. For this purpose, different n-paraffins and tetradecane were tested. While the attenuation length of tetradecane with less than 5 m was found to be too short, all n-paraffins tested showed high attenuation lengths in the range of 12 m and hence would have been eligible candidates. Due to the best offer, the decision was made for the company CBR.

Regarding the buffer liquid it has been foreseen to use a mixture of a mineral oil and in order to achieve the required density also n-paraffin. While in the case of n-paraffin, the decision had already been made in favor of the company CBR, the mineral oils Ondina 909 and Ondina 917 from the company Shell have been under investigation in the case of the mineral oil. With more than about 10 m, Ondina 909 did show higher attenuation lengths than Ondina 917 with about 7 m. Since Ondina 909 was discontinued by Shell, the decision has been made for Ondina 917, whose transparency also was sufficient.

The optimal concentration of the wavelength shifter PPO for the muon veto scintillator has been determined. Therefore, light yield measurements for scintillator liquids with varying PPO-concentration under the irradiation of a ^{137}Cs-source were carried out using an experimental setup for a coincidence measurement. The best PPO concentration was found to be 2 g/l. With a light yield of (8.7 ± 1) photons/keV, the muon veto scintillator with its final products met the requirements concerning Double Chooz.

The finalized compositions of both the muon veto scintillator and the buffer liquid are listed in table (8.1). A Master Solution of the muon veto scintillator containing LAB and the highly concentrated wavelength shifters PPO and bisMSB has been prepared at Wacker Chemie in Munich. In Chooz the Master Solution has been diluted to the muon veto scintillator concentration. Both the scintillator and the buffer liquid have finally been mixed on site and adapted to the correct density.

Samples of the liquids stored in Chooz, ready to be filled in the detector, have again been tested on their light yield as well as on their attenuation lengths. The light yield of the scintillator was determined to be (9 ± 1) photons/keV, which even exceeds the expected (8.7 ± 1) photons/keV.

The attenuation length at the characteristic wavelength of light emission of 430 nm for the muon veto scintillator was found to be more than 8 m and for the buffer

muon veto scintillator	company	buffer liquid	company
48.4 % vol. LAB	Helm Spain		
51.6 % vol. n‑paraffin	CBR	46 % vol. n‑paraffin	CBR
2 g/l PPO	Perkin Elmer	54 % vol. Ondina 917	Shell
20 mg/l bisMSB	Perkin Elmer		

Table 8.1.: *Final composition of the Double Chooz muon veto scintillator and the buffer liquid.*

liquid more than 12 m. Both liquids, hence, are very transparent and exceed the requirements regarding the attenuation.

In addition, the muon veto scintillator from Chooz has been tested on its light yield due to neutron irradiation. The principal reaction of neutrons incident on the scintillator is elastic neutron‑proton scattering. The recoiled protons are responsible for the ionization of the scintillator molecules and hence, the light output. Due to radiationless deexcitation processes grouped together under the term of quenching, not the whole energy that has been deposited in a liquid scintillator medium by incident particles is converted into detectable light. Taking this into account, the quenching factor describes the scintillation efficiency and, therefore, is a relevant parameter for a precise understanding of the Double Chooz detector response. For the determination of the proton‑quenching factor for the muon veto scintillator the MLL accelerator was used as a neutron source. By time‑of‑flight measurements performed during a beamtime of about one week the proton‑quenching factor at 10.6 MeV was assigned to be (2.6 ± 0.4). For a further investigation of its energy dependence a Monte Carlo simulation was used. The quenching factors that have been determined for energies within the range of the experimental data can be seen in table (8.2).

The shape of the emitted light pulses of a scintillator varies for particles of different ionizing power due to the excitation of different fluorescence mechanisms. For certain scintillators, where this effect is strong, this can be used to distinguish between different types of incident particles. In the course of the beamtime at the MLL accelerator, the DC muon veto scintillator has additionally been tested on its capability of distinguishing between incident neutrons and gammas via pulse‑shape discrimination. The neutron‑gamma discrimination was found to be possible on a $1\,\sigma-$ level above an energy threshold of 2180 keV. As regards Double Chooz, the fact that neutron and gamma events can subsequently be identified on a certain level will allow a better control of the background.

Further improvements concerning the measurements of the light yield due to γ‑irradiation could be reached by implementing an experimental setup for the absolute light yield. The measurements performed in this thesis used a relative method.

E_p [MeV]	9	8	7	6	5
$QF(E_p)$	2.7 ± 0.1	3.0 ± 0.1	3.4 ± 0.1	4.0 ± 0.2	4.8 ± 0.2

Table 8.2.: *Based on the energy dependence that was derived from a Monte Carlo simulation, the quenching factor was calculated for different energies within the range of the measured data.*

Results that are independent from a reference sample could be achieved by realizing a complex 4π-detector geometry.

For the attenuation length measurements with the UV/Vis-spectrophotometer the samples under investigation had to be filled in a sample cell of 0.1 m length. Measurements with higher precision, however, could be obtained by new experimental setups using path lengths that are in the range of the expected attenuation lengths (~ 6 m).

The experimental setup for the time-of-flight measurements at the MLL presented in this thesis is a general possibility to perform further quenching factor measurements under irradiation of neutrons and to proceed with investigating the neutron-gamma discrimination capability of liquid scintillators. A repetition of the measurements would indeed be desirable in order to increase statistics and hence, the reliability of the results. Furthermore, measurements using neutrons of different energies, would be interesting and lead to a more detailed understanding of the energy dependence of the proton-quenching factor.

The possibility of pulse-shape discrimination is a crucial issue for next-generation neutrino experiments. For LENA with the subject to a possible observation of rare neutrino events from the diffuse supernova neutrino background (DSNB), for example, controlling the background is highly important [81]. The fact that the Double Chooz muon veto scintillator was found to be generally capable of neutron-gamma discrimination together with its high transparency and light yield speaks in favor for LAB as a scintillator candidate for future neutrino experiments.

Regarding Double Chooz, both the muon veto scintillator and the buffer liquid will allow a successful performance. The results for the quenching factor and the discrimination capability are essential for the Double Chooz analysis and hence will contribute to its success in the search for ϑ_{13}.

A. Attenuation Length Corrections

For the measurement of an empty cell, reflections of four boundary layers are contributing to the attenuation as described in sec. (5.3). Presuming wavelength independent reflections at the layers between air and glass, the absorbance measured with an empty cell can be written as

$$
\begin{aligned}
A_{cell} &= log_{10}\left(\frac{I(0)\cdot(1-R)^4}{I(x)}\right) \\
&= log_{10}\left(\frac{I(0)}{I(x)}\right) + log_{10}\left((1-R)^4\right) \\
&= A_{glass+air} + 4\cdot log_{10}(1-R)
\end{aligned}
\tag{A.1}
$$

where $A_{glass+air}$ is the absorbance of both the quartz glass of the cell and the air. R is the reflectivity of the boundary between quartz glass and air, $I(0)$ the intensity of the incident light ray and $I(x)$ the reflectivity of the light ray having crossed the cell.

The absorbance of the cell filled with the sample, which only has two layers contributing (see sec. (5.3)), on the other hand, is

$$
\begin{aligned}
A_{full} &= log_{10}\left(\frac{I(0)\cdot(1-R)^2}{I(x)}\right) \\
&= log_{10}\left(\frac{I(0)}{I(x)}\right) + log_{10}\left((1-R)^2\right) \\
&= A_{glass+liquid} + 2\cdot log_{10}(1-R)
\end{aligned}
\tag{A.2}
$$

Here $A_{glass+liquid}$ refers to the absorbance of both the glass and liquid. In order to obtain A_{liquid}, half of the absorbance for the empty cell is subtracted from the absorbance of the full cell, according to

$$
A_{liquid} = A_{full} - \frac{1}{2}A_{cell}.
\tag{A.3}
$$

Inserting eq. (A.2) and eq. (A.1) and applying the fact that the absorbance of a

multi component system is the sum of the absorbances of the single components (see sec. (5.1)), $A_{full} - \frac{1}{2}A_{cell}$ actually evaluates to

$$
\begin{aligned}
A_{full} - \frac{1}{2}A_{cell} &= A_{glass} + A_{liquid} + 2 \cdot log_{10}\left(1 - R\right) \\
&\quad - \frac{1}{2}\left(A_{glass} + A_{air} + 4 \cdot log_{10}\left(1 - R\right)\right) \\
&= A_{liquid} + \frac{1}{2}A_{glass} - \frac{1}{2}A_{air}
\end{aligned}
\tag{A.4}
$$

Neglecting the absorbance of air and considering the wavelength dependence, this becomes the absorbance $A'(\lambda)$ of sec. (5.3):

$$
A'(\lambda) = A_{full}(\lambda) - \frac{1}{2}A_{cell}(\lambda) = A_{liquid}(\lambda) + \frac{1}{2}A_{glass}(\lambda).
\tag{A.5}
$$

Now $A'(\lambda)$ still has to be corrected for the remaining absorbance of glass. Therefore, the smallest occurring absorbance A_{min} at the wavelength λ_{min}, which is

$$
A_{min} = A(\lambda_{min}) = \underbrace{A_{liquid}(\lambda_{min})}_{\approx 0} + \frac{1}{2}A_{glass}(\lambda_{min})
\tag{A.6}
$$

is used. Assuming that the transmission at the wavelength position λ_{min} is maximal, $A_{liquid}(\lambda_{min})$ is zero. Furthermore, the wavelength dependence of the quartz glass has to be neglected, which, however, is a good approximation [64].
This leads to the corrected absorbance $A(\lambda)$ of the sample that is taken for the calculation of the attenuation length in sec. (5.3):

$$
\begin{aligned}
A(\lambda) &= A'(\lambda) - A_{min} \\
&= A_{liquid}(\lambda) + \frac{1}{2}A_{glass}(\lambda) - \frac{1}{2}A_{glass}(\lambda_{min}) \\
&= A_{liquid}(\lambda).
\end{aligned}
\tag{A.7}
$$

B. Attenuation Length of the Final Liquids from Chooz

Attenuation length of final liquids

wavelength [nm]	AL MU tank 1	AL MU tank 2	AL MU tank 3	AL BF tank 1	AL BF tank 2	AL BF tank 3
450	10.44	11.11	10.81	13.05	16.02	16.17
448	10.45	10.96	10.82	13.52	16.09	16.17
446	10.58	11.16	10.97	13.86	16.54	16.88
444	10.72	11.39	11.23	14.18	17.64	17.93
442	10.41	10.89	10.84	13.86	16.94	17.06
440	9.94	10.49	10.30	13.27	16.64	17.00
438	9.64	10.14	10.06	13.00	16.30	16.43
436	9.30	9.73	9.70	12.72	16.01	16.23
434	9.06	9.41	9.40	12.91	15.79	16.08
432	8.65	8.96	9.00	12.35	15.62	15.70
430	8.16	8.39	8.46	11.98	15.07	15.30
428	7.73	8.01	8.12	11.92	14.97	15.16
426	7.13	7.49	7.59	11.55	14.94	15.20
424	6.62	6.79	6.96	11.48	14.24	14.60
422	5.86	6.02	6.19	11.45	14.35	14.71
420	5.10	5.20	5.33	11.12	13.93	13.95
418	4.31	4.40	4.51	10.97	13.95	14.07
416	3.51	3.52	3.63	10.95	13.66	13.58
414	2.74	2.75	2.83	10.41	13.14	13.21
412	2.03	2.03	2.08	10.20	12.93	12.97
410	1.41	1.40	1.44	10.17	12.57	12.80
408	0.89	0.89	0.91	9.72	12.52	12.81
406	0.52	0.52	0.53	9.73	12.18	12.34
404	0.28	0.28	0.29	9.49	11.87	12.15
402	0.15	0.15	0.15	8.98	11.66	11.78
400	0.08	0.08	0.09	8.87	11.22	11.51

Table B.1.: *The table lists the attenuation lengths (AL) of the final muon veto scin-tillator (MU) and the buffer liquid (BF) that have been calculated for the wavelength range from 400 nm to 450 nm. A sample of each of the three buffer and the three muon veto tanks of the storage area in Chooz has been measured with the UV/Vis-spectrometer.*

List of Figures

List of Tables

Bibliography

[1] L. Bergström and A. Goobar. *Cosmology and particle astrophysics.* Springer-Verlag, New York, Berlin, Heidelberg, 2nd edition, 2008.

[2] F. Halzen and A. D. Martin. *Quarks and leptons.* John Wiley and sons, 1984.

[3] N. Schmitz. *Neutrinophysik.* Teubner-Verlag, Stuttgart, 1997.

[4] C. L. Cowan et al.. Detection of the Free Neutrino: a Confirmation. *Science*, (124, 103), 1956.

[5] R. Davis et al.. Search for neutrinos from the sun. *Phys. Rev. Lett.*, (20, 1205), 1968.

[6] P. Anselmann et al.. Solar neutrinos observed by GALLEX at Gran Sasso. *Phys. Lett.*, (B 285, 376), 1992.

[7] M. Ishitsuka for the Super-Kamiokande collaboration. Super-Kamiokande results: atmospheric and solar neutrinos. E-print arXiv:physics/0404071v2.

[8] Q. R. Ahmad et al.. Direct evidence for neutrino flavour transformation from neutral-current interactions in the Sudbury Neutrino Observatory, 2001. E-print arXiv:nucl-ex/0204008 and arXiv:nucl-ex/0204009.

[9] Double Chooz Collaboration. A Search for the Neutrino Mixing Angle $\boldsymbol{\theta_{13}}$, 2006. E-print arXiv:hep-ex/0606025v4.

[10] M. Apollonio et al.. Limits on neutrino oscillations from the Chooz experiment. *Phys. Lett. B.*, (466, 415), 1999. E-print arXiv:hep-ex/9907037.

[11] K. Nakamura et al.. The Review of Particle Physics. *J. Phys.*, (G 37, 075021), 2010. http://pdg.lbl.gov.

[12] C. Giunti. Theory of neutrino oscillations, 2004. E-print arXiv:hep-ph/0409230.

[13] S.M. Bilenky and B. Pontecorvo. Lepton mixing and neutrino oscillations. *Phys. Rept.*, (41, 225), 1978.

[14] B. Kayser. Neutrino physics, 2005. E-print arXiv:hep-ph/0506165v1.

[15] S.M. Bilenky, C. Giunti, and W. Grimus. Long-baseline neutrino oscillation experiments and CP violation in the lepton sector. 1997. E-print arXiv:hep-ph/9712537v1.

[16] M. Fukugita and T. Yanagida. *Physics of Neutrinos and Applications to Astrophysics.* Springer Verlag, 2003.

[17] F. Suekane et al.. An overview of the KamLAND 1-kiloton liquid scintillator. E-print arXiv:hep-ex/0406076.

[18] M.H. Ahn et al.. Measurement of neutrino oscillation by the K2K experiment. *Phys. Rev.*, (D74, 072003), 2006. E-print arXiv:hep-ph/0606032v3.

[19] MINOS collaboration. Preliminary results from MINOS on ν_μ disappearance based on an exposure of $2.5 \cdot 10^{20}$ $120 \, \text{GeV}$ protons on the NuMI target. E-print arXiv:hep-ph/07081495v2.

[20] M. Guler et al.., 2000. CERN/SPSC 2000-028.

[21] Y. Oyama. Results from K2K and status of T2K. E-print arXiv:hep-ex/05012041v2.

[22] O. Mena Requejo et al.. Super-NOνA: A long-baseline neutrino experiment with two off-axis detectors. *Phys. Rev.*, (D 72), 2005. E-print arXiv:hep-ph/0504015.

[23] G. Alimonti et al.. The Borexino detector at the Laboratori Nazionali del Gran Sasso. *Nucl. Instr. and Meth. in Phys. Res. A*, (600, 568-593), 2009.

[24] G. L. Fogli, E. Lisi, A. Marrone, A. Palazzo, and A. M. Rotunno. Neutrino oscillations, global analysis and ϑ_{13}, 2009. E-print arXiv:hep-ph/0905.3549v2.

[25] A. Merle and W. Rodejohann. The Elements of the Neutrino Mass Matrix: Allowed Ranges and Implications of Texture Zeros. 2006. E-print arXiv:hep-ph/0603111.

[26] M. Mezzetto. Physics potential of the spl super beam. *J. Phys.*, (G 29, 1781-1784), 2003. E-print arXiv:hep-ex/0302005.

[27] K. Hagiwara et al.. Solving the neutrino parameter degeneracy by measuring the T2K off-axis beam in Korea. *Phys. Lett.*, (B 637, 266-273), 2006. E-print arXiv:hep-ph/0504061.

[28] P. Huber et al.. Reactor neutrino experiments compared to superbeams. *Nucl. Phys.*, (B 665, 487), 2003. E-print arXiv:hep-ph/0303232v2.

[29] L. Oberauer. Search for ϑ_{13} with reactor experiments. *Prog. Part. Nucl. Phys.*, (57,127), 2006.

[30] S.M. Bilenky, D. Nicolo, and S.T. Petcov. Constraints on $|U_{e3}|^2$ from a three-neutrino oscillation analysis of the CHOOZ data. *Phys. Lett.*, (B 538, 77), 2002. E-print arXiv:hep-ph/0112216.

[31] http://irfu.cea.fr/images/aslmg/2656_1.jpg, 2010.

[32] S. Berridge et al.. Proposal for U.S. participation in DOUBLE CHOOZ: A new ϑ_{13} experiment at the Chooz reactor. E-print: arXiv:hep-ex/0410081.

[33] V. Zimmer. Development of a muon track reconstruction with the inner veto of Double Chooz. Diploma thesis, Technische Universität München, 2010.

[34] M. Apollonio et al.. Search for neutrino oscillations on a long baseline at the CHOOZ nuclear power station. *Eur. Phys. J.*, (C 27, 331), 2003. arXiv:hep-ex/0301017.

[35] J. B. Birks. *Scintillation Counters*. Pergamon Press, London, 1953.

[36] W. R. Leo. *Techniques for Nuclear and Particle Physics Experiments*. Springer Verlag, Berlin, 1987.

[37] T. Marrodán Undagoitia. *Measurement of light emission in organic liquid scintillators and studies towards the search for proton decay in the future large-scale detector LENA*. PhD thesis, Technische Universität München, 2008.

[38] T. Förster. *Fluoreszenz organischer Verbindungen*. Vandenboeck und Ruprecht in Göttingen, 1950.

[39] C. E. Mortimer and U. Müller. *Das Basiswissen der Chemie*. Georg Thieme-Verlag, 8th edition, 2003.

[40] J. R. Lakowicz. *Principles of fluorescence spectroscopy*. Springer Verlag, 2nd edition.

[41] A. Jablonski. *Z. Phys.*, (94, 38), 1935.

[42] G. F. Knoll. *Radiation Detection and Measurement*. Wiley, 1989.

[43] C. Grupen. *Teilchendetektoren*. BI Wissenschaftsverlag, 1993.

[44] H. Morrison and G. Pandey. Singlet excited-state "energy hopping" in alkyl-benzenes. *Chem. Phys. Lett.*, (1, 96).

[45] T. Forster. *Discuss. Farady Soc.*, (27, 7), 1959.

[46] C. Buck, F. X. Hartmann, D. Motta, and S. Schoenert. Energy transfer and light yield properties of a new highly loaded indium(III) β-diketonate organic scintillator system. *Chem. Phys. Lett.*, (435, 252-256), 2007.

[47] Th. Jagemann, F.v. Feilitzsch, and J. Jochum. Measurement of the scintillation light quenching at room temperature of sodium recoils in NaI(Tl) and hydrogen recoils in NE 213 by the scattering of neutrons. *Nucl. Inst. and Meth. in Phys. Res.*, (A 564, 549-558), 2006.

[48] http://www.helmag.com/de, 2010.

[49] http://www.cepsa.com/, 2010.

[50] EG Sicherheitsdatenblatt - Linear-Alkylbenzol, 2009.

[51] Material safety data sheet - Linear Alkylbenzene Petrelab 550-Q (P 550-Q), 2007.

[52] http://www.hansachemie.eu/de, 2010.

[53] A. Röckl. Test and Installation of Level Measurement Systems for the Double Chooz Experiment. Diploma thesis, Technische Universität München, 2010.

[54] Produktdatenblatt - Cobersol C 70, 2008.

[55] Sheet of Typicalproperties - Petrepar n-C_{14}, 2008.

[56] http://www.cbr-online.de, 2010.

[57] 2010. http://www.perkinelmer.com/.

[58] Material safety data sheet - PPO, 2004. http://www.perkinelmer.com/.

[59] M. Wurm. Untersuchungen zu den optischen Eigenschaften eines auf PXE basierenden Flüssigszintillators und zum Nachweis von "Supernova Relic Neutrinos" mit dem zukünftigen Neutrinodetektor LENA. Diploma thesis, Technische Universität München, 2005.

[60] Material safety data sheet - bisMSB, 2004. http://www.perkinelmer.com/.

[61] Material safety data sheet - Shell Ondina oil 909, 2010. http://www.epc.shell.com/.

[62] Material safety data sheet - Shell Ondina oil 917, 2010. http://www.epc.shell.com/.

[63] H.-L. Xiao and J.-S. Deng. Oxygen quenching in LAB based liquid scintillator and nitrogen bubbling model. *Chinese Physics*, (C, 34, 5), 2009. E-print arXiv:nucl-ex/0904.1329v4.

[64] W. Demtröder. *Experimentalphysik 2, Elektrizität und Optik.* Springer Verlag, 5th edition.

[65] M. Hesse, H. Meier, and B. Zeeh. *Spektroskopische Methoden in der organischen Chemie.* Georg Thieme-Verlag, 7th edition, 2005.

[66] J. M. Hollas. *Moderne Methoden in der Spektroskopie.* Vieweg-Verlag, 1995.

[67] E. W. Otten. *Repetitorium Experimentalphysik für Vordiplom und Zwischenprüfung.* Springer Verlag, Berlin, 2002.

[68] M. Wurm et. al.. Optical Scattering Lengths in Large Liquid-Scintillator Neutrino Detectors. *Rev. of Scient. Instr.*, (81, 5, 053301), 2010.

[69] C. Aberle. Optimierung der Fluoreszenzcharakteristik von Flüssigszintillatoren des Double Chooz Reaktorneutrinoexperiments. Diploma thesis, Max-Planck-Institut für Kernphysik Heidelberg, 2008.

[70] P. Huang et al.. Study of attenuation length of linear alkyl benzene as LS solvent, 2010. E-print: http://iopscience.iop.org/1748-0221/5/08/P08007.

[71] P. Pfahler. Bestimmung der absoluten Lichtausbeute des Flüssigszintillators für die äusseren Detektorkomponenten des Neutrinoexperiments Double Chooz. Diploma thesis, Technische Universität München, 2007.

[72] Electron Tubes Ltd. 25 mm (1") photomultiplier 9111B series data sheet, 2009. http://www.electrontubes.com/pdf/9111B.pdf.

[73] G. Alimonti et al.. Light propagation in a large volume liquid scintillator. *Nucl. Instr. and Meth. in Phys. Res. A*, (440, 360), 2000.

[74] R. Strauss. Quenching Factor Measurements of CaWO4 at mK Temperatures by Neutron Scattering for the Dark Matter Experiments CRESST and EURECA. Diploma thesis, Technische Universität München, 2009.

[75] C. Ciemniak. PhD thesis, Technische Universität München. in preparation.

[76] http://www.item24.com, 2010.

[77] Firestone (Editor). *Table of Isotopes.* John Wiley & Sons, 8th edition, 1996.

[78] M. J. Berger, J.S Coursey, M. A. Zucker, and J. Chang. Computer programs for calculating stopping-power and range tables for electrons, protons, and helium ions. Online available: http://physics.nist.gov/Star [2010, October]. National Institute of Standards and Technology, Gaithersburg, MD.

[79] B. Di Cesare. Calculation of the Birks quenching factor for Borexino's scintillator. talk, 2008.

[80] J. F. Beacom, W. M. Farr, and P. Vogl. Detection of Supernova Neutrinos by Neutrino - Proton Elastic Scattering, 2002. E-print arXiv:hep-ph/0205220v1.

[81] Möllenberg, R. Monte Carlo Study of the Fast Neutron Background in LENA. Diploma thesis, Technische Universität München.

[82] P. Huber, M. Lindner, M. Rolinec, T. Schwetz, and W. Winter. Combined potential of future long-baseline and reactor experiments. 2004. E-print arXiv:hep-ph/0412133.

[83] E. Condon. *Phys. Rev.*, (28, 1182), 1926.

[84] J. Franck and E. G. Dymond. *Trans. Faraday Soc.*, (21, 536), 1926.

[85] T. Jagemann. *Measurement of the Scintillation Light Quenching for Nuclear Recoils induced by Neutron Scattering in Detectors for Dark Matter Particles.* PhD thesis, Technische Universität München, 2004.

[86] H. V. Klapdor-Kleingrothaus and K. Zuber. *Teilchenastrophysik.* Teubner-Verlag, Stuttgart, 1997.

[87] M. Hofmann. Low-background gamma spectroscopy for the neutrino oscillation experiment DOUBLE CHOOZ. Diploma thesis, Technische Universität München, 2007.

[88] L. Kirkup and B. Frenkel. *An Introduction to Uncertainty in Measurement.* Camebridge University Press, 2006.

Danksagung